THERMAL AND CATALYTIC CRACKING OF JP-10 FOR PULSE DETONATION ENGINE APPLICATIONS

M. Cooper and J.E. Shepherd

Graduate Aeronautical Laboratories,
California Institute of Technology, Pasadena, CA 91125

GALCIT Report FM 2002.002

This work was carried out under P.O. No. 00-592 for
Advanced Projects Research, Inc. under AF contract F04611-99-C-0017.

December 16, 2002

Abstract

Practical air-breathing pulse detonation engines (PDE) will be based on storable liquid hydrocarbon fuels such as JP-10 or Jet A. However, such fuels are not optimal for PDE operation due to the high energy input required for direct initiation of a detonation and the long deflagration-to-detonation transition times associated with low-energy initiators. These effects increase cycle time and reduce time-averaged thrust, resulting in a significant loss of performance. In an effort to utilize such conventional liquid fuels and still maintain the performance of the lighter and more sensitive hydrocarbon fuels, various fuel modification schemes such as thermal and catalytic cracking have been investigated.

We have examined the decomposition of JP-10 through thermal and catalytic cracking mechanisms at elevated temperatures using a bench-top reactor system. The system has the capability to vaporize liquid fuel at precise flowrates while maintaining the flow path at elevated temperatures and pressures for extended periods of time. The catalytic cracking tests were completed utilizing common industrial zeolite catalysts installed in the reactor. A gas chromatograph with a capillary column and flame ionization detector, connected to the reactor output, is used to speciate the reaction products. The conversion rate and product compositions were determined as functions of the fuel metering rate, reactor temperature, system backpressure, and zeolite type.

An additional study was carried out to evaluate the feasibility of using pre-mixed rich combustion to partially oxidize JP-10. A mixture of partially oxidized products was initially obtained by rich combustion in JP-10 and air mixtures for equivalence ratios between 1 and 5. Following the first burn, air was added to the products, creating an equivalent stoichiometric mixture. A second burn was then carried out. Pressure histories and schlieren video images were recorded for both burns. The results were analyzed by comparing the peak and final pressures to idealized thermodynamic predictions.

Contents

List of Figures

List of Tables

Nomenclature

A	component amount from integrated detector signal
C	constant of integration for vapor pressure curve
C_M	component concentration in the mobile phase
C_S	component concentration in the solid phase
D	inner diameter of accumulator
E	product expansion ratio
H_{fg}	heat of vaporization
H_{piston}	measured height of accumulator piston
K	distribution coefficient
K_s	flame stretch factor
L	length of capillary column
L_M	Markstein number
M_f	mass of liquid fuel injected into system
M_p	mass of products in system
n_f	moles of liquid fuel injected into system
n_P	moles of products in system
P	pressure
P_1	initial pressure before first burn
P_2	initial pressure before second burn
$(P_{max})_1$	maximum pressure of first burn
$(P_{max})_2$	maximum pressure of second burn
$(P_p)_1$	final pressure of cooled products after first burn
P_{sat}	saturation pressure
Q	heat release of mixture
R	universal gas constant
R_c	column resolution
R_f	instantaneous radius of spherical flame
S	detector signal
S_u	laminar burning velocity
$S_u{}^\circ$	unstretched laminar burning velocity
t	time
T	temperature
t_R	component retention time
T_{sat}	saturation temperature
u	linear velocity of mobile phase
u_u	fluid velocity
U	rate of travel for a component molecule through the capillary column
V	volume of combustion vessel
V_f	measured flame velocity

V_M	volume of mobile phase in the capillary column
V_S	volume of stationary phase in the capillary column
V_{sys}^0	volume of system plumbing upstream of accumulator valves
V_{total}	total volume of system plumbing and instantaneous accumulator volume
W_f	molecular weight of liquid fuel
ΔV_f	volume of liquid fuel injected into system
ϵ	effectiveness factor
ϕ	equivalence ratio
ρ_f	density of liquid fuel
σ	detector signal peak width at half height divided by 2.357
τ_M	fraction of time a molecule spends in the mobile phase

1 Introduction

Pulse detonation engine (PDE) research has primarily been conducted with hydrocarbon fuels such as acetylene, ethylene, and propane due to their ease of use in laboratory experiments. These light gaseous fuels have lower boiling points and reduced critical energies of initiation than storable liquid hydrocarbon fuels (i.e., JP-10 and Jet A) eliminating the need for high energy ignition systems and heated test facilities. However, storable liquid hydrocarbon fuels are probably a necessity in propulsive applications. Gaseous fuels require special storage and dispensing facilities which reduce the available payload capacity. Gaseous fuels can not meet the engine cooling requirements for operation at supersonic flight speeds. Additionally, gaseous fuels pose severe explosion hazards in comparison with liquids. For all of these reasons, particularly the high energy density and cooling capabilities, liquid hydrocabon fuels are essential for practical propulsion systems. However, special techniques of initiation or fuel modification will be needed to use these fuels in PDE's.

Previous experimental work [1, 2, 3] has been completed studying the detonation properties of fuel additives such as methane, acetylene, ethers, and nitrates for sensitizing the main fuel component. Other means of reducing the critical ignition energy for PDE applications have included a separate driver section upstream of the main detonation tube. Under the correct conditions, a separate driver has enabled less sensitive mixtures to detonate; however, this method does not eliminate the need for a sensitive gaseous fuel and oxidizer. This reduces the additional payload capacity gained by using the storable liquid hydrocarbon fuels with higher energy densities. If JP-10 is to be used directly in hypersonic flight, temperatures are expected to be near or above the auto-ignition temperature of the fuel. Zhang et al. completed detonation studies of JP-10 vapor detonation near the auto-ignition temperature observing a significant increase in cell size and an increase in the initiation energy [4]. An alternative to pre-initiator systems is modification of the fuel composition by catalytic cracking. This will produce a mixture of molecules that are smaller than the parent molecule and hopefully, easier to detonate.

This research conducts experiments to thermally and catalytically crack JP-10 to quantify product species and concentrations. A chemical approach with respect to the reaction mechanisms and pathways is not studied here. Instead, these results determine the feasibility of cracking reactions with JP-10 as a means of fuel sensitization for low energy detonation initiation in PDEs.

2 Hydrocarbon cracking

Hydrocarbon cracking (HC) is the process by which higher molecular weight hydrocarbons are converted into lower molecular weight hydrocarbons through C-C bond fission [5]. There are three types of HC, including thermal cracking or pyrolysis, catalytic cracking, and hydrocracking, which occur via different chemical pathways and reaction conditions. Pyrolysis typically occurs at temperatures greater than 1000 K [6]. Catalytic cracking occurs with a catalyst that comes into contact with the sample in a reactor.

There are many reactor types, including tubular, plug flow, mixed bed, and fluidized bed. Reactor operating conditions can vary significantly depending on the catalyst and sample used. Most catalytic cracking reactions typically occur at temperatures between 200 - 600°C and pressures close to 1 atm. Hydrocracking occurs under high pressures, typically between 80 and 200 atm, in the presence of added hydrogen. Large pore zeolites with noble metals are used at operating temperatures between 270 and 450°C [5].

JP-10, also called exo-tetrahydrodicyclopentadiene, is a single-component hydrocarbon (Fig. 2) produced synthetically by the hydrogenation of dicyclopentadiene [7]. It is a popular missile fuel because of its increased energy storage through strained cyclic geometries [8] and is considered ideal for volume limited applications [7]. Little is known of JP-10's high temperature chemistry since few experiments identifying the cracking mechanisms have been completed. However, experiments on detonation pressure, detonation wave speed, and cell width have been completed in JP-10 mixtures and mixtures representative of decomposed JP-10 [1]. Both the high initiation energy and large cell size characteristic of JP-10 mixtures indicated low mixture sensitivity to detonation initiation. JP-10 does have a similar cell size to propane (Fig. 1) with similar difficulties in initiation. Schauer et al. [9] have achieved detonations in propane-air mixtures, but only

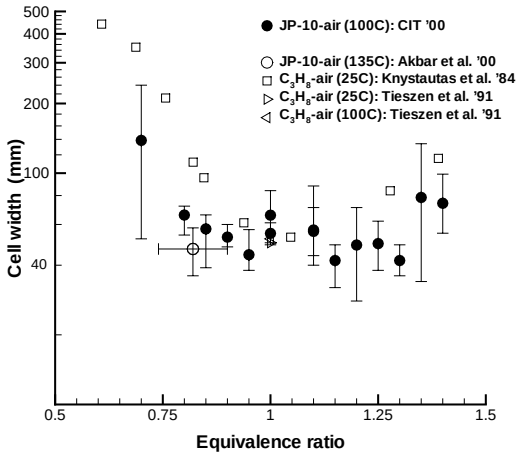

Figure 1: Cell widths of JP-10 and propane mixtures as a function of equivalence ratio.

for a small range of equivalence ratios. For these reasons, we study hydrocarbon cracking as a method of increasing the mixture sensitivity and reducing the critical initiation energy of JP-10 mixtures. Experimental capabilities of our system enable an investigation of HC by the thermal and catalytic cracking mechanisms. Hydrocracking was not studied due to high reaction pressures and the need for excess hydrogen.

2.1 Thermal cracking

Thermal cracking of JP-10 can be split into two studies depending on the level of dissolved oxygen in the fuel: oxidative and non-oxidative pyrolytic decomposition [7]. Experi-

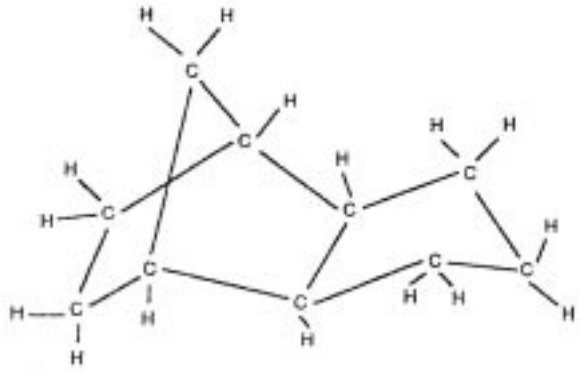

Figure 2: Structure of JP-10 ($C_{10}H_{16}$) molecule.

ments [6] studying non-oxidative pyrolysis of JP-10 were completed in a flowing reactor with residence times of approximately 2 ms and temperatures up to 1500 K. The experimental facility consisted of a heated quartz tube eliminating the possibility of surface reactions. Product analysis with a GC-MS observed benzene at temperatures greater than 1250 K and cyclopentadiene below 1250 K [6]. Davidson et al. [8] investigated JP-10 oxidative pyrolysis behind a reflected shock at conditions between 1.2 to 1.5 bar and 1100 to 1700 K. The UV absorption cross-sections of the decomposition products did not show any benzene. This is possibly due to the short test time ($\sim$50 μs) since benzene is expected to form through secondary chemical reactions at later times [8]. The results of these two studies are largely inconclusive due to varying test conditions and little knowledge of the radical reaction pathways.

Abbot and Wojciechowski illustrate the necessity of correcting catalytic cracking results for thermal cracking as the chemical pathways may be affected [10]. Thus, we quantify JP-10 thermal cracking in our reactor for comparison with the catalytic cracking results.

2.2 Catalytic cracking with zeolites

The popularity of catalytic cracking increased during the 1960's with the need to produce high octane gasoline and hydrocarbons from methanol using synthetic zeolite catalysts. Those commercial processes that produce gasoline and high grade military fuels from crude oils typically use fluidized bed reactors containing a mixture of zeolite catalyst and crude oil [5, 11]. The mixture passes through a heated reaction zone followed by a series of processes to recover the cracked products and zeolite. Because of significant coke and deposit formation, the zeolite is regenerated under high temperatures between 590 and 730°C in an air purge before being mixed again with the crude oil feedstock at the beginning of the process. Zeolite catalysts used in the harsh operating conditions of heavy oil cracking are typically of the faujausite (FAU) structure [11].

Different zeolite types refer to a porous, crystalline alumniosilicate of a specific molecular structure. The HY zeolite is of the FAU structure. More generally, zeolites are

comprised of tetrahedral frameworks of AlO_4 and SiO_4 connected through shared oxygen atoms creating a secondary building unit. A zeolite unit cell is comprised of an integral number and a single type of these secondary building units [12]. The arrangement of the secondary building units into rings results in the formation of channels, pores, and cages with dimensions and orientations specific to a given zeolite type. These parameters thus define a zeolite's reactivity and shape-selectivity. Because of the shared oxygen atoms, the framework possesses a net negative charge which is balanced by the addition of protons. After proton addition, the zeolite becomes a strong Bronsted acid containing sites for hydrocarbon adsorption [13].

The channel dimensions are well-defined for such tetrahedrally-coordinated zeolites enabling shape-selectivity of the cracking products. Molecules with dimensions larger than the zeolite pore dimensions typically can not enter the channels and obtain access to the internal active sites, but there are exceptions to this statement. Pore diameters of several common zeolite structures appear in Table 1. It is important to note that these dimensions can vary slightly depending on the zeolite's hydration state and temperature [12]. FAU (Fig. 3) zeolites are commonly referred to as "large pore" zeolites

Zeolite	Pore Diameter (Å)
Faujasite (FAU)	7.4
Beta (BEA)	7.6 to 5.5
ZSM-5 (MFI)	5.1-5.6

Table 1: Pore diameters of common zeolites.

because they have supercages approximately 13 Å in diameter which can accommodate large components [14]. ZSM-5 (Fig. 4) is referred to as an "intermediate pore" zeolite

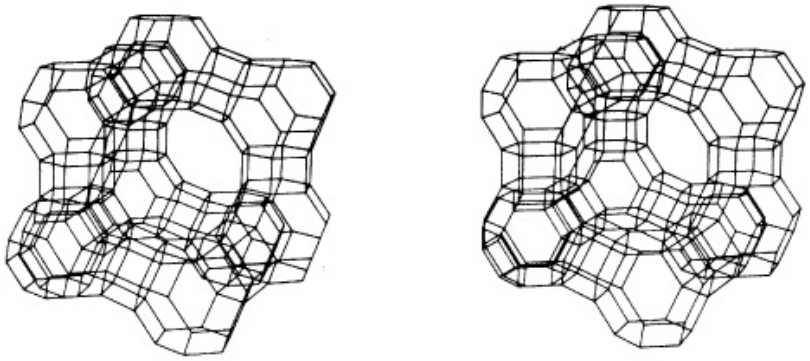

Figure 3: Faujausite zeolite framework viewed along [111].

where the product distribution is restricted to compounds smaller than those of FAU, typically less than C_{11} [14]. Beta is an additional zeolite structure; however, there are few documented experiments using Beta to catalytically crack hydrocarbons.

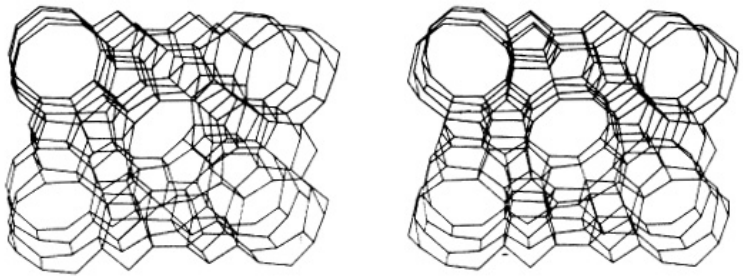

Figure 4: ZSM-5 zeolite framework viewed along [010].

The FAU and ZSM-5 zeolites have been found to deactivate quickly in reactions with hydrocarbons as a result of coke deposition [13, 14]. In an effort to create a zeolite that is more coke resistant, an ultra-stable form of zeolite Y (USY) was created. USY is known to produce more olefins due to decreased hydrogen transfer reactions, produce more aromatics due to a reduction in coke formation, and have a higher thermal stability than HY [5]. Additional attempts to reduce the coking tendency through structural improvements to the FAU structure have met with little success [15, 16].

A variety of studies have been completed with these zeolites. For example, normal alkanes [13, 17, 18, 16, 10] and heavy oils [15] have been studied extensively to characterize zeolite cracking properties in catalytic reforming reactions. Few studies [19, 20, 21] have investigated the cracking of JP-10 with zeolites. Additional studies [19, 20, 22, 23] have investigated the HC of other liquid hydrocarbon fuels both thermally and catalytically. In particular, some studies determined the fuel endothermicity for supersonic engine cooling applications [22, 19, 20] and some studies investigated the factors that affect deposit formation on the zeolites [21, 24].

3 Experimental setup

Design of the experimental facility began in the summer of 2000 and preliminary operation began in the fall of 2001. Testing and modifications occurred from fall 2001 to fall 2002. A timeline of activities is provided in Appendix A.

The facility (Fig. 5) consists of the "reactor panel" upon which individual components are mounted. The panel is 45-inches square and is composed of a 1/8-inch thick sheet of aluminum bolted to a 3/4-inch thick sheet of plywood. Screws around the perimeter hold the two pieces together forming the panel. Unistrut supports vertically stabilize the panel and attach it to a lab workbench. The supports clamp to the table edge eliminating the need for permanent holes to be drilled through the table top. As a result, the panel may be easily relocated to another work area.

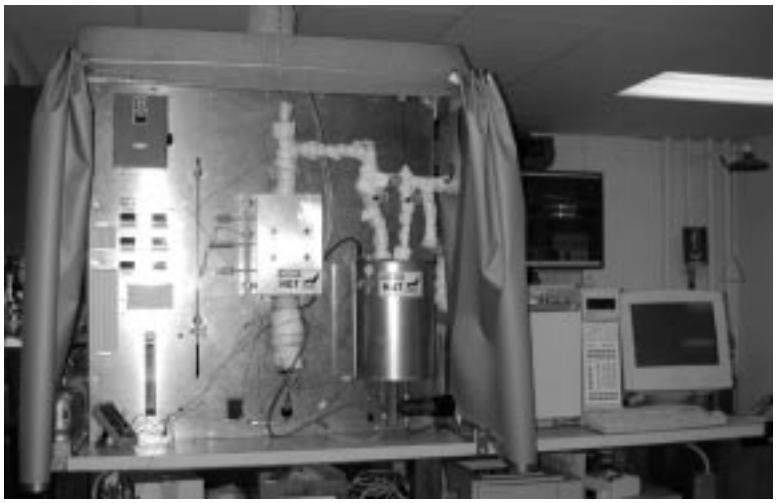

Figure 5: Photograph of reactor panel with gas chromatograph.

The original schematic showing the component order appears in Fig. 6. This schematic was redrawn as shown in Fig. 7 accounting for component dimensions in addition to considering mounting holes for component installation, panel feedthroughs, and electrical wiring. The panel components are discussed in the following sections.

3.1 Rotameters

Two rotameters with 150 mm flowtubes (Omega, Cat. No. FL-3845G) appear near the bottom left corner of the panel (Fig. 6 and 7). Each is capable of metering between 25.3 to 253 cc/min of air. The rotameter outlets were originally plumbed together with 1/4-inch stainless steel tubing and attached to the panel plumbing through the gas inlet valve (GIV). The rotameter inlets were attached directly to nitrogen and methane gas bottles. It was originally thought that these gases were required for zeolite activation but these were not needed so the rotameters have been removed from the panel.

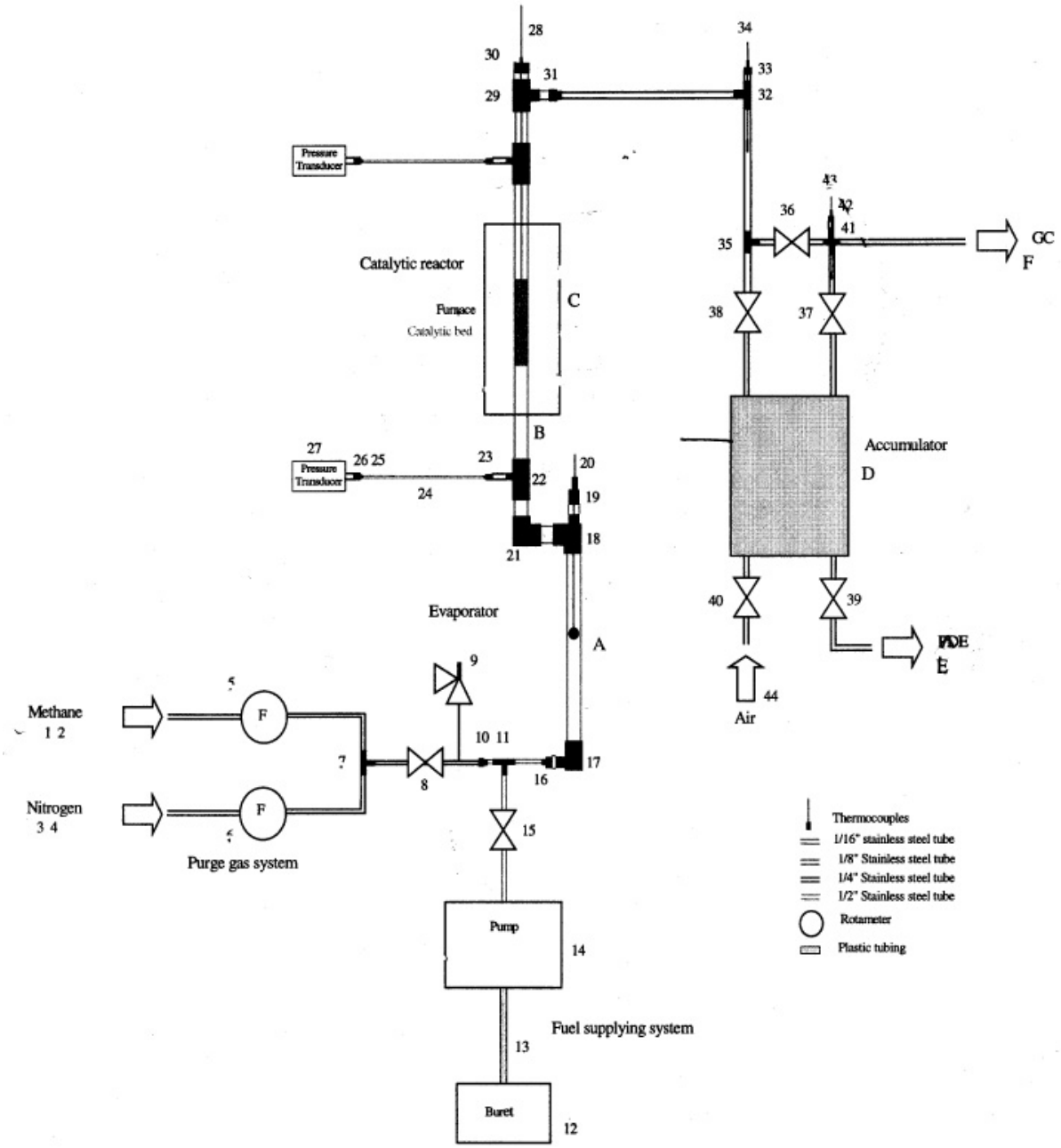

Figure 6: Original conceptual schematic of reactor panel. Refer to Fig. 7 for schematic drawn to scale and Fig. 9 for schematic of redesigned system.

3.2 Fuel pump

A fuel pump is located to the right of the rotameters behind the panel (Fig. 7). It sits on a small plywood platform attached to the backside of the panel and requires 120 VAC for operation. Manufactured by Eldex Laboratories, Inc. (Model A-30-VS, Cat. No. P-

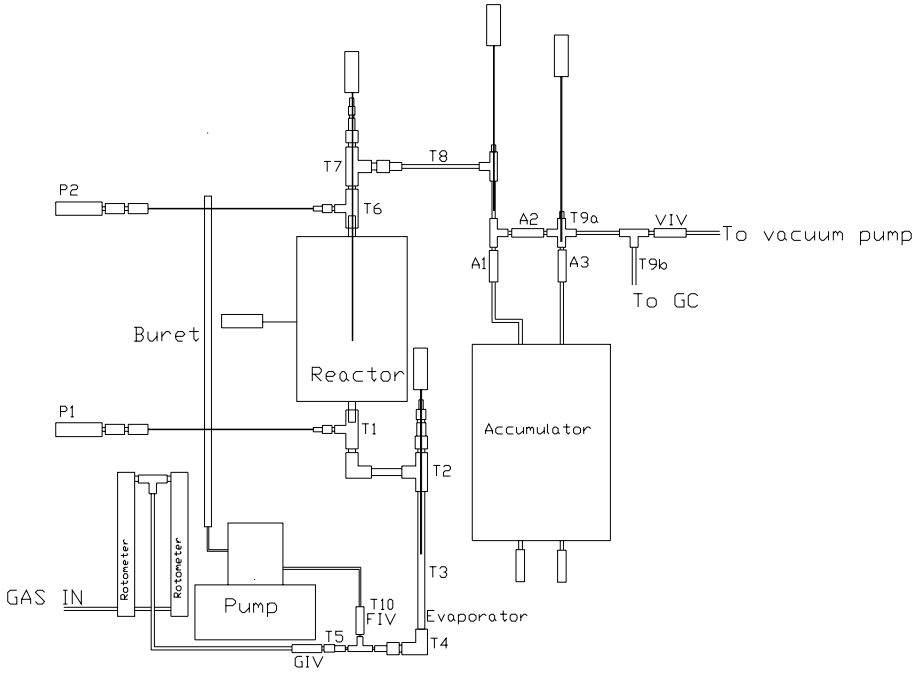

Figure 7: Schematic of reactor panel drawn to scale.

74450-00), the pump uses a sapphire piston to accurately meter liquids between 0.025 and 1.5 ml/min. The liquid flowrate is controlled either manually by a dial, with settings (FP) between 000 and 999, or remotely via electrical connections. Manual operation was used entirely throughout this study. Liquid fuel is supplied to the pump from a 25 ml glass buret (VWR, Cat. No. 17456-121) attached to the front of the panel. Flexible tubing provides the connection between the pump and the glass buret. The pump outlet is attached to the fuel inlet valve (FIV) on the front of the panel with 1/16-inch stainless steel tubing. The FIV connects to the system between the GIV and the evaporator inlet.

If a liquid reservoir is applied to the pump inlet and no backpressure is supplied to the pump outlet, the liquid will flow freely through the pump even when not powered on. During testing, backpressure was supplied to the pump by pressurizing the system with nitrogen. It was determined that a pressure drop across the pump of at least 5 kPa was required to prevent unrestricted flow through the pump. Because the system must be pressurized with nitrogen, the product distributions are diluted.

Calibration of the pump was conducted by recording the change in the buret liquid level over time when attached to the system with an applied backpressure (Fig. 8).

3.3 Evaporator

The evaporator appears on the panel to the right of the FIV and vaporizes the liquid fuel metered in by the fuel pump before it enters the reactor. In the original design (Fig. 6 and 7), the evaporator consisted of single 1/2-inch diameter stainless steel tube with a length

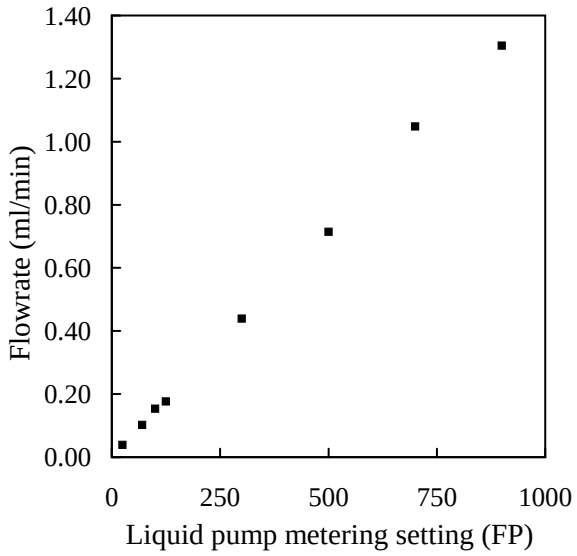

Figure 8: Liquid fuel metering pump calibration curve.

of 12 inches. A series of Swagelok reductions connected the bottom of the evaporator to the FIV and GIV. The top of the evaporator contained several additional Swagelok reductions enabling the installation of a 12-inch long K-type thermocouple with a 1/16-inch sheath (Omega, Cat. No. KQSS-116G-12) to monitor its internal temperature. Just below the thermocouple installation point is a horizontal segment of 1/2-inch stainless steel tubing that attaches the top of the evaporator to the bottom of the reactor. The entire assembly from the FIV to the reactor was wrapped with 6-foot long rope heaters (Omega, Cat. No. FGR-060) capable of operation up to 250°C. However, because of the non-uniformity in the tubing and Swagelok dimensions, obtaining uniform heating using the rope heaters was difficult.

Vapor pressure tests were completed with this system. Because of cold spots and the low operating temperature of the rope heaters, not enough JP-10 could be vaporized to achieve the desired system operating pressure of 200 psi. This led to an evaporator redesign (Fig. 9). The FIV was one cold spot since its maximum operating temperature was 65°C. To eliminate this and other cold spots, the entire plumbing section including the evaporator was removed, from the GIV to the bottom of the reactor. It was replaced by a 200-ml cylindrical vessel with Swagelok fittings welded to the top and bottom end flanges. The bottom flange of the new evaporator contained two 1/16-inch Swagelok connections to the GIV and FIV. The top flange contained a 1/2-inch Swagelok connection attached directly to the bottom of the reactor. Two band heaters (Omega, Cat. No. MBH-2015375B/240) having widths of 2 inches and diameters of 4 inches were installed around the evaporator's outer surface ensuring fast vaporization of the incoming liquid fuel. The band heaters can operate up to 350°C.

The new evaporator was sized for the amount of fuel required to reach a system pressure of 200 psi when vaporized. However, since installation it has been used entirely

with the fuel pump under constant flowrate conditions.

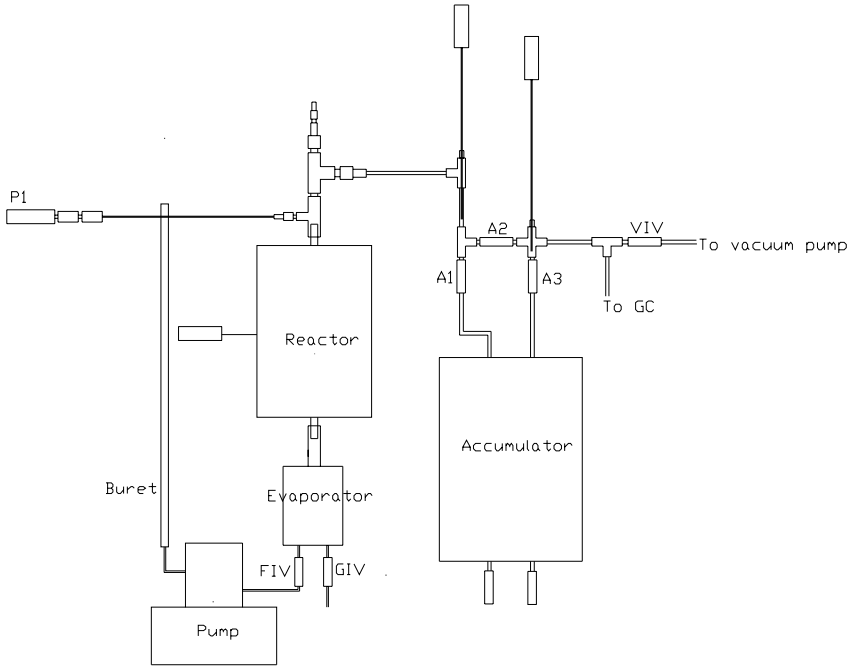

Figure 9: Schematic of reactor panel with redesigned evaporator. Components drawn to scale.

3.4 Reactor

The reactor refers to the main component located in the center of the panel. The reactor contains a 1/2-inch diameter stainless steel tube encased by two copper blocks. A total of eight cartridge heaters (Omega, Cat. No. 3618K263) and three K-type thermocouples are embedded in the copper blocks. This assembly is then enclosed in an aluminum box packed with insulation (Fig. 10). The vaporized JP-10 sample flows through the central tube within which zeolite pellets may be installed.

The cartridge heaters can be connected such that operation at either 262 or 1028 W was possible. A switch enables the user to choose the desired operating power. Re-wiring inside the aluminum casing was required since the insulation on the ground wire, the insulation on the connections between the cartridge heater wires, and the power plug were not rated for high temperature operation. Upon re-wiring, the reactor has operated for up to 36 continuous hours at 500°C with the aluminum casing obtaining temperatures of approximately 100°C and significant surface oxidation occurring on the copper blocks.

The central tube of the reactor allows for the installation and interchanging of catalysts. The design to contain the catalyst consists of three tubes that fit within the central reactor tube. Spacers between the tubes hold porous metal disks which confine the zeolite pellets inside the second spacer tube (Fig. 11). Stainless steel porous disks

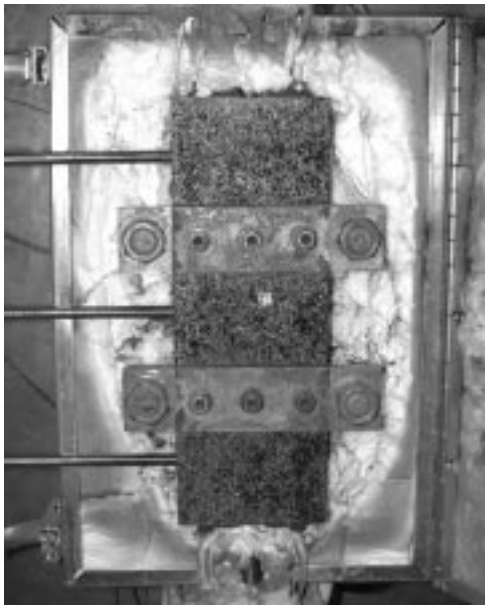

Figure 10: Photograph of inside of the reactor.

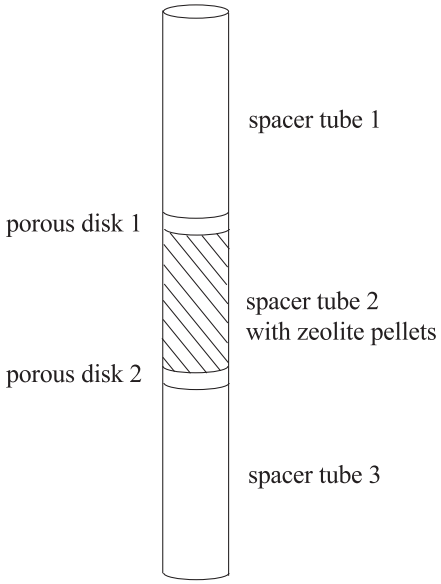

Figure 11: Schematic of tubes and spacers that contain zeolite pellets.

with 100 micron porosity were obtained from Mott Metallurgical Corporation and initially used between the spacer tubes. After several runs, they became coated with coke and were replaced with plugs of glass wool.

The outlet of the reactor contains several Swagelok reductions to an additional 1/16-inch sheathed K-type thermocouple installation point (Omega, Cat. No. KQSS-116G-16). This thermocouple was intended to be embedded directly into the catalyst bed to monitor

reaction temperatures. However, because holes would have to be drilled into the porous metal plates and the presence of the thermocouple made installation and removal of the central reactor tube difficult, it was removed. Since only a gram of zeolite pellets are used and they are not tightly packed within the second spacer tube, a significant temperature gradiant across the bed is not expected and the reactor wall temperature is monitored instead.

Two pressure gauges (Omega, Cat. No. PX302) were initially installed at the inlet and outlet of the reactor (Fig. 7). Upon system redesign, the upstream gauge was removed because a negligibly small pressure drop was found to occur across the zeolite bed.

3.5 Accumulator

The accumulator consists of a vessel that can change its volume through an internal piston and is mounted on the right side of the panel. The piston is contained in a cylinder that is sealed at each end with flanges which contain two 1/4-inch Swagelok connections. The outside of the cylinder is wrapped with a flexible heater and insulation. The end flanges are not heated. The entire assembly including insulation is encased in an aluminum can with removable ends. Based on the design drawings, the accumulator's maximum internal volume, including the volume between the upstream needle valves (A1 and A3) and the accumulator inlet, was calculated to be 1875 cc. Orientation of the upstream needle valves allow the accumulator to be operated in a filling or emptying mode. In the filling mode, all flow from the reactor is directed into the accumulator. In the emptying mode, all flow is directed out of the accumulator to the gas chromatograph (GC).

The bottom flange of the accumulator contains two valves, one of which is directly attached to a gas bottle filled with air via a venting regulator. The venting regulator maintains a constant pressure on the bottom of the piston in the accumulator.

Upon receiving the accumulator at Caltech, several system and accumulator leak tests were performed with the anticipation of system operating pressures up to 200 psi. A large leak rate across the piston was measured. After dismantling the accumulator, several scratches were found on the inner surface of the cylinder. The cylinder was then removed and honed resulting in a decrease in the leak rate from 262.3 sccm to 3.38 sccm. Replacing a leaking plug on the top flange resulted in a final leak rate of 2.47 sccm. The piston is sealed against the internal surface of the cylinder by a Parker FlexiSeal capable of temperatures up to 315°C. The residual leak is probably a result of the honing operation and the resulting insufficient compression of the seal between the piston and internal cylinder surfaces.

The original Omega flexible heater (Omega, Cat. No. SRGL-910/2) capable of temperatures up to 215°C was attached to the outer surface of the cylinder with a self-leveling RTV (GE Red RTV 116). This adhesive is capable of operation up to 204°C after which it begins to thermally decompose producing formaldehyde. Due to the cylinder thickness and the unheated end flanges, the accumulator must be regulated to 215°C to achieve a nominal internal temperature of 200°C. As a result, adhesive decomposition occurred. The accumulator was dismantled again to remove the flexible heater and RTV adhesive.

This heater was replaced with two 400 W flexible heaters (Watlow, Cat. No. 040200C1) capable of operation up to 260°C and were clamped to the cylinder with a thin sheet of aluminum, eliminating the need for any adhesive. The heater wire was replaced with high temperature hookup wire capable of temperatures up to 250°C (Omega, Cat. No. HTTG-1CU-314S). Since the end flanges are not directly heated, the steady state temperature distribution along the accumulator surface over time was measured. It was found that the end flanges were within 17°C of the side wall temperature (Table 2).

Thermocouple position:	Temperature (°C)
Top flange at r = 0	209
Top flange at r = R	211
Bottom flange at r = 0	205
Bottom flange at r = R	198
Side wall at half height	215

Table 2: Temperature distribution measured on accumulator surface after 280 minutes of heating time.

The system plumbing connecting the reactor to the accumulator was 1/4-inch stainless steel tubing wrapped with rope heaters (Omega Cat. No. FGR-060) capable of operation up to 250°C. A vacuum pump was attached to the system outlet in parallel with the GC (Fig. 9). A cold trap was installed to condense and recover the product gases.

3.6 Valves

Both needle valves and ball valves are used in the system. The ball valves originally used were Whitey, Cat. No. SS-42S4 and Whitey, Cat. No. SS-41S2 both capable of temperatures up to 65°C. These were later replaced with higher temperature valves (Swagelok, Cat. No. SS-60) at the vacuum pump isolation valve (VIV) except for the FIV which is not heated. The needle valves (Whitey Cat. No. SS-1RS4) above the accumulator are capable of operation up to 232°C. The handles of the heated valves were replaced with phenolic valve stems preventing additional heat loss or cold spots.

3.7 Controllers and panel wiring

Due to the number of heated components in the system, they were grouped into four heating zones (Fig. 12).

A dedicated temperature controller and control thermocouple (denoted as CTx) was assigned to each zone.

The controller (Omega Cat. No. CSi-3222) for each zone has two outputs and one input which is attached to the control thermocouples. One of the outputs is 5 VDC from an internal solid state relay (SSR) while the other output is from an internal mechanical relay. Because the output voltages are not sufficient to power the heaters directly, each

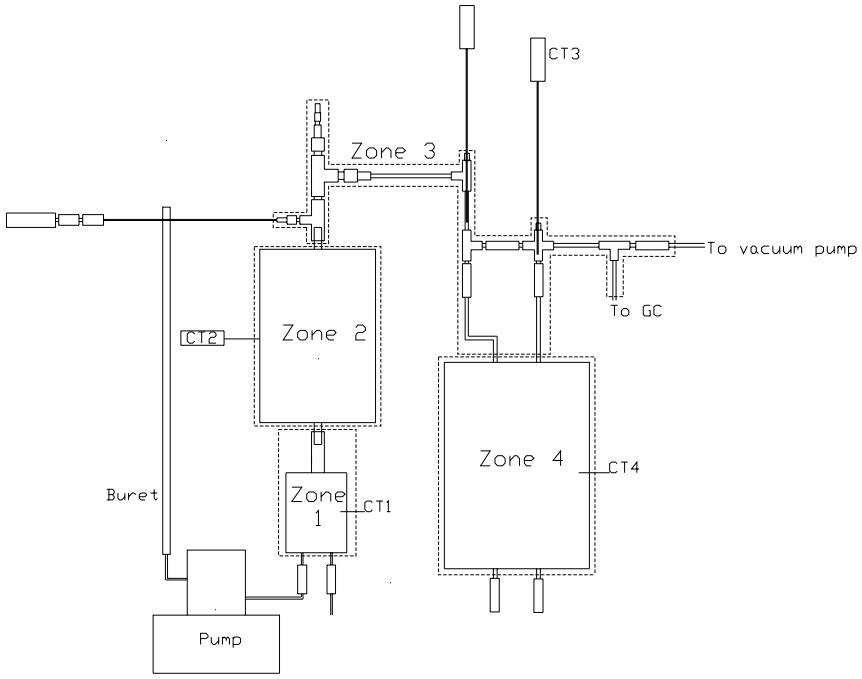

Figure 12: Schematic of reactor panel illustrating boundaries of the four heating zones.

Zone	Associated Component	Control Temperature (°C)
1	Evaporator	273
2	Reactor	250-500
3	Outlet plumbing	206
4	Accumulator	215

Table 3: Panel operating temperatures.

controller output is used to switch a SSR applying 120 VAC to the heaters. The wiring diagrams for the four heating zones appear in Fig. 13. The 120 VAC power supply switched by the relays comes from the building with a maximum current of 30 A.

Two additional controllers monitor the pressure transducer signal output. The digital readout was calibrated to units of kPa. The wiring diagram for the pressure gauges appear in Fig. 14. Output 1 of the controller provides a 10 V excitation voltage to power the pressure transducer.

3.8 Vent hood and fume curtain

A sheet metal vent hood was designed and built to cover the top of the reactor panel. Flexible ducting (McMaster Carr, Cat. No. 87815K71) was used to connect the top of the vent hood to the room ventilation purge system. Silicon-coated fiberglass fabric (McMaster Carr, Cat. No. 87815K71) with thickness of 0.017 inch was hung from a rod

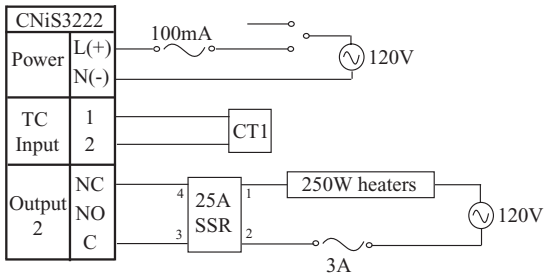

(a) Zone 1: Evaporator

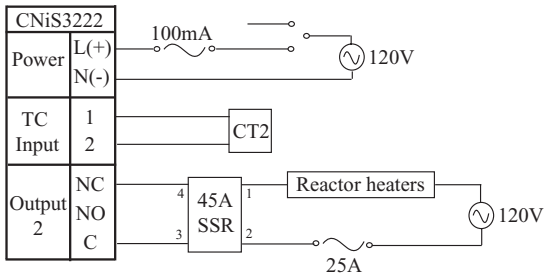

(b) Zone 2: Reactor

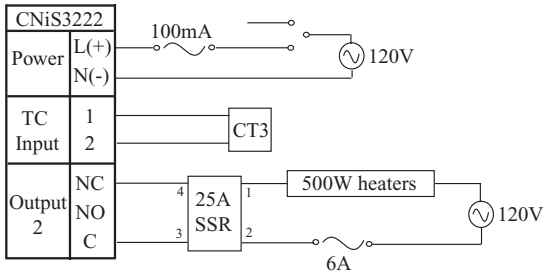

(c) Zone 3: Outlet plumbing

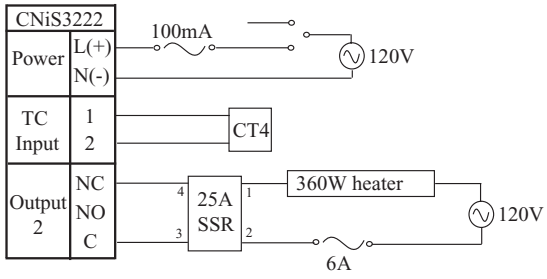

(d) Zone 4: Accumulator

Figure 13: Wiring diagrams for the four heating zones.

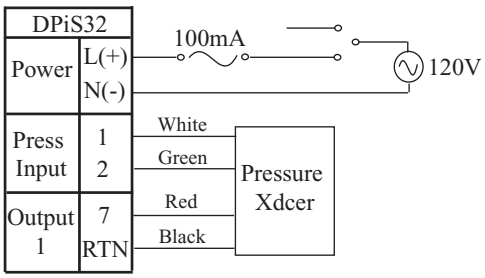

Figure 14: Wiring diagram for electronic pressure gauges.

around the perimeter of the vent hood to contain the fumes under the hood area. Fumes were generated by the panel components as a result of heater and insulation outgassing. Additional fumes due to the vaporized JP-10 were exhausted through the top of the vent hood after passing through the cold trap located at the exhaust of the GC sampling loop.

3.9 Gas bottles and regulators

A bottle rack capable of holding up to six bottles was built and attached to the wall behind the reactor panel. The gas chromatograph required a total of three different gases. The carrier gas was ultra-high-purity helium and required an analytical regulator (Math-

eson Cat. No. 3122-580) capable of supply pressures up to 200 psi. It was regulated to a pressure of 80 psi. An oxygen trap (Agilent, Cat. No. 3150-0414) was installed on the helium line just upstream of the GC to remove water vapor which can damage the capillary column during high-temperature operation. The GC's detector required a supply of ultra-zero air and ultra-high-purity hydrogen each with regulators capable of supply pressures up to 200 psi (Matheson, Cat. No. 3122-580 and Matheson, Cat. No. 3120-350). The ultra-zero air was regulated to a pressure of 80 psi while the hydrogen was regulated to a pressure of 60 psi. Specification of these pressures appears in the "Agilent Site Prep and Installation Guide" documentation. A Matheson flame arrestor was added to the ultra-high-purity hydrogen line just downstream of the regulator.

A bottle of industrial nitrogen with a general purpose regulator (Matheson, Cat. No. 9-580) was attached directly to the system plumbing through the GIV. A bottle of industrial air with a general purpose regulator (Matheson, Cat. No. 19-590) was attached directly to the bottom of the accumulator via a venting regulator as previously mentioned.

4 Gas chromatograph

The reactor panel outlet was connected to a capillary gas chromatograph (Agilent 6890 Series) for product component analysis. Connections to the GC appear on the right side of the reactor panel (Fig. 9) upstream of the VIV. The capillary column has a stationary phase of HP-5 (crosslinked 5% Phenyl Methyl Siloxane, Model HP 19091J-433) with dimensions of 3 m $\times$ 0.32 mm $\times$ 0.25 μm column. The column temperature limits are -60 to 325°C. A flame ionization detector quantified the column effluent.

4.1 GC theory

Chromatography [25] is the method of separating a volatile sample into its individual components. Separation occurs due to variations in the individual component distributions between two phases that are contained in the column. In capillary columns, the carrier gas and sample constitute the mobile phase while the solid, stationary phase is coated on the column's inner surface. As the sample and carrier gas travel through the column, the sample components are retarded due to their affinity for the stationary phase. This affinity is a dynamic process where the average concentrations of the component molecule in the mobile and stationary phase are defined by the distribution law.

$$K = \frac{C_S}{C_M} \tag{1}$$

This distribution coefficient K can be related to the fraction of time a molecule spends in the mobile phase τ_M by considering the relative volumes of the two phases.

$$\tau_M = \frac{C_M V_M}{C_M V_M + C_S V_S} = \frac{1}{1 + K(V_S/V_M)} \tag{2}$$

The linear velocity u of the mobile phase is an operating parameter specified by the user. Thus, the rate U at which a component molecule travels through the column varies with this linear velocity of the mobile phase.

$$U = u\ \tau_M \tag{3}$$

From the above equations, the rate of travel of a sample component then depends on three factors: the carrier gas velocity u, the volume ratio between the stationary and mobile phases V_S/V_M, and the distribution coefficient K. Only the distribution coefficient is different for each component in the same sample and is responsible for the component's varying rates of travel. For a constant length column, different components elute at different times as a result of their varying rates of travel through the column. The component elution order is typically in the order of increasing boiling points when Raoult's law applies [26]. The time at which a sample component elutes from the column is its retention time.

$$t_R = \frac{L}{U} \tag{4}$$

Ideally, at a component's retention time, all of the sample component elutes in the same volume or time interval as it was injected into the inlet [27].

$$A = \int_{I}^{II} S dt \tag{5}$$

The detector records the component elution as a spike with height proportional to the injected amount (Fig. 15a).

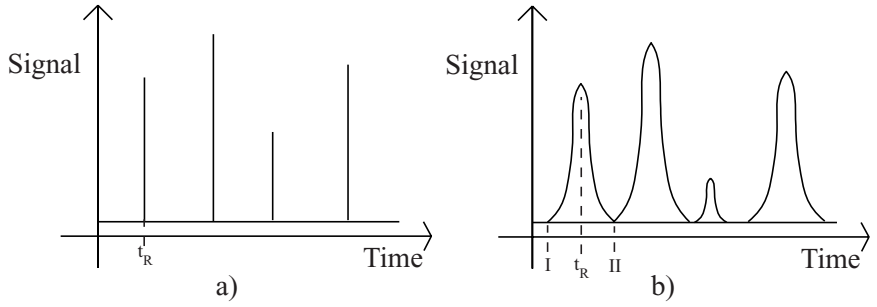

Figure 15: Detector output for a) ideal operation and b) real operation with peak broadening.

However, in actual operation dispersion of the molecules causes deviations from this ideal behavior. As the component travels through the column, it diffuses causing a broadening of the detector signal (Fig. 15b). In cases of significant peak broadening, signal analysis can be difficult because overlapping peaks at similar retention times prevent accurate integration of the area under each peak. The column resolution R_c refers to the degree of separation of two components that leave the column shortly after each other. This can be quantified by comparing the two retention times and the variance of the eluted peak.

$$R_c = \frac{t_{R2} - t_{R1}}{4\sigma_2} \tag{6}$$

Where σ_2 refers to the peak width at half height divided by 2.357 [25]. The resolution can be improved by decreasing the sample size. Suggested sample sizes for capillary columns should be smaller than 10^{-7} gr [25] corresponding to less than $7{\times}10^{-6}$ μl of JP-10. Many other parameters can be specified in capillary column operation such as separation number, plate number, holdup time, etc. These have not been quantified in this study as they are for a more theoretical study of the GC operation than is required to understand the measured results. Due to the size of our experimental facility, sample injections are often too large resulting in GC operation that is not optimal. The effect of large sample injections may be eliminated or reduced by increasing the sample dilution or using a split injector. These methods were attempted with our system as is discussed in section 5.1 and 5.2.

4.2 Flame ionization detector

There are many detectors that may be used in conjuction with a gas chromatograph. After the sample components are separated, the detector that is attached to the end of the column provides the quantitative measurement of the sample amount. The detector then measures the time of elution from the sample injection and determines the quantity of the sample at each particular retention time.

There are two classes of detectors: those in which the detector response depends on the sample concentration and those in which the detector response depends on the mass flowrate of the sample and is concentration independent [28]. Figures of merit for the detectors include sensitivity, detectability, specificity, linearity, and response time. The two most popular detectors are the flame ionization detector (FID) and the thermal conductivity detector (TCD).

The FID is the universal detector of organic compounds and considered the most versatile of the high sensitivity detectors [25]. A diffusion flame, created by burning hydrogen in air, burns the sample components as they elute from the column. Electrons and positive ions are produced by the process of chemi-ionization in which the major ion formed is the hydronium ion (H_3O^+) [28]. By applying a voltage differential across the flame, a measurement of the number of electrons can be made in units of pA. Many generations of FID configurations have resulted in the current configuration where a parallel plate electrode system is used with a non-conducting jet [25]. As a result, only the gas flowrates may be controlled by the users but suggested values appear in the Agilent support documentation.

The TCD detector is less sensitive but can be used with a wider range of species than the FID. The sensitive element is a thin wire or filament that is operated in either a constant current or constant temperature mode. Heat transfer from the wire to the sample eluting from the column will depend primarily on the thermal conductivity of the sample, which is a function of the sample molar mass and molecular structure. When the sample has a thermal conductivity significantly higher or lower than the carrier gas, the detector filament resistance or current demand will change and this is registered by the bridge circuit and electronics connected to the detector. The response of the TCD at a specific retention time to a given component is directly proportional to its concentration, velocity, and inversely proportional to its specific heat. Unlike the FID, the TCD is sensitive to H_2, O_2, and N_2 in addition to the organic compounds. One disadvantage of the TCD is that it is less sensitive than the FID by a factor of 10^5 [29].

Detector theory is described in a number of sources on chromatography and should be referred to for a more detailed discussion of detector design and operation.

4.3 Agilent GC and associated hardware

This section discusses the hardware required for GC operation. The GC oven is fast-heating requiring a dedicated power supply of 240 V and 15 A. Plumbing for the helium, air, and hydrogen is attached to the connections on the back of the GC with 1/8-inch

refrigeration grade copper tubing. Building supply air regulated to 40 psi operated the gas sampling valve.

A Hewlett-Packard computer containing the ChemStation interfacing software was connected to the GC with a LAN connection. The network connection is established between the computer and GC with a "bootp" server which establishes the network IP address of the GC upon startup. A second network card was installed in the computer allowing it to be connected to the department computer network.

4.4 ChemStation software

The ChemStation software is a user interface enabling the GC operating parameters, system configuration, data analysis, and report generation properties to be specified. The software is organized into three main "views" that group common functions and operations together.

4.4.1 Method and run control

Method and Run Control is the first view where the GC is configured, system operating parameters are specified, runs are begun, and the data is acquired. The sum of these settings are stored into a file called a method. Thus, a method is comprised of all the data acquisition and analysis parameters specific to a given sample. A description of the important submenus within the Method and Run Control view follow.

The sample name and filenames for the detector signal output are specificed in the Sample Information menu. System operating parameters, specified in the submenus of the Edit Parameters menu, are discussed below.

The Valve Configuration menu specifies the operating parameters for the gas sampling valve (Table 4). These parameters are used when Gas Sampling Valve is selected from the

Configured:	Gas Sampling
Loop Volume [ml]:	0.25
Loop Time [min]:	0.10
Inject Time [min]:	0.10

Table 4: Edit Parameters - Valve Menu.

Injection Source pull down menu. The 0.25 ml sampling loop was installed on the GC and is the smallest loop volume provided by Agilent. The sample loop volume determines (or controls) the amount of sample introduced onto the column. Thus, reducing the sample loop volume is a means of sample size reduction which can help eliminate problems of column saturation.

As mentioned in section 4.3, building supply air regulated to 40 psi was used to operate the pneumatic sample valve as it switches between two positions (Fig. 16). The default setting is shown in Fig. 16 and is referred to as the LOAD position. In this position, the column and sample loop are not connected. The carrier gas enters the column at position

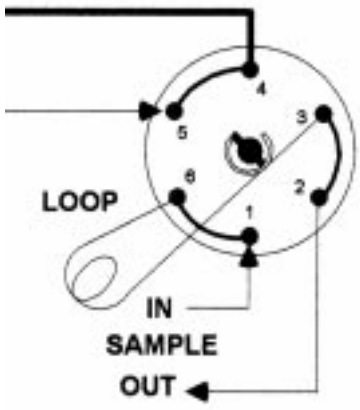

Figure 16: Agilent schematic of gas sampling valve in the LOAD position. Copied from Agilent paperwork provided with the GC.

5 as denoted by the arrow and exits the valve through position 4 which leads to the inlet and column. The isolated sample loop is located between positions 3 and 6. In this configuration, the sample gas can be flushed through the sample loop without contacting the column until the valve switches into the INJECT position. From the LOAD position to the INJECT position, the valve moves such that the carrier gas inlet is now applied to position 1 and exits through position 2 into the inlet and column. Thus, the sample gas contained in the sample loop volume just before the valve switches into the INJECT position is trapped and injected onto the column by the redirected carrier gas. The gas sampling valve is an easy way to produce repeatible injections of gaseous samples. Gas syringes, which inject the gas sample directly into the column as in a manner similar to the liquid injections, may also be used. The results in this study with gas injection were completed using only the GC gas sampling valve.

Liquid samples are analyzed by specifying the Manual option from the Injection Source pull down menu. A syringe injects the sample through a septum directly into the inlet. The high temperature septum is self-sealing but should be replaced every 10-15 injections. An Agilent syringe of 10 μl capacity was provided with the system.

Table 5 shows typical operating settings used in this study for the inlet while Table 6 shows the column settings. These two sections are discussed together as some of the settings are dependent.

Heater [°C]:	250
Pressure [psi]:	8.75
Split Ratio:	400:1
Split Flow [ml/min]:	800
Total Flow [ml/min]:	805

Table 5: Edit Parameters - Inlet Menu.

Mode:	Constant Pressure
Pressure [psi]:	8.75
Flow [ml/min]:	2.0
Average Velocity [cm/sec]:	32

Table 6: Edit Parameters - Column Menu.

The inlet is capable of operation in split or splitless modes. In splitless mode, all of the sample is introduced onto the column. In split mode, only a user specified fraction of the sample is introduced onto the column (Split Ratio = Split Flow / Column Flow) and the remainder is purged from the GC. Thus, split operation is a simple means of sample dilution. By setting the split ratio and the column flowrate, the split flow and the total flow are constrained. The total flow is calculated by adding 3 ml/min for the purge flow to the sum of the user specified column flow and split flow. The purge flow exhausts through a port on the top of the GC. The inlet pressure is constrained by the used specified column flow and the column dimensions. The average column velocity is calculated from the flow, pressure, and column dimensions.

As suggested for capillary columns, the flowrate was set to 2.0 ml/min. This flowrate affects how fast the sample elutes from the column and should be optimized to achieve adequate peak separation without excessive peak broadening.

The inlet temperature should be set approximately 20°C greater than the highest boiling point temperature of the sample components. Additionally, a program specifies the temperature control of the oven containing the column (Fig. 17). Ramping the column temperature promotes component separation and orders the elution times by their boiling point temperatures.

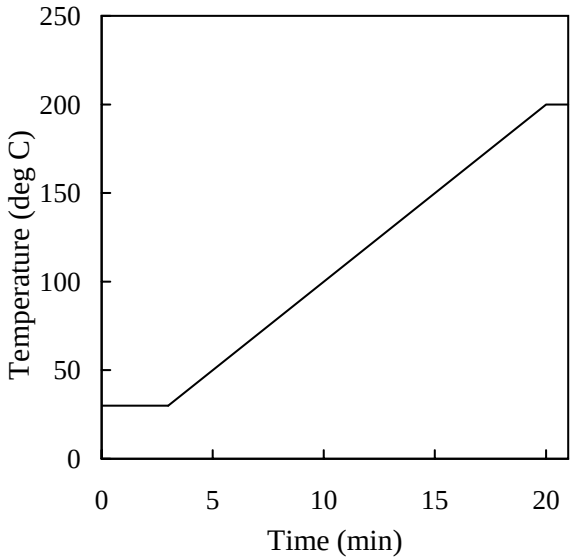

Figure 17: Temperature versus time plot of the GC oven program.

The Detector menu allows for specification of the flowrate for the supply gases to the FID (Table 7). These parameters were suggested by the Agilent support documentation.

Heater [°C]:	250
H_2 Flow [ml/min]:	40
Air Flow [ml/min]:	450
Makeup Flow [ml/min]:	45
Flame:	ON
Electrometer:	ON

Table 7: Edit Parameters - Detector.

After flame ignition, a period of time (approximately 10 minutes) is required for signal stabilization to a baseline value of approximately 10-15 pA. It is possible for the flame to have ignition problems after periods of inoperation. In this case, the Lit Offset parameter may be increased from its default of 2.0 pA to a higher value (i.e., 10 pA). This parameter is a signal threshold that the software uses to establish whether flame ignition has occurred.

In the Signal menu, it is specified that the FID output signal is to be recorded at a sampling frequency of 20 Hz. The Aux menu specifies an auxiliary heater temperature of 250°C. This is the auxiliary heater for the gas sampling valve.

4.4.2 Data analysis and report generation

The auto-integrator in the ChemStation software was used to complete the signal integrations for each run. These results were tabulated into a report and printed out with the chromatogram for each run. The reported data consist of the retention time, peak area, and peak symmetry.

4.4.3 Column conditioning and maintence

Maintence procedures included ensuring there is a continuous supply of carrier gas flowing through the column, periodically conditioning the column, and replacing the inlet septum regularly.

The purpose of column conditioning is to clean the column at high temperature and to flush retained components out of the stationary phase. This is conducted by flowing only the carrier gas through the column while ramping the oven temperature to the maximum column temperature and holding at this temperature for at least 30 minutes. The procedure to replace the inlet septum is found in the Agilent documentation.

5 Characterization tests

The following sections discuss the initial tests conducted to understand operation of the GC, the reactor panel, and the combined system. These characterization tests include GC analysis with liquid and gas injection, quantification of system leak rates, and system vapor pressure measurements with JP-10. The GC samples with liquid and gas injection are referred to by a standardized naming convention as shown in Tables 8 and 11. The test ID consists of a number and letter. The numbers refer to the date of the test and the letters refer to the order of samples taken that day. For example, test ID 011102A means it is the first sample taken on January 11, 2002.

5.1 Chromatography with liquid injection

Learning how to use the GC began by analyzing samples using liquid injection. The effect of changes in the operating parameters on the resulting signal were investigated. This primarily included the effect of sample dilution on peak width, peak separation, and peak symmetry. Sample sizes of 1 μl can be injected with a syringe into the inlet with acceptable repeatibility. Injection procedure can significantly affect the time duration in which the sample is introduced to the inlet and is one of the biggest causes of error in practice [26].

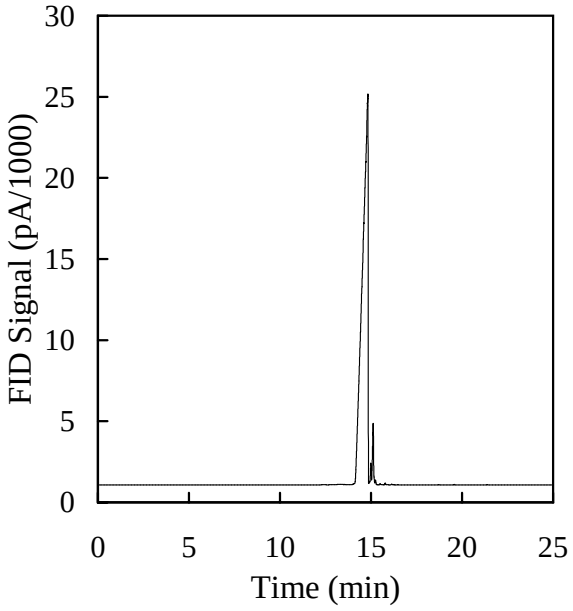

Figure 18: GC chromatograph with liquid injection of 1μl of JP-10.

Liquid injection of 1 μl of JP-10 into the inlet resulted in significant peak fronting indicative of column saturation (Fig. 18). Such peak asymmetry causes a ficticious delay in the retention time. This retention time delay is most prominent in tests 011602A through F of Table 8. A series of tests was conducted to dilute the JP-10 sample in

hexane to obtain a symmetric chromatogram, thus obtaining an idea of the required dilution for meaningful output signals. Required dilutions were on the order of 0.05% wt JP-10 in hexane in a 1μl sample. This is observed in the tests labeled 012102A and B of Table 8.

5.2 Chromatography with gas injection

The initial GC tests using the gas sampling valve were completed by sampling from the closed accumulator that was heated to approximately 90°C and filled with a hydrocarbon-nitrogen mixture. The effect of loop and inject time were investigated (Table 11). Residual hydrocarbon, especially JP-10, in the plumbing was observed and difficult to flush from the system as evidenced by tests where no hydrocarbon was injected. The system was flushed between each test.

Due to the length of line connecting the outlet of the reactor panel to the sampling valve, the time required to flush the line was determined by measuring the flowrate out of the sample loop as a function of accumulator pressure (Fig. 19). This was done by measuring the water displaced from an overturned beaker.

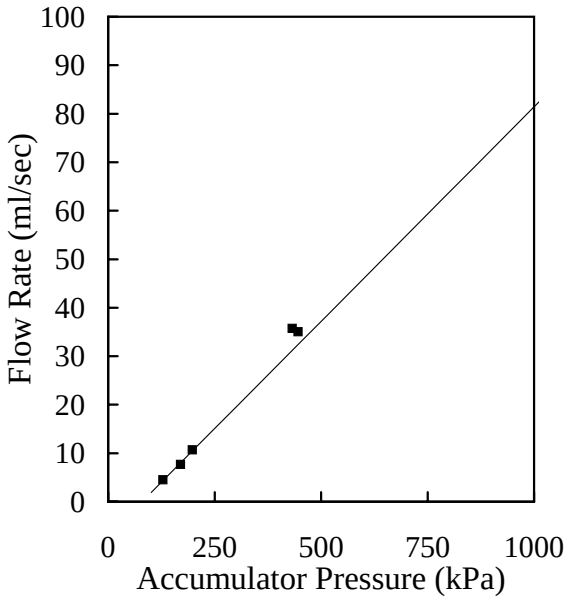

Figure 19: flowrate through the GC sampling valve as a function of accumulator pressure.

The alkanes between C_5 and C_{12} in addition to JP-10 were analyzed to determine their retention times. An overlay of the output chromatograms appears in Fig. 20.

A list of the samples tested along with their boiling temperatures and measured retention times appears in Table 9. The retention times are ordered by boiling temperatures (Fig. 21) as expected, which is a product of the oven program (Fig. 17).

Boundaries defining regions in which compounds with the same carbon number are expected to elute from the column also appear in Fig. 20. The boundaries are listed in

Test ID	Compound Description	Column Press (psi)	Column Flow (ml/min)	Split Ratio	Start Temp (°C)	End Temp (°C)	Ret. Time (min)
011102A	1μl JP-10	4.87	1.0	20:1	30	250	14.826
011202A	0.5μl JP-10	4.87	1.0	20:1	30	250	14.544
011202B	0.1μl JP-10	4.87	1.0	20:1	30	250	14.226
011202C	0.1μl C_5H_{12}	4.87	1.0	20:1	30	250	3.384
011202D	0.1μl C_7H_{16}	4.87	1.0	20:1	30	250	6.164
011602A	0.5μl JP-10	8.75	2.0	10:1	30	250	12.097
011602B	0.5μl JP-10	8.75	2.0	25:1	30	250	11.908
011602C	0.5μl JP-10	8.75	2.0	75:1	30	250	11.697
011602D	0.2μl JP-10	8.75	2.0	100:1	30	250	11.511
011602E	0.2μl JP-10	8.75	2.0	88:1	30	250	11.513
011602F	0.2μl JP-10	8.75	2.0	125:1	30	250	11.590
011702A	1μl, 5% wt	8.75	2.0	25:1	30	230	11.657
011702B	0.2μl, 5% wt	8.75	2.0	25:1	30	200	11.555
011702C	0.2μl, 5% wt	8.75	2.0	40:1	30	200	11.543
011702D	0.2μl, 1% wt	8.75	2.0	40:1	30	200	11.501
011702E	0.2μl, 0.5% wt	8.75	2.0	40:1	30	200	11.502
011702F	0.2μl, 0.3% wt	8.75	2.0	40:1	30	200	11.496
011702G	0.2μl, 0.1% wt	8.75	2.0	40:1	30	200	11.492
011702H	0.2μl, 0.3% wt	8.75	2.0	40:1	30	200	11.494
011702I	0.2μl, 0.5% wt	8.75	2.0	40:1	30	200	11.494
011702J	0.2μl, 1% wt	8.75	2.0	40:1	30	200	11.501
012102A	1.1μl, 0.05% wt	8.75	2.0	40:1	30	200	11.496
012102B	1.05μl, 0.05% wt	8.75	2.0	25:1	30	200	11.494
012102C	1μl, 0.03% wt	8.75	2.0	25:1	30	200	11.491
012102D	1μl, 0.01% wt	8.75	2.0	25:1	30	200	11.495
012302A	1.05μl, 0.1% wt	8.75	2.0	25:1	30	200	11.496
012302B	0.6μl, 0.3% wt	8.75	2.0	40:1	30	200	11.497
012302C	0.8μl, 0.3% wt	8.75	2.0	40:1	30	200	11.501
012302D	0.8μl, 0.3% wt	8.75	2.0	40:1	30	200	11.497
012302E	0.8μl, 0.3% wt	9.14	2.0	40:1	40	200	10.280
012302F	0.8μl, 0.1% wt	8.75	2.0	40:1	30	200	11.496
012302G	0.6μl, 0.1% wt	8.75	2.0	50:1	30	200	11.502

Table 8: Summary of all GC characterization tests with liquid injection. Tests with specified dilutions were made with JP-10 in hexane. Refer to Tables 4 - 7 for GC operating conditions not specified here.

Table 10. Woodrow [30] used this technique as a means of quantifying product composition since detailed component analysis is not possible with an FID. The FID gives a

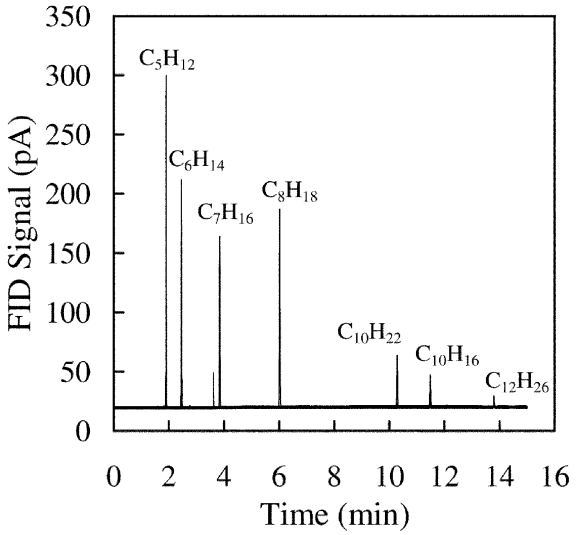

Figure 20: Sample chromatogram of gaseous injection samples of alkanes and JP-10 with region boundaries.

Compound	Formula	Boiling temperature (°C)	Retention time (min)
Pentane	C_5H_{12}	36	1.900
Hexane	C_6H_{14}	69	2.457
Heptane	C_7H_{16}	99	3.849
Octane	C_8H_{18}	126	6.022
Decane	$C_{10}H_{22}$	174	10.296
JP-10	$C_{10}H_{16}$	193	11.494
Dodecane	$C_{12}H_{26}$	216	13.800

Table 9: Boiling temperature and retention times of tested compounds.

.

signal which is proportional to the number of carbon atoms that are eluting at a given time. By integrating the signal over a range of retention times, the resulting area $Area_i$ under the FID signal is proportional to the number of carbon atoms $n_{C,i}$ in that region.

$$Area_i \propto n_{C,i} \tag{7}$$

The areas assigned to retention times in each region are summed. The summed areas in each region are divided by the summed areas in all regions,

$$\frac{Area_i}{\sum_i Area_i} \propto \frac{n_{C,i}}{\sum_i n_{C,i}} = x_i \ , \tag{8}$$

resulting in an associated mole fraction x_i of *carbon atoms* for each region of FID signal integration. Since the FID only determines the number of carbon atoms this is also the

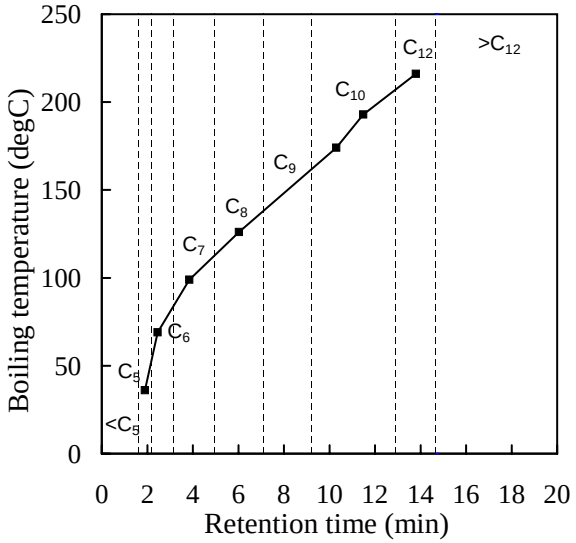

Figure 21: Boiling temperature of alkanes and JP-10 versus measured retention times.

Formula	Start Time (min)	End time (min)
$<C_5$	0	1.622
C_5	1.622	2.179
C_6	2.179	3.153
C_7	3.153	4.936
C_8	4.936	7.091
C_9	7.091	9.228
C_{10}	9.228	12.924
C_{12}	12.924	14.676
$>C_{12}$	14.676	20

Table 10: Region boundaries for peak summation of compounds with same carbon number.

mass fraction y_i for that region.

$$y_i = \frac{m_{C,i}}{\sum_i m_{C,i}} = \frac{12 \text{ g/mol} \cdot \text{n}_{\text{C,i}}}{\sum_i 12 \text{ g/mol} \cdot \text{n}_{\text{C,i}}} = x_i \tag{9}$$

The resulting *carbon* mass fraction is what is being reported in the subsequent sections of this report. We report this instead of number density or mass fraction of a particular species since since we don't know exactly what the species are that are being eluted. Speciation would require further analysis by a GC/MS. Although we have calibrated the retention times with pure hydrocarbon test species, the actual reactor products will involve species other than those used for calibration.

Reactor product species are not assured to be ordered in terms of the carbon number in exactly the same fashion as the calibration species. Reducing the the FID output

in terms of carbon mass instead of species amount eliminates possible over or under counting of species in this situation. The ratio of hydrogen to carbon is also not known for the reactor products. While this only makes a modest difference in determining the molar mass, it prevents us from precisely determining the mass fraction on a species basis. Since C is 12 times heavier than H, as long as the H/C ratio does not vary too wildly, then the carbon mass ratio distribution will be similar to the actual species mass distribution.

In conclusion, without a great deal of further analysis, what the FID reports is proportional to the mass of carbon atoms. The data reduction does not account for the hydrogens and the reported mass fraction y_i is strictly on a carbon-only basis.

Test ID	Compound Description	Loop Time (min)	Inject Time (min)	Split Ratio	Start Temp (°C)	End Temp (°C)	Ret. Time (min)
012402A	0.1μl JP-10, 52 psi N_2	0.25	0.25	40:1	30	150	11.572
020102A	1μl Vial G, 42 psi N_2	0.25	0.25	40:1	30	150	11.540
020102B	No JP-10, 48 psi N_2	0.25	0.25	40:1	30	150	11.550
020202A	No JP-10, 50 psi N_2	0.25	0.25	40:1	30	150	11.522
020202B	No JP-10, 48 psi N_2	0.25	0.25	40:1	30	150	None
020402A	No JP-10, 45 psi N_2	0.05	0.05	40:1	30	150	11.494
020502A	No JP-10, 48 psi N_2	0.05	0.05	40:1	30	150	11.492
020502B	No JP-10, 48 psi N_2	0.05	0.05	40:1	30	150	11.494
020502C	17.4μl JP-10, 40 psi N_2	0.05	0.10	40:1	30	150	11.494
020502D	No JP-10, 40 psi N_2	0.05	0.10	40:1	30	150	11.490
020502E	17.4μl JP-10, 40 psi N_2	0.05	0.10	40:1	30	150	11.488
020502F	17.4μl JP-10, 41 psi N_2	0.05	0.10	40:1	30	150	11.499
020502G	17.4μl JP-10, 43 psi N_2	0.05	0.10	40:1	30	150	11.498
020602A	No JP-10, 40 psi N_2	0.05	0.10	40:1	30	150	11.486
020602B	No JP-10, 40 psi N_2	0.10	0.10	40:1	30	150	11.487
020602C	17.4μl C_6H_{14}, 40 psi N_2	0.10	0.10	40:1	30	150	2.457
020602D	17.4μl C_5H_{12}, 40 psi N_2	0.10	0.10	40:1	30	150	1.900
020602E	17.4μl $C_{10}H_{22}$, 40 psi N_2	0.10	0.10	40:1	30	150	10.284
020602F	17.4μl C_7H_{16}, 40 psi N_2	0.10	0.10	40:1	30	150	3.849
020602G	17.4μl $C_{12}H_{26}$, 40 psi N_2	0.10	0.10	40:1	30	150	13.800
020702A	No JP-10, 40 psi N_2	0.10	0.10	40:1	30	150	11.499
020702B	17.4μl $C_{10}H_{22}$, 40 psi N_2	0.10	0.10	40:1	30	150	10.296
020702C	17.4μl C_8H_{18}, 40 psi N_2	0.10	0.10	40:1	30	150	6.022

Table 11: Summary of all GC characterization tests with gas injection. Refer to Tables 4 - 7 for GC operating conditions not specified here.

5.3 Leak testing

Initial leak testing was performed on the accumulator only, as mentioned above in the accumulator discussion. As it was received from Advanced Projects Research, Inc., the leak rate was 262.3 sccm. Honing the internal cylinder surface and replacing a plug on the top flange resulted in reducing the leak rate to 2.63 sccm.

Leak tests of the reactor panel plumbing without the accumulator yielded a leak rate of 0.39 sccm. This measurement was obtained by filling the system with helium to a pressure of 200 psi and recording the pressure over time. The system was primarily operated at or near atmospheric pressure so this value is assumed to be an upper bound on the leak rate. However, due to repeated removal and replacement of the central reactor tube, some variation in the leak rate is expected. The leak rate was not quantified before each thermal and catalytic cracking test.

5.4 Temperature distribution

The temperature uniformity of the original system (Fig. 7) was monitored over time on three separate days. The first two heating tests were at temperatures lower than the intended operating temperatures. A third heating test at operational temperatures

TC	1	2	3	4	5	6	7	8	9a	10
9/20/01	50	51	56	49	38	60	53	48	43	-
9/28/01	68	67	63	65	45	104	93	96	58	-
10/11/01	192	218	218	220	209	282	270	257	144†	70

Table 12: Reactor system temperature distribution in °C. Thermocouple positions refer to numbers on Fig. 7. † For the Oct. 11 test, the thermocouple in position 9a was moved to the connection between the reactor system and the GC denoted by position 9b in Fig. 7.

measured a maximum temperature difference in the evaporator section of 28°C. Even heating with the rope heaters over the smaller diameter tubing and many Swagelok connections was difficult.

5.5 JP-10 Vapor Pressure

Previous experiments [31, 32, 33] have measured the vapor pressure of JP-10 over different temperature ranges. We have combined this data onto one graph as shown in Fig. 22. The data from Caltech was measured using documented methods that involve removing the dissolved oxygen from the liquid fuel [34]. A linear correlation was derived based on the approximate Clausius-Clapeyron equation.

$$\left(\frac{dP}{P}\right)_{sat} = \frac{H_{fg}}{R}\left(\frac{dT}{T^2}\right)_{sat} \tag{10}$$

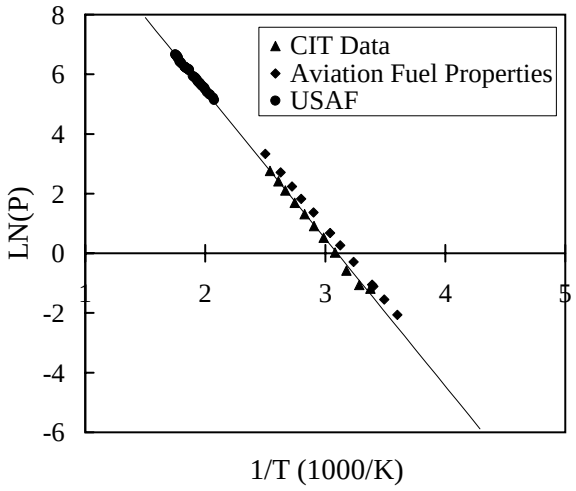

Figure 22: Experimental JP-10 vapor pressure data with correlation given in Eq. 12.

This equation is integrated and the two unknowns (H_{fg} and integration constant C) are calculated given the experimental data of Fig. 22.

$$P_{sat} = C \exp\left(\frac{-\Delta H_{fg}}{RT_{sat}}\right) \tag{11}$$

This yields the vapor pressure and temperature relation for JP-10 (Eq. 12). This relation is valid for temperatures between 5 and 315°C based on the available experimental data. The correlation is extrapolated for temperatures outside this range.

$$P_{sat} = 4.46 \times 10^6 \exp\left(\frac{-302}{RT_{sat}}\right) \tag{12}$$

where P_{sat} is in units of kPa, T_{sat} is in units of K, and R is 0.0611 kJ/kg $\cdot$ K for JP-10.

This equation is tabulated showing the expected pressure rise for a range of temperatures assuming the system contains enough JP-10 to reach the saturation point (Table 13). To reach the intended system operating pressure of 200 psi, the system must be heated to a minimum of 340°C. Because the maximum operating temperature of most panel components is 200°C, the maximum absolute operating pressure experimentally possible in the system is 19 psi. For simplicity, the system (with a nominal temperature of 200°C) was operated at an absolute system pressure between 104 and 111 kPa (15.1 and 16.1 psia). Since no back pressure was applied to the bottom of the accumulator piston (i.e. the venting regulator was set so that no additional pressure was applied to the bottom of the accumulator), the system pressure increase over the ambient value amounted to only 3 to 10 kPa (0.1 to 1.5 psi). This pressure increase is a result of the force required to overcome the friction of the piston seal and force the piston down.

Temperature (°C)	Pressure (kPa)	Pressure(psi)
180	82	12
190	104	15
200	130	19
210	161	23
220	198	29
230	242	35
240	293	43
250	353	51
260	421	61
270	499	72
280	589	85
290	690	100
300	804	117
310	932	135
320	1075	156
330	1235	179
340	1411	205
350	1606	233

Table 13: Tabulated vapor pressure data using Eq. 12.

6 Methods of data acquisition, analysis, and reduction

Running the reactor system and GC involve a standard set of operations described below. The data analysis is also described here as well as the methods applied to obtain the data of the results sections which follow.

6.1 Test procedure

This section describes the test procedure for thermal or catalytic reaction of JP-10 and the subsequent analysis by the GC. Generally, the test procedures are the same between the two tests except for a few noted exceptions.

Preparations for testing primarily consisted of heating the reactor panel components to the desired operational temperatures (Table 3). The heating process for a thermal cracking test was different than a catalytic cracking test because of the installed zeolite.

Prior to a thermal cracking test, the temperature controllers for the four heating zones were turned on and the desired set point entered. Constant power was supplied to the heaters, bringing the system up to operating temperature (a reactor temperature of 500°C) in approximately 6 hours.

Prior to a catalytic cracking test, the zeolite was installed into the central reactor tube, and the temperature controllers for the four heating zones were turned on. The desired set point was entered for zones 1, 3, and 4. The RAMP function of the controller was used to heat zone 2 containing the reactor. The zeolite requires a temperature rate increase less than 5°C/min to prevent destruction of the zeolite framework. Additionally, the zeolite absorbs water vapor from the environment which must be removed from the active sites freeing them for reaction with the sample hydrocarbon. This process is completed by holding the zeolite at an elevated temperature (250°C) in a dry, inert environment for 4 hours. Thus, the heating process for the catalytic cracking tests begins by flowing nitrogen through the system and ramping from room temperature to 250°C at a rate of 2.7°C/min. This takes approximately 2.5 hours. Zone 2 is then held at 250°C for 4 hours followed by a second temperature increase at a rate less than 5°C/min to the desired operating temperature. Because of heat loss from the reactor casing to the surroundings, it took 4 to 5 hours for the temperature to increase from 250 to 500°C.

The controllers do not have the option of programming multiple temperature ramp and soak routines. Thus, the second temperature ramp had to be manually initiated. After several long testing days, the first temperature ramp and soak was started at midnight, and the second temperature ramp was started at 7:00 AM so the system was ready for testing by noon.

The GC was prepared once the reactor panel was close to its operating temperature. Preparing the GC consisted of specifying the run parameters as previously discussed and igniting the FID. The FID output was checked for baseline stability.

When both the reactor panel and GC were ready for testing, the system plumbing was evacuated with the attached vacuum pump to eliminate as much residual JP-10

as possible. Valves A2 and A3 were closed (Fig. 9). Then nitrogen was added to the system through the GIV until a pressure of 104 kPa was obtained. This provided the required backpressure on the fuel pump. The FIV was opened and stability in the buret liquid level was verified. Concurrent with starting the fuel pump, the time, buret liquid level, system pressure, and accumulator position were recorded. These parameters were recorded throughout the duration of the test and comprise the results presented in a later section.

Each test was stopped by taking a final record of the time, buret liquid level, system pressure, and accumulator pressure; then the fuel pump was shut off and the FIV closed. Valve A1 was then closed, isolating the products inside the accumulator. A baseline run was conducted with the GC by taking a gas sample from the evacuated plumbing between the GC and valve A3. Prior to taking the first sample from the accumulator, approximately 240 kPa of backpressure was applied to the bottom side of the accumulator. This backpressure established flow through the sample loop once valve A3 was opened. Valve A3 was held open and the products were allowed to flow through the sample loop for at least 3 seconds before the GC run was started. In the GC operating parameters, a sample loop load time of 0.10 minutes was specified. This results in a minimum of 9 seconds in which products were allowed to flow through the sample loop. After the GC sample valve switched into the INJECT position, valve A3 was closed. This GC sampling procedure was completed 3 times for most of the tests.

As for the liquid and gas characterization tests, the test and GC sample naming convention has been standardized. The baseline GC samples have been subtracted from the samples of the accumulator products. Each test recording data from the reactor panel begins with numbers for the date of the test (i.e. 0916 refers to Sept. 16). The letters correspond to the order of the GC samples taken that day. Thus, 0916B-A means the baseline chromatogram 0916A is subtracted from the first sample chromatogram 0916B taken from the accumulator. Typically, three samples were taken from the accumulator for a given test so samples 0916B-A, 0916C-A, and 0916D-A are referred to as a test ID of 0916B:D-A. This naming convention applies to all tests and GC samples.

Because of the run time determined by the oven program and subsequent cool down, samples from the accumulator were taken approximately 45 minutes apart. After all samples had been taken of the accumulator products, the system was flushed with nitrogen and the heaters turned off. The reactor panel typically required a day to cool down before the central reactor tube could be removed. The zeolite catalyst was observed to coke significantly during a single test so that fresh catalyst was installed before each test. Thus, each catalytic cracking test represents two days of system preparation and data acquisition.

A volume of approximately 4.8 ml of JP-10 was injected during each thermal and catalytic test. Approximately 1 gram of zeolite was installed for the catalytic cracking tests. These values were calculated based on experiments by Lopes et al. [17] who used a WHSY (weight of component per hour per unit weight of zeolite) value equal to 6.9 hr^{-1}. The inverse of this value is referred to as the "time on stream". Assuming 1 gram of zeolite is installed in our system, the fuel flowrate of 10.6 g/hr (FP = 125) corresponds

to a time on stream of approximately 330 s and the fuel flowrate of 2.3 g/hr (FP = 25) corresponds to a time on stream of approximately 1570 s. These time on stream values correspond with other documented experiments [35, 21, 10, 36].

Thus, the system parameters tested to determine their effect on the cracking conversion rate and product composition were fuel flowrate (2.3, 6.2, 10.6 g/hr), reactor temperature (250, 300, 350, 425, 500°C), system backpressure (104 and 400 kPa), and zeolite (HY, Beta, USY).

6.2 Mole balance calculations

We present the calculations used to analyze the data obtained during the tests. An example is presented for the purpose of illustration and the use of these calculations as a diagnostic tool is discussed.

In addition to the GC product analysis, a mole balance was completed for each test. The moles of liquid fuel injected were compared to the moles of product created. When JP-10 cracks into lower molecular weight components through the mechanisms of thermal or catalytic cracking, the number of product moles will increase. This can be observed by considering a balanced chemical reaction description of the cracking process. Experiments by Green et al. [6] observed cyclopentadiene C_5H_6 and smaller compounds such as C_3H_4. While the exact cracking products are not known for all conditions, we will assume for the purpose of illustration that the only cracking products are C_5H_5 and C_3H_5 resulting in the following balanced chemical reaction.

$$C_{10}H_{16} \rightarrow 0.2C_5H_5 + 3C_3H_5 \quad \text{or} \quad 3.2C_{3.125}H_5 \tag{13}$$

Thus, 1 mole of JP-10 would yield 3.2 moles of products for this reaction. From the buret liquid level, system pressure, and accumulator position recorded during each test, the injected and product moles are calculated. We refer to these calculations as a mole balance.

As fuel is injected into the system, the buret liquid level changes over time. This change in the liquid level provides a measurement of the amount of liquid fuel ΔV_f injected into the system. Alternatively, the mass M_f and moles n_f of fuel injected can be calculated with the fuel density and molecular weight.

$$M_f = \Delta V_f \cdot \rho_f \tag{14}$$

$$n_f = \frac{M_f}{W_f} \tag{15}$$

The density of JP-10 is 0.94 g/ml and the molecular weight is 136 g/mol. For an assumed liquid fuel flow rate of 10.6 g/hr, a plot of the injected moles over time appears in Fig. 23.

The moles of products in the system can be calculated with the ideal gas law given the instantaneous system pressure and volume. The volume of the accumulator with the piston in the bottom position is calculated to be 1875 cc as discussed previously.

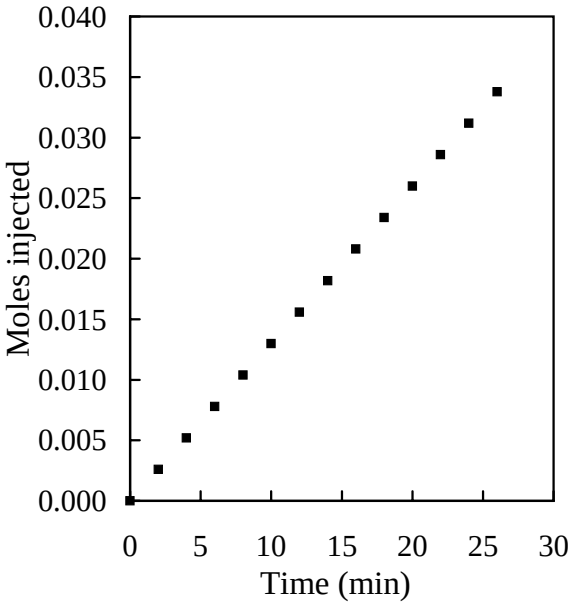

Figure 23: Example: Moles injected into system as a function of time.

The upstream volume of the system V_{sys}^0 was determined to be 260 cc by conducting a pressure-volume balance experiment between the accumulator and system plumbing. Thus, the total system volume as a function of the accumulator piston position is

$$V_{total} = V_{sys}^0 + \left(\frac{\pi}{4}\right) D^2 \cdot H_{piston} \ . \tag{16}$$

The accumulator position is measured as a function of time and a plot of the accumulator position for a product to injected mole ratio of 3.2 and 1 is shown in Fig. 24.

The system temperature T is estimated to be 473 K based on the nominal (Table 2) accumulator temperature used in these tests, the temperature of the other components in the system is kept at comparable values (Table 12). The moles of products (Fig. 25) are then calculated from the accumulator position (Fig. 24) with the ideal gas law and the estimated temperature and measured system pressure.

$$n_p = \frac{P \Delta V_{total}}{\tilde{R} T} \tag{17}$$

Based on the balanced chemical reaction of Eq. 13, 3.2 moles of products are created for every mole of reactant fuel injected into the system. If no decomposition of the fuel occurs in the system, then one mole of reactant will yield one mole of products. Figures 23 and 25 can be combined into a single figure illustrating the mole balance (Fig. 26) by plotting n_p vs n_f. The slope of this line is the mole ratio

$$\frac{n_p}{n_f} = \frac{P \Delta V_{total}}{M_f R_f T} \tag{18}$$

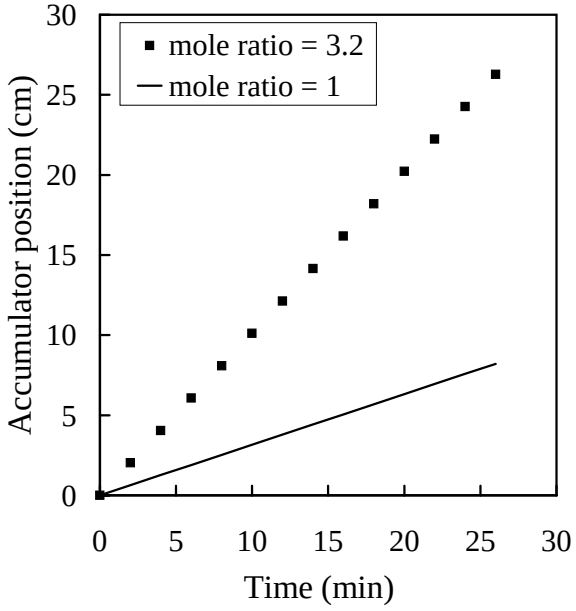

Figure 24: Example: Instantaneous accumulator piston position. Data points are values expected for a 3.2 mole ratio reaction. Line is "zero conversion" expectation.

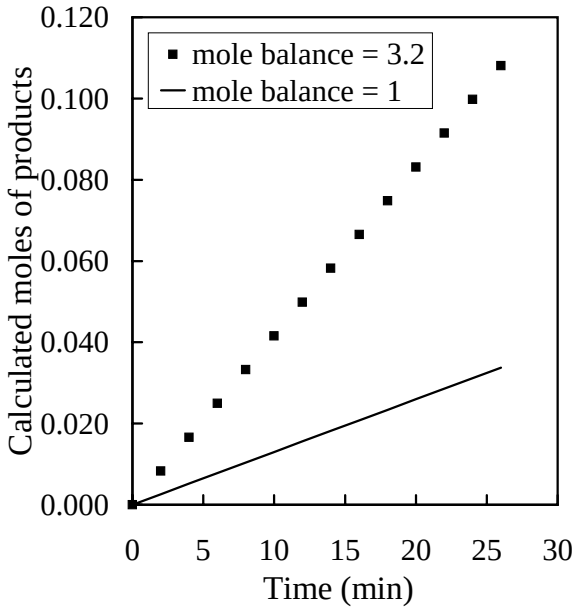

Figure 25: Example: Product moles in system as a function of time.

and is used as a key diagnostic in our tests. The solid line with $n_p/n_f = 1$ refers to the case of "zero conversion" of the fuel into lower molecular weight components. If there is a net mole increase due to reaction, the slope of the line is greater than one, $n_p/n_f > 1$. For a given liquid fuel flow rate, the accumulator volume increases more rapidly with

time for a higher molar conversion ratio.

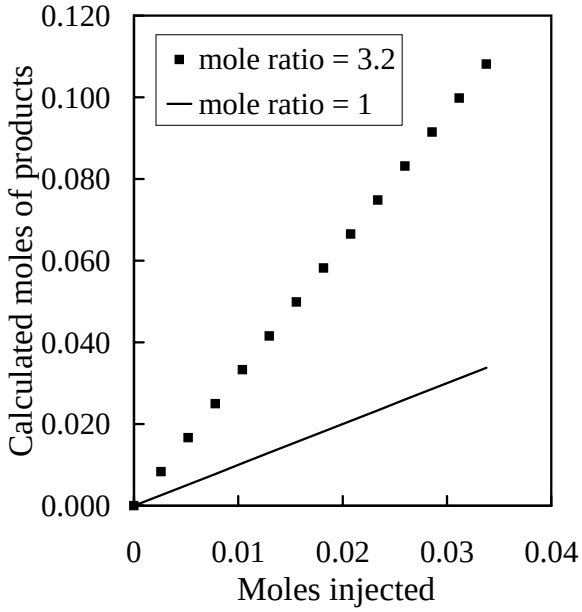

Figure 26: Examples of finding mole ratio n_p/n_f as the slope of the line. Two cases are shown. The solid line is an example of no conversion n_p/n_f =1. The points are for a conversion ratio of $n_p/n_f = 3.2$, corresponding to Equation 13,

6.3 Mass Balance Calculations

In the previous section, the complete conversion of JP10 to products was considered. In reality, the conversion is usually quite incomplete and only a fraction y of the original mass of fuel is converted. The amount of JP10 converted can be measured with the GC by determining the fraction of carbon mass in all the species other than JP-10. Using the notation of Equation 9, the carbon mass fraction of species region i is y_i and the conversion mass fraction is

$$y = \sum_{i \neq \text{JP10}} y_i = \sum_{i \neq \text{JP10}} Area_i \Big/ \sum_{\text{all peaks}} Area_i \tag{19}$$

which is usually expressed at %wt conversion

$$\%\text{wt conversion} = 100 \times y \tag{20}$$

The mass conversion can be related to the mole ratio discussed previously by considering the mass balance for the processes in the reactor. The sequence of events in the reactor can idealized as liquid injection, vaporization, reaction in the catalyst bed, and storage

in the accumulator. The partial reaction of n_f moles of JP-10 vapor can be represented schematically as

$$n_f \mathrm{C_{10}H_{10}} \longrightarrow n_f(1-y)\mathrm{C_{10}H_{10}} + (n_p - n_f(1-y))\,\mathrm{Products} \tag{21}$$

The "Products" of catalytic cracking represent a notional species that has the average molar mass of the actual products and fictitious composition $\mathrm{C}_m\mathrm{H}_n$ appropriate to the mixture. The products have an average molar mass of $\mathcal{W}_P = 12m + n$, where m and n represent an empirical composition appropriate to the mixture and are not necessarily integers. For example, the reaction of equation 13 has a notional product species of $\mathrm{C_{3.125}H_5}$ which has a molar mass of 42.5 g/mol. If all of the product species are correctly accounted for, then the hydrogen-to-carbon ratio m/n must equal 1.6 if we consider that the JP-10 either reacts or remains in the original state. GC measurements indicate that this appears to be the case.

From the reaction equation given above, the mass balance will be

$$M_f = n_f \mathcal{W}_f = n_f(1-y)\mathcal{W}_f + (n_p - n_f(1-y))\,\mathcal{W}_p \tag{22}$$

where $\mathcal{W}_f = 136$ g/mol is the molar mass of JP-10. This can be simplified to

$$\frac{\mathcal{W}_p}{\mathcal{W}_f} = \frac{y}{n_p/n_f - (1-y)} \tag{23}$$

This is the key relationship between mass conversion, mole conversion, and the average product molar mass. Using values of the mass and mole conversion obtained from the experiments, this enables us to predict the average product molar mass. Another way to look at this is as relationship between molar conversion ratio and mass conversion fraction for a fixed average molar mass of the products.

$$\frac{n_p}{n_f} = 1 + \left(\frac{\mathcal{W}_f}{\mathcal{W}_p} - 1\right) y \tag{24}$$

Using this version of the relationship, the expected molar ratio can be predicted as a function of product molar mass and conversion ratio. The limiting cases are: no conversion, $y = 0$ and $n_p/n_f = 1$; complete conversion, $y = 1$ and $n_p/n_f = \mathcal{W}_f/\mathcal{W}_p$. These were illustrated in the previous section.

7 Thermal decomposition

We present all measured data obtained from 16 thermal decomposition tests and 25 corresponding GC samples. The central reactor tube did not contain catalyst and the system was operated at the temperatures listed in Table 3 for heating zones 1, 3, and 4. The reactor in zone 2 was heated to 500°C in all thermal decomposition tests. Several repeat tests were conducted to access the repeatibility in the reactor panel and system diagnostics.

The first series of tests varied the liquid fuel flowrate with experiments at three different fuel pump settings. Tests were run at settings (FP) of 25, 70, and 125. These fuel pump settings correspond to liquid flowrates of 2.3 g/hr, 6.2 g/hr, and 10.6 g/hr respectively (Fig. 8). Graphs of the calculated moles of product versus the injected moles of liquid fuel appear in Fig. 27, 28, and 29. In each graph, the solid line represents the case of zero conversion.

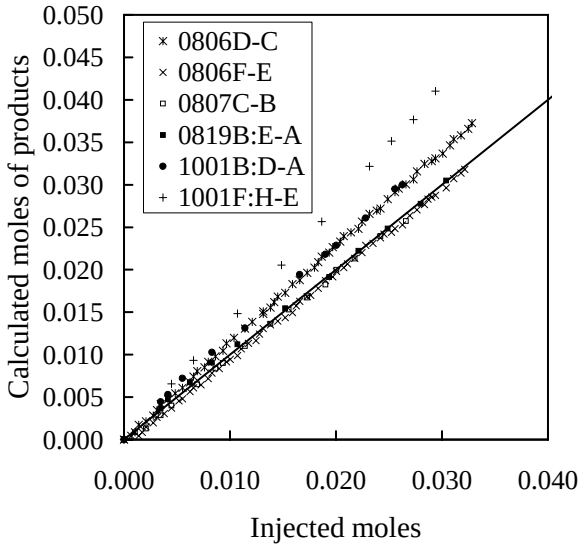

Figure 27: Calculated moles of products versus injected moles for thermal decomposition tests with a liquid fuel flow rate of 2.3 g/hr (FP = 25).

The results at the highest metering speed are the most consistent and repeatable over time. The results at each flowrate were averaged enabling a comparison shown in Fig. 30. The slope of these mole balances correspond to the number of moles of products divided by the number of moles injected into the system (Fig. 31). There is substantial scatter in this plot for the lowest flow rate (2.3 g/hr), mole ratios varied between 0.975 and 1.389. The scatter decreases for the intermediate flow rate (6.2 g/hr) and is minimal for the highest flowrate (10.6 g/hr). The reasons for the scatter at low flow rates is not obvious but the condition of the stainless steel tubing and fittings used for the reactor channel and plumbing are the obvious factors. It is known that stainless steel can exhibit catalytic activity and the effectiveness of this action will be depend strongly on the surface condition of the steel. No attempt was made to control the surface condition in

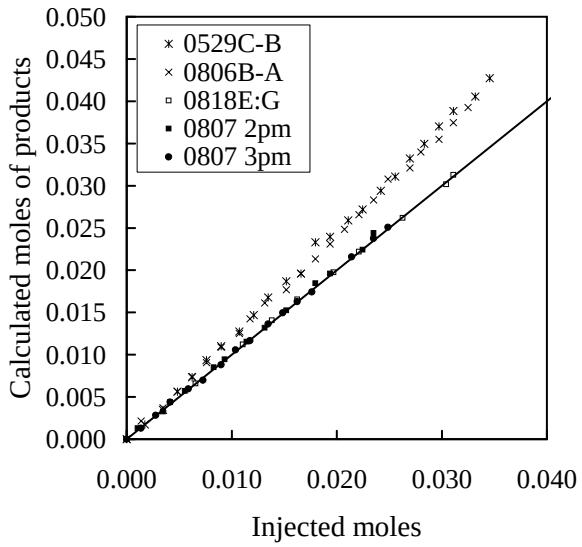

Figure 28: Calculated moles of products versus injected moles for thermal decomposition tests with a liquid fuel flowrate of 6.2 g/hr (FP = 70).

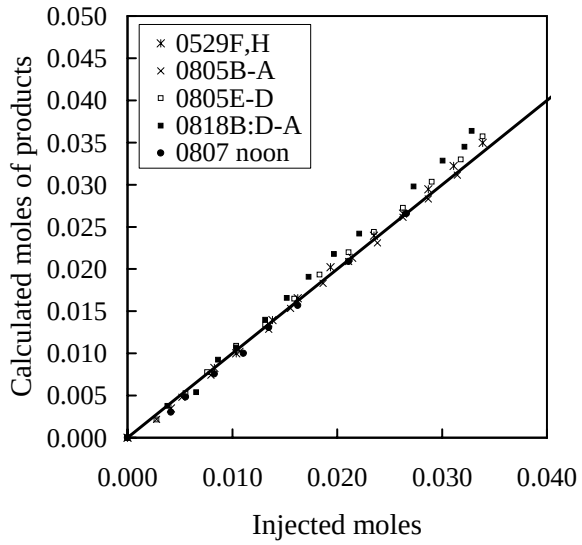

Figure 29: Calculated moles of products versus injected moles for thermal decomposition tests with a liquid fuel flowrate of 10.6 g/hr (FP = 125).

the present tests because that would have been very difficult to do in any case. The reactor plumbing was also very difficult to clean out since the fittings contained many cervices that can trap fuel or decomposition products. Finally, in some tests, the total motion of the tell-tale on the accumulator was extremely small and the measurement of the final product volume was subject to significant uncertainty. If an accurate measurement of thermal decomposition is needed, we recommend that the tests be repeated using quartz tubing for the high temperature parts of the reactor and a carefully prepared stainless

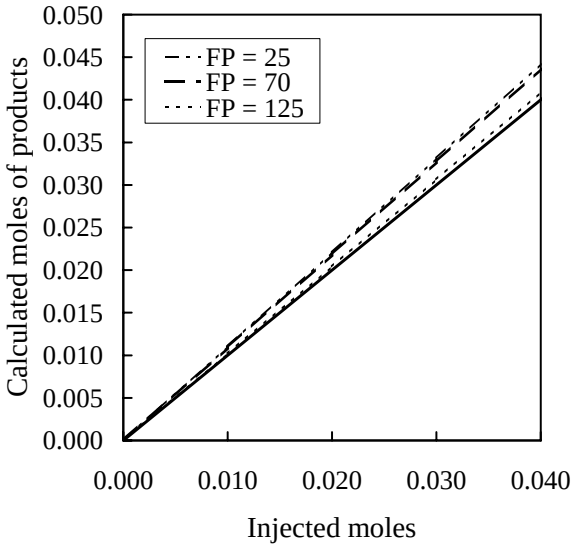

Figure 30: Calculated moles of products versus injected moles averaged over all thermal decomposition tests for the different liquid fuel flowrates.

steel sample.

Despite the variability, the cases at the two higher flow rates yielded average molar conversion ratios between 0.95 and 1.05 and mass conversion amounts of less than 3% (Table 15). Reducing the liquid fuel flowrate from 10.6 g/hr to 2.3 g/hr results in increasing the average mass conversion up to 6% in the most extreme case (Table 14). The variability in the mass conversion ratios is probably associated with the difficulty in flushing the JP-10 from the system between runs, condensation of JP-10 in cold spots, and the saturation of the column and detector due to the very high concentration of JP-10.

As described in the test procedures section, the chromatograms were split into regions corresponding to compounds with the same number of carbon atoms. The area under the detector signal in each region is summed and divided by the total area under the signal in all the regions. A representative GC sample of a thermal decomposition test appears in Fig. 32 and is very similar to the chromatogram of liquid JP-10 (Fig. 18).

For most tests, multiple GC samples were taken from the accumulator. The product composition for multiple GC samples taken during individual tests as a function of the liquid fuel flowrate appears in Fig. 33, 34, 35, 36, and 37. In the plots, the JP-10 (C_{10}) composition was not plotted for clarity. Table 15 contains the percent conversions calculated for each GC sample and the average percent conversion of each test with the reactor panel. The mole ratio is plotted as a function of the mass conversion fraction in Fig. 42. Clearly, the conversion amounts and the molar ratios have too much variability to be draw any conclusions about an average molar mass of the products.

The product composition of all tests at the same liquid fuel flowrate appears in Fig. 38, 39, and 40. Tests in which multiple GC samples were taken were averaged. Finally, the product compositions were averaged enabling a direct comparison of the effect of fuel

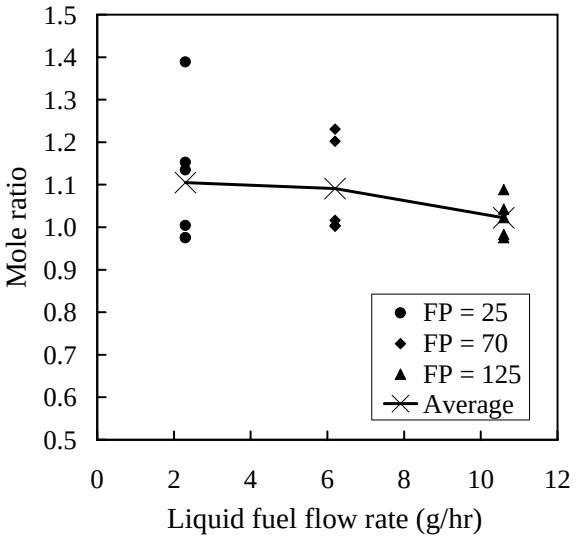

Figure 31: Ratio of product moles to injected moles for each thermal decomposition test at the different liquid fuel flowrates. Straight line represents the average mole ratio.

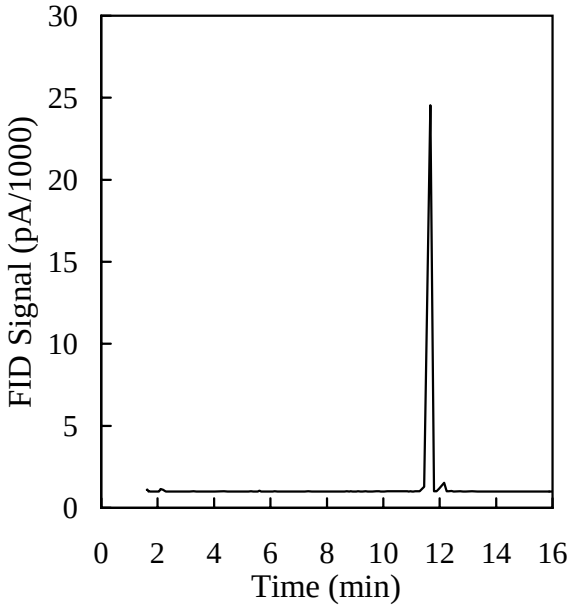

Figure 32: GC chromatogram (Test 0807C-B) representative of thermal decomposition test.

flowrate (Fig. 41). The percent of products increases as the flowrate decreases. This is expected due to the increasing total conversion rate (Table 14).

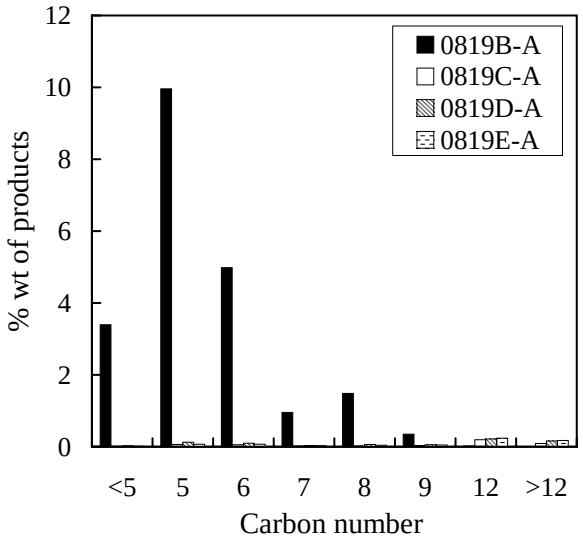

Figure 33: Product composition of test 0819B:E-A at a fuel flowrate of 2.3 g/hr (FP = 25). C_{10} products are omitted for clarity.

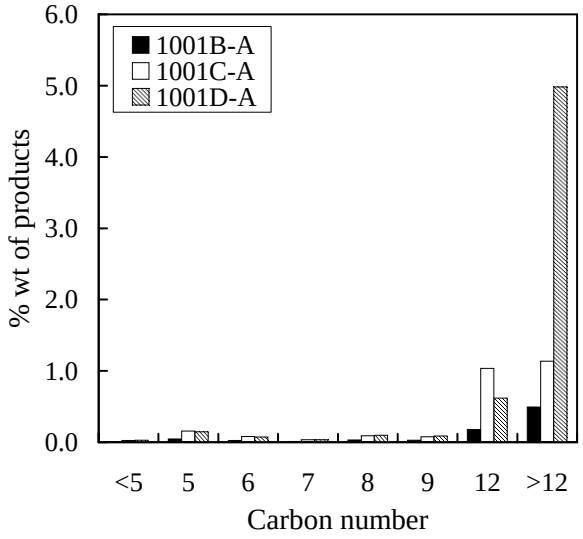

Figure 34: Product composition of test 1001B:D-A at a fuel flowrate of 2.3 g/hr (FP = 25). C_{10} products are omitted for clarity.

	Avg. % Conversion
25	3.15
70	2.19
125	1.90

Table 14: Overall average percent conversion of all thermal decomposition tests for the different liquid fuel flowrates.

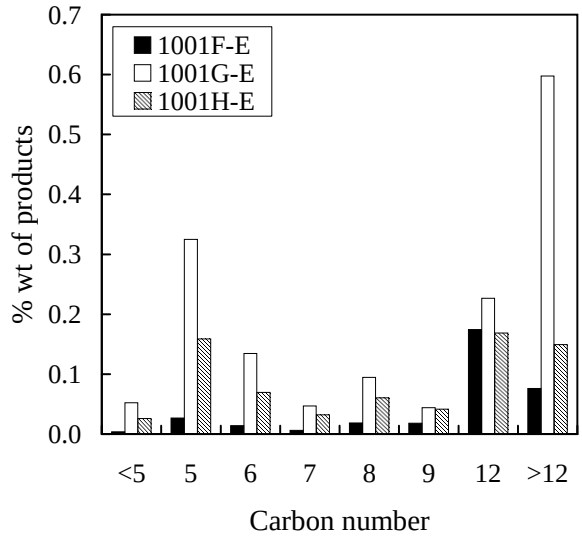

Figure 35: Product composition of test 1001F:H-E at a fuel flowrate of 2.3 g/hr (FP = 25). C_{10} products are omitted for clarity.

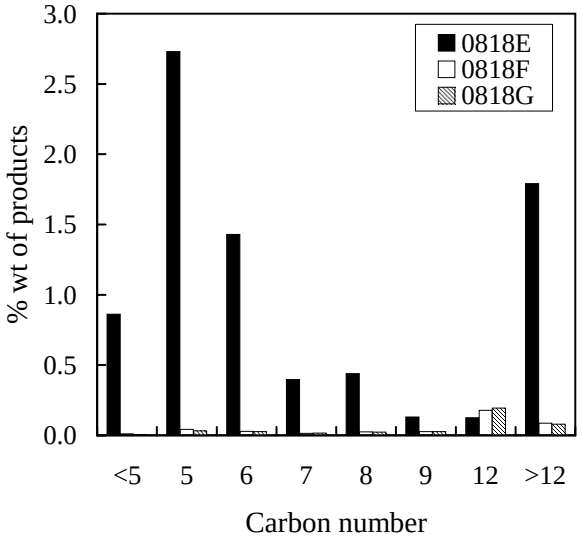

Figure 36: Product composition of test 0818E:G at a fuel flowrate of 6.2 g/hr (FP = 70). C_{10} products are omitted for clarity.

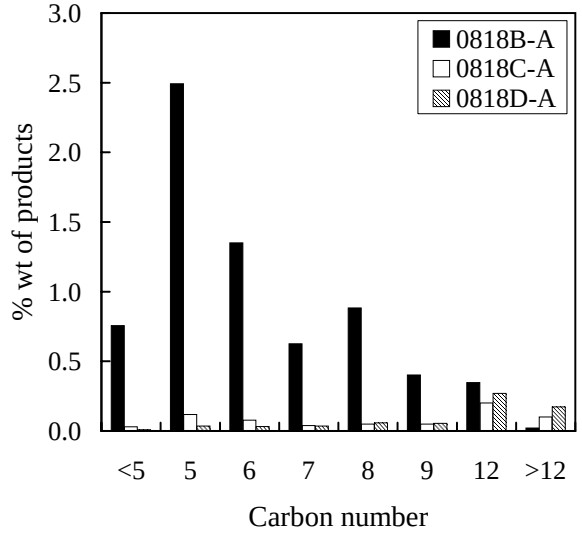

Figure 37: Product composition of test 0818B:D-A at a fuel flowrate of 10.6 g/hr (FP = 125). C_{10} products are omitted for clarity.

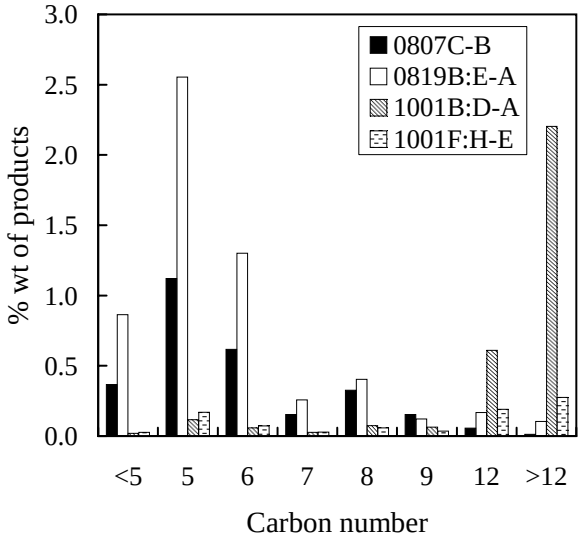

Figure 38: Average product composition for thermal decomposition tests at a liquid fuel flowrate of 2.3 g/hr (FP = 25). C_{10} products are omitted for clarity.

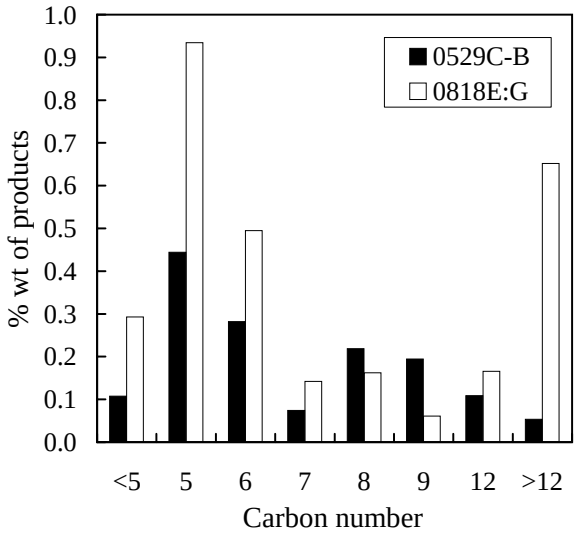

Figure 39: Average product composition for thermal decomposition tests at a liquid fuel flowrate of 6.2 g/hr (FP = 70). C_{10} products are omitted for clarity.

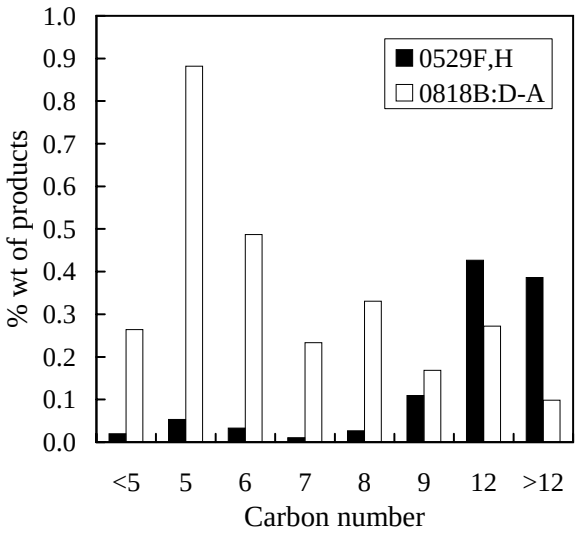

Figure 40: Average product composition for thermal decomposition tests at a liquid fuel flowrate of 10.6 g/hr (FP = 125). C_{10} products are omitted for clarity.

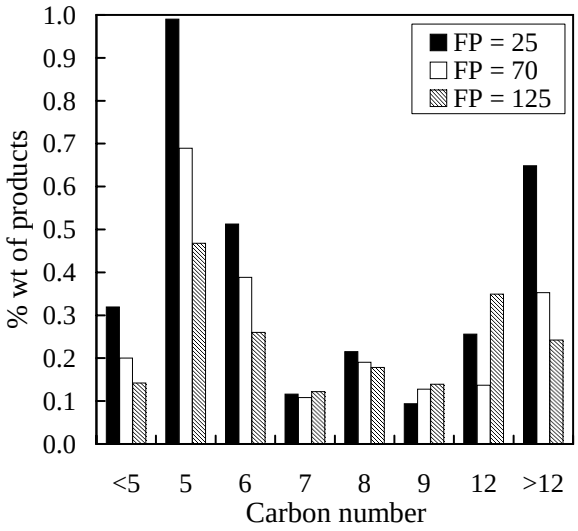

Figure 41: Overall product composition for thermal decomposition tests averaged over individual tests and multiple GC samples. C_{10} products are omitted for clarity.

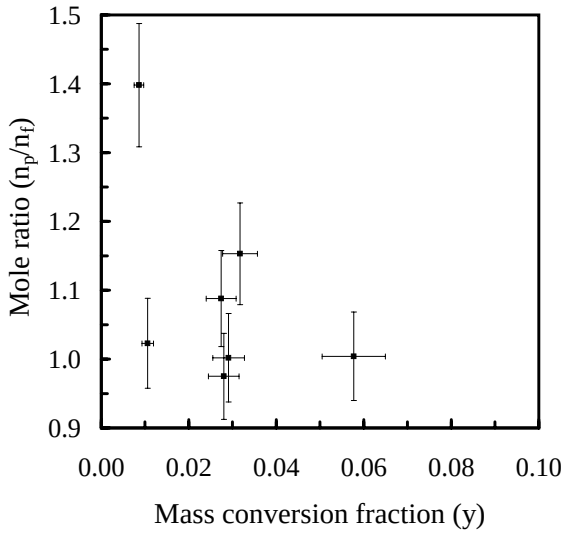

Figure 42: Observed mole ratio n_p/n_f as a function of the mass conversion fraction y for the thermal decomposition tests.

Test ID	Sample ID	Fuel Pump Setting	Metering Rate	n_p/n_f	Average % wt. Conv.	% wt. Conv.
0529C-B	0529C-B	70	6.2	1.231	1.48	1.48
0529F,H	0529F-E 0529H-G	125	10.6	1.023	1.06	1.59 0.54
0805B-A	0805B-A	125	10.6	0.983	-	-
0805E-D	0805E-D	125	10.6	1.042	-	-
0806B-A	0806B-A	70	6.2	1.202	-	-
0806D-C	0806D-C	25	2.3	1.135	-	-
0806F-E	0806F-E	25	2.3	0.976	-	-
0807 Noon	-	125	10.6	0.975	-	-
0807 2pm	-	70	6.2	1.017	-	-
0807 3pm	-	70	6.2	1.004	-	-
0807C-B	0807C-B	25	2.3	0.975	2.80	2.80
0818B:D-A	0818B-A 0818C-A 0818D-A	125	10.6	1.088	2.74	6.88 0.66 0.67
0818E:G	0818E 0818F 0818G	70	6.2	1.002	2.91	7.90 0.41 0.40
0819B:E-A	0819B-A 0819C-A 0819D-A 0819E-A	25	2.3	1.004	5.77	21.15 0.49 0.78 0.70
1001B:D-A	1001B-A 1001C-A 1001D-A	25	2.3	1.153	3.17	0.82 2.63 6.06
1001F:H-E	1001F-E 1001G-E 1001H-E	25	2.3	1.389	0.86	0.34 1.52 0.71

Table 15: Summary of all thermal decomposition tests and corresponding GC samples. The reactor temperature in zone 2 was 500°C. Estimated uncertainty in n_p/n_f is ±6.4% and uncertainty in Avg % wt. Conversion y is 12.5%.

8 Catalytic cracking

8.1 Zeolite preparation

The zeolite Y powder with a Si/Al ratio (SAR) of 6.0 was obtained in sodium form. It was protonated by ion exchange with aluminum nitrate. A 1 M solution of ammonium nitrate was made by mixing 80 g of solid NH_4NO_3 with 1 L of distilled water. The solution was stirred until it was completely mixed. The zeolite powder was then mixed at a ratio of 1 g of zeolite for every 100 ml of solution and allowed to stir for at least 12 hours. The zeolite was then filtered from the solution using a flask with a faucet aspirator. A new solution of ammonium nitrate was made and the zeolite returned to the flask for another 12 hours of mixing. This process was repeated 4 times.

After filtering the zeolite powder from the solution for the final time, the zeolite was placed in a ceramic crucible and calcined in a temperature controlled oven. The oven facility contained gas inlets which were connected to metered dry air and nitrogen for control of the internal oven environment. For the calcination procedure, the zeolite in the crucible was placed in the oven and dry nitrogen was allowed to flow through the oven. The oven temperature was increased at a rate of 5°C/min from 30 to 250°C. It was held at 250°C for 4 hrs and then increased at the same rate to a temperature of 500°C. It was held at this temperature for approximately 6 hrs.

The zeolite powder is formed into pellets by first compressing the powder into small disks. Two meshes (#60 and #45) were used with a pestle to break the disks into pellets. The pellets on the #60 mesh were saved for installation into the reactor.

After each test, the zeolite was found to be coked and no longer effective in causing cracking reactions with the hydrocarbon sample. Regeneration of the zeolite could restore the activity of the pellets. This was conducted by placing the coked zeolite into a crucible and placing it into the oven. The dry nitrogen was allowed to flow through the oven while the temperature was increased from 30 to 200°C at a rate of 1°C/min. It was held at 200°C for 3 hrs. Then the nitrogen supply was turned off and the air supply turned on. The temperature was increased again at the same rate to 550°C then allowed to cool to room temperature in the air environment.

8.2 Test results

8.2.1 Effect of zeolite activity

For a zeolite to act as a catalyst in the HC reactions, it must have active sites. These are the sites generated in the ion exchange and calcination procedures forming a Bronsted acid base. When a zeolite becomes coked, the active sites become clogged with carbon deposits preventing the sites from participating in reactions with the surrounding hydrocarbon. During tests with the different zeolites, it was determined that the catalyst became coked after a single test at the nominal test conditions of approximately 4.8 ml of JP-10 injected and a reactor temperature of 500°C. This is observed by comparing the conversion of two subsequent runs without zeolite replacement in between. The mole

balance for the first run with zeolite pellets containing active sites (test 0524D,G,I) and the mole balance for the second run where the zeolite active sites have become blocked appear in Fig. 43. The ratio of product moles to injected moles for the active zeolite is

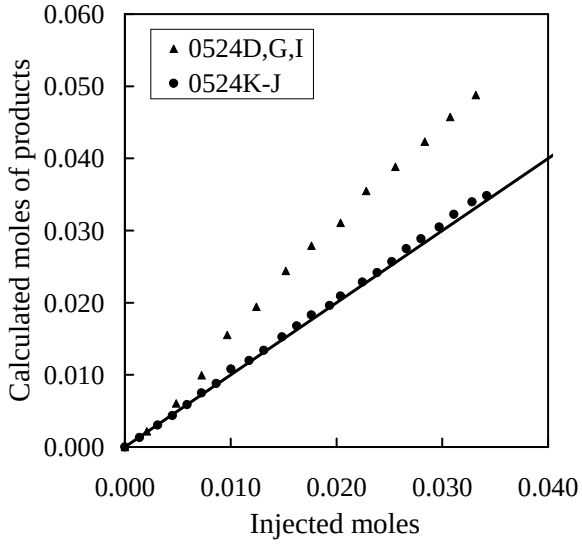

Figure 43: Comparison of moles of product to moles of injected JP-10 with HY zeolite with active sites and coked HY zeolite. Fuel flowrate is 10.6 g/hr (FP = 125). Reactor temperature in zone 2 was 500°C.

1.510 whereas the ratio for the coked zeolite is 1.026. This value compares to the thermal cracking runs which had an average mole ratio of 1.022 at a fuel flowrate of 10.6 g/hr (FP = 125) illustrating that a coked zeolite does not contribute to catalytic cracking of the sample hydrocarbon.

As mentioned above, the active sites of a zeolite may be regenerated by burning off the coke deposits in an air environment at elevated temperatures. Throughout the course of testing with the reactor panel, the first batch of zeolite pellets was regenerated in addition to making a second batch of HY zeolite pellets. To verify conversion rates and zeolite reactivity between the different batches of zeolite pellets, repeat tests were conducted. The mole balance results comparing the first and second zeolite batches at a fuel flowrate of 2.3 g/hr (FP = 25) appear in Fig. 44. The reactivity of the two batches appear similar except for test 0815B:E-A. The percent conversion of this test is an average of 55% greater than the other tests and may be due to installation of a new stainless steel central reactor tube instigating additional surface reactions increasing the conversion rate. At the time of these initial tests, the effect of stainless steel surface reactivity was not known nor accounted for.

The mole balance comparison between the first zeolite batch and the regenerated first batch appear in Fig. 45 at a fuel flowrate of 10.6 g/hr (FP = 125). The results are similar and the ratio of product moles to injected moles is an average of 1.472 and 1.583 for the original and regenerated batches, respectively.

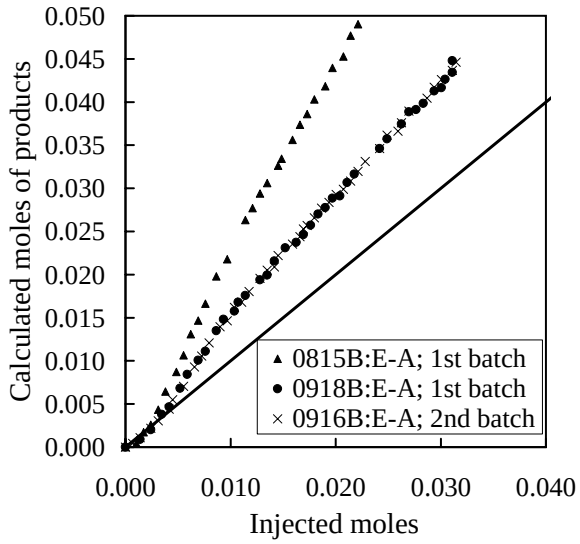

Figure 44: Comparison of moles of product to moles of injected JP-10 from tests with the first and second batches of HY zeolite. Fuel flowrate is 2.3 g/hr (FP = 25). Reactor temperature in zone 2 was 500°C.

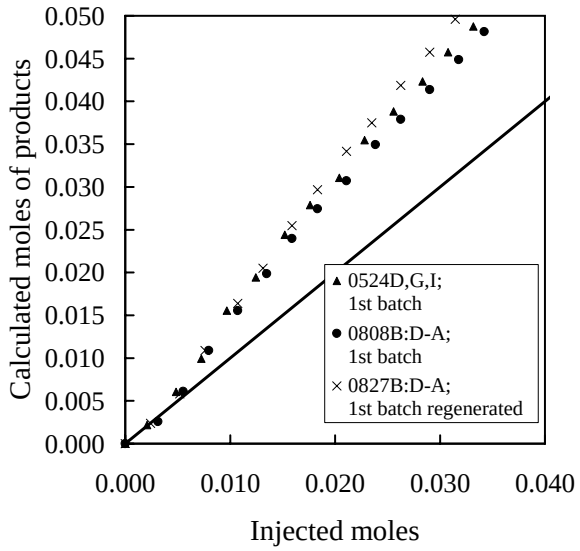

Figure 45: Comparison of moles of product to moles of injected JP-10 from tests with the first batch and regenerated first batch of HY zeolite. Fuel flowrate is 10.6 g/hr (FP = 125). Reactor temperature in zone 2 was 500°C.

As was done in the thermal cracking results, multiple GC samples were generally taken from the products for a given test. The product compositions resulting from multiple GC samples of the different zeolites discussed above appear in Fig. 46, 47, 48, 49, 50, 51, and 52.

The multiple GC samples from each test were averaged and then subsequently aver-

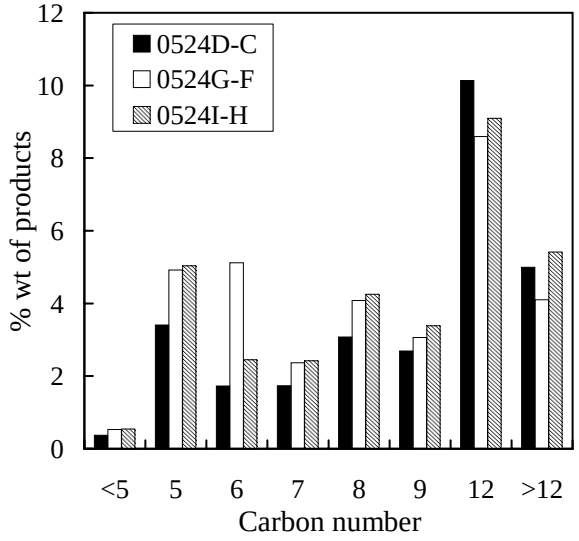

Figure 46: Product composition of test 0524D,G,I with the first batch of HY zeolite at a fuel flowrate of 10.6 g/hr (FP = 125). The C_{10} products are omitted for clarity.

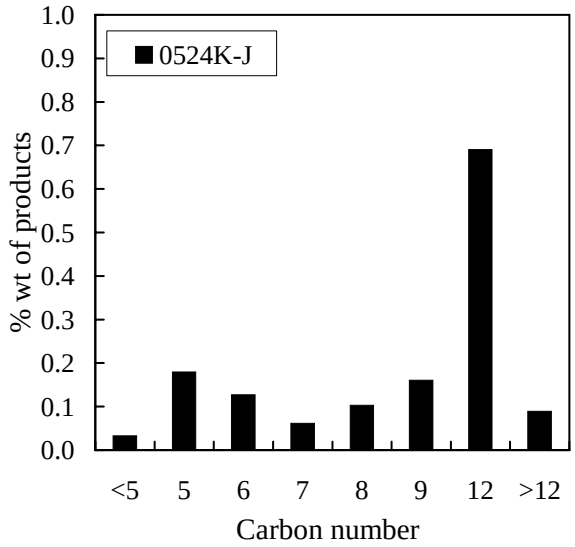

Figure 47: Product composition of test 0524K-J with the first batch of HY zeolite that was coked at a fuel flowrate of 6.2 g/hr (FP = 70). The C_{10} products are omitted for clarity.

aged across similar zeolite batches to generate the comparisons of Fig. 53 and 54. The activity between the first and second batches of HY zeolite is similar. The average percent conversion at a fuel flowrate of 2.3 g/hr for the first batch is 33.62% while the percent conversion for the second batch is 35.52%. Activity between the first batch and the regenerated first batch is not as similar. The average percent conversion at a fuel flowrate of 10.6 g/hr for the first batch is 31.45% while the conversion for the regenerated zeolite

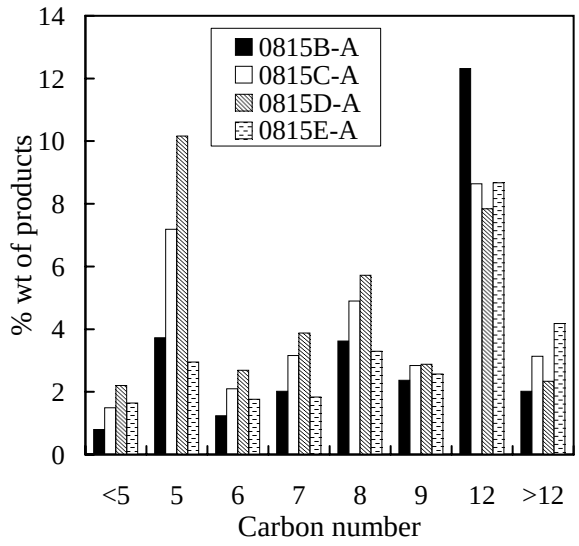

Figure 48: Product composition of test 0815B:E-A with the first batch of HY zeolite at a fuel flowrate of 2.3 g/hr (FP = 25). The C_{10} products are omitted for clarity.

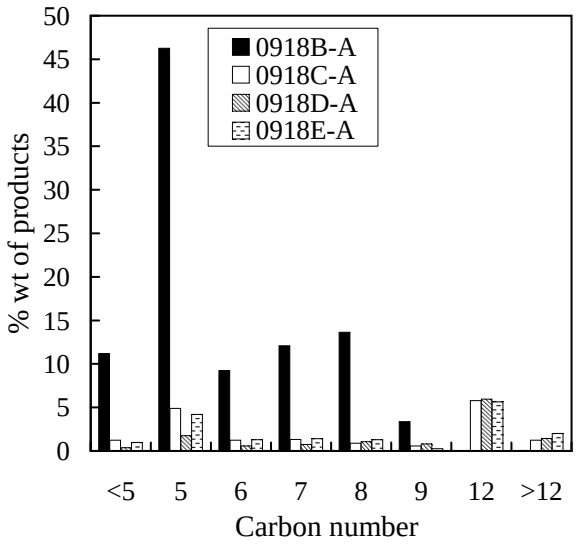

Figure 49: Product composition of test 0918B:E-A with the first batch of HY zeolite at a fuel flowrate of 2.3 g/hr (FP = 25). The C_{10} products are omitted for clarity.

is 61.41%. It is not understood why such a high conversion is observed in the regenerated HY zeolite, especially since the mole balance results are very similar to the results of the first batch (Fig. 45). An error in the product composition analysis seems a likely cause of this discrepancy.

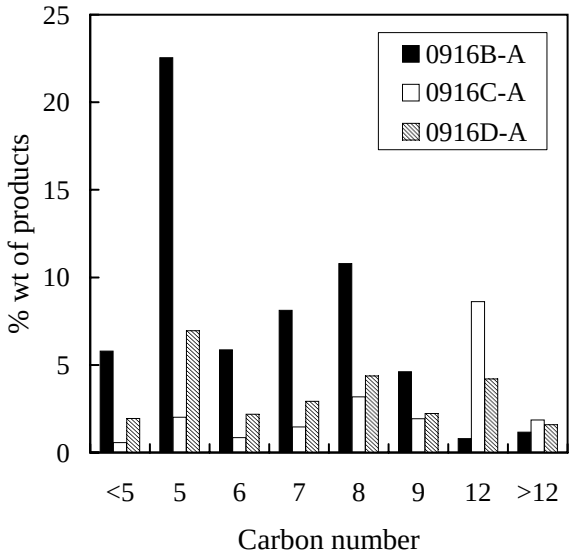

Figure 50: Product composition of test 0916B:E-A with the second batch of HY zeolite at a fuel flowrate of 2.3 g/hr (FP = 25). The C_{10} products are omitted for clarity.

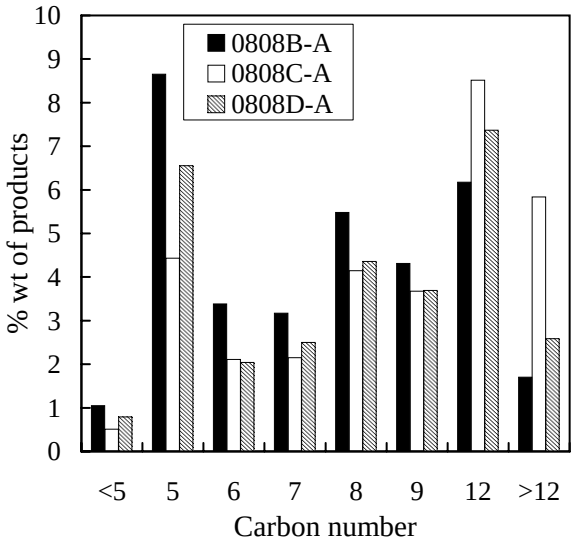

Figure 51: Product composition of test 0808B:D-A with the first batch of HY zeolite at a fuel flowrate of 10.6 g/hr (FP = 125). The C_{10} products are omitted for clarity.

8.2.2 Effect of liquid fuel flowrate

To compare the effect of liquid fuel flowrate on conversion, the tests with HY zeolite at a reactor temperature of 500°C presented above were averaged. By averaging the three tests of Fig. 44 at FP = 25 and the three tests of Fig. 45 at FP = 125, we obtain the overall averaged mole balances of Fig. 55. The overall average ratio of product moles to injected moles is 1.701 and 1.509 for FP = 25 and 125, respectively (Fig. 56). The moles

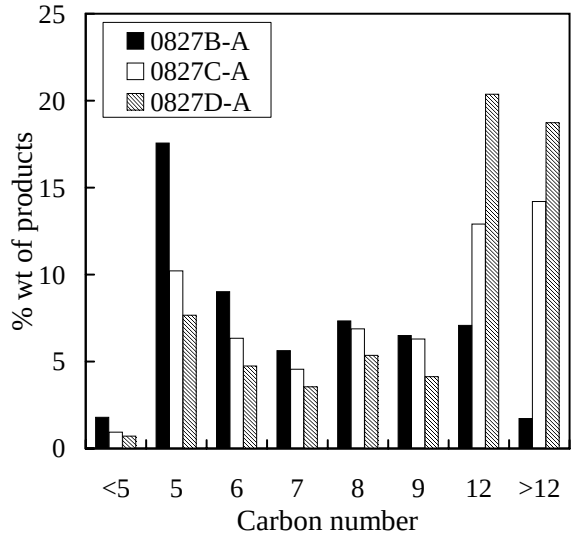

Figure 52: Product composition of test 0827B:D-A with the regenerated first batch of HY zeolite at a fuel flowrate of 10.6 g/hr (FP = 125). The C_{10} products are omitted for clarity.

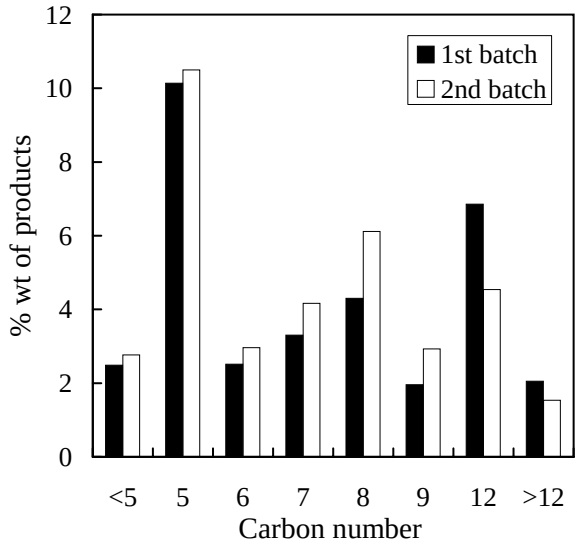

Figure 53: Comparison of product compositions between the first and second batches of HY zeolite. Compositions are averaged over multiple samples per test and multiple tests. Fuel flowrate is 2.3 g/hr (FP = 25). The C_{10} products are omitted for clarity.

of products increase 11.3% as the fuel flow rate decreases from 10.6 to 2.3 g/hr.

Because these data were obtained at a reactor temperature of 500°C, thermal cracking reactions are expected as shown in the previous section. These thermal reactions result in a small conversion (Table 14). Thus, we correct the catalytic cracking data by subtracting the product moles created due to the thermal cracking reactions (Fig. 57). However,

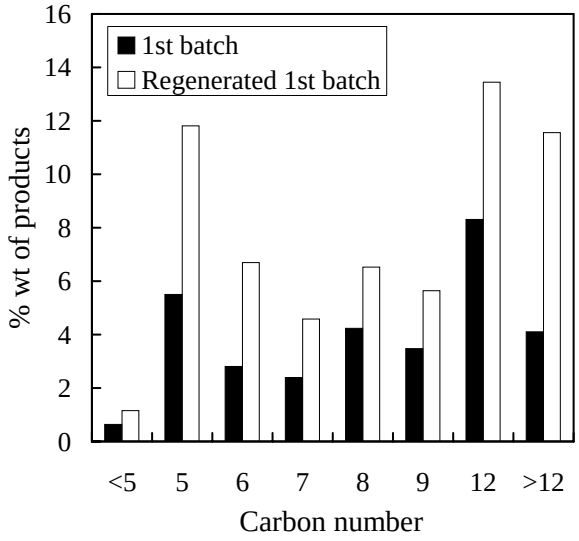

Figure 54: Comparison of product compositions between the first batch and regenerated first batch of HY zeolite. Compositions are averaged over multiple samples per test and multiple tests. Fuel flowrate is 10.6 g/hr (FP = 125). The C_{10} products are omitted for clarity.

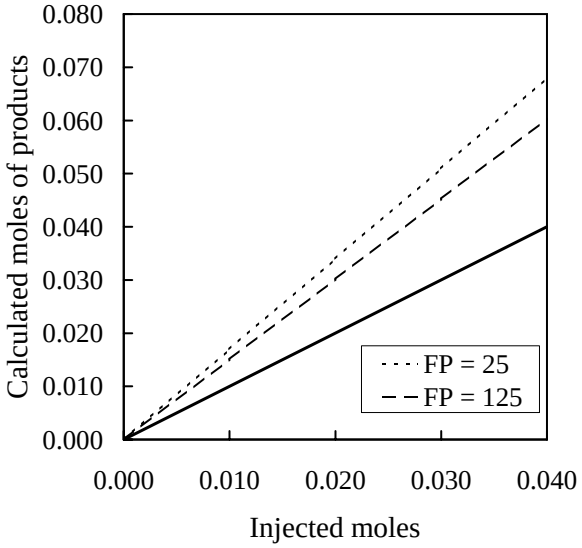

Figure 55: Average mole balances of all HY zeolite batches at a reactor temperature of 500°C for fuel flowrates of 2.3 and 10.6 g/hr (FP = 25 and 125 respectively).

because of the small amount of conversion due to cracking reactions, we do not correct the remaining data.

The average product composition considering multiple GC samples for the above tests with HY zeolite at a reactor temperature of 500°C appears in Fig. 58. The variation in products is slight with the lower fuel flowrate increasing the percent weight of the C_5

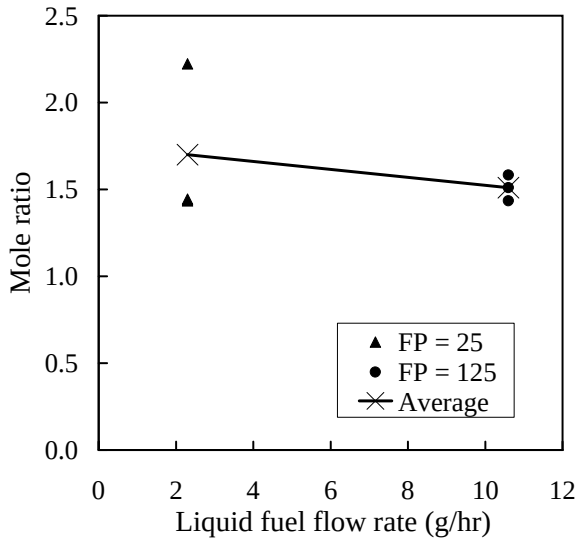

Figure 56: Ratio of product moles to injected moles for tests with HY zeolite. The average ratio is denoted by a straight line. This data is not corrected for thermal cracking.

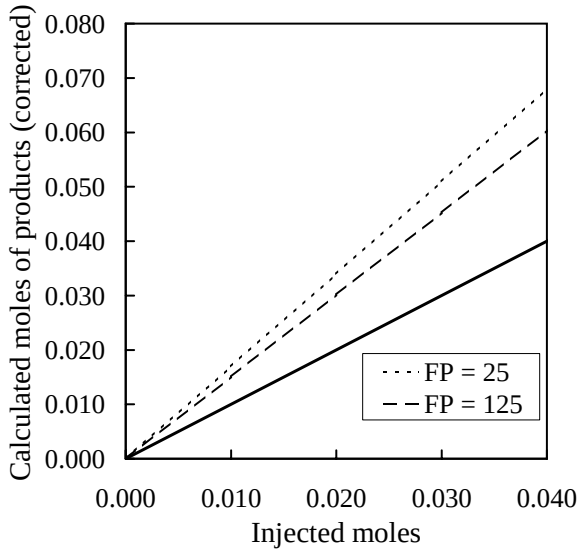

Figure 57: Ratio of product moles to injected moles corrected for conversion due to thermal cracking for tests with HY zeolite.

components approximately 2% and decreasing the coking products (>C10) by a total of 9%. These large carbon number compounds are indicative of coke and coke precursors. The formation of these deposits is known to be accelerated at higher flowrates which correspond to higher Reynolds numbers [24, 21]. From Table 17, the overall average conversion of HY zeolite at a fuel flowrate of 2.3 g/hr (FP = 25) is 34% while the overall average conversion at a fuel flowrate of 10.6 g/hr (FP = 125) is 41%.

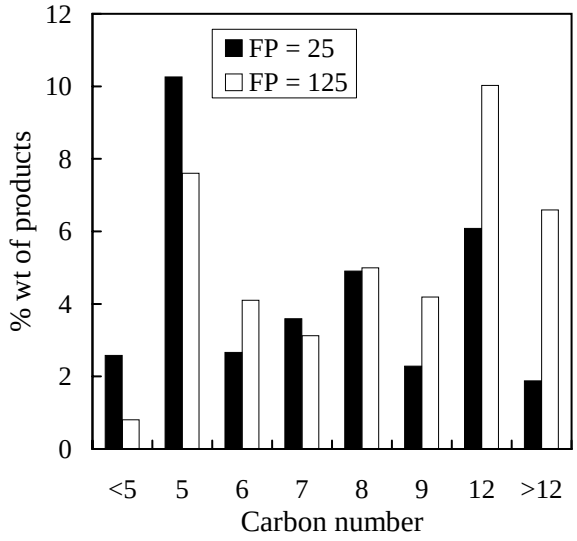

Figure 58: Averaged product composition as a function of liquid fuel flowrate for HY zeolite. The C_{10} products are omitted for clarity.

8.2.3 Effect of zeolite type

Zeolites Beta and ultrastable-Y (USY) were also tested at the nominal reactor conditions of 500°C and a fuel flowrate of 2.3 g/hr (FP = 25). A single test was conducted with each zeolite and the mole balance results are compared with the overall average HY data at the same fuel flowrate (Fig. 59). The USY had a much lower activity observed by a

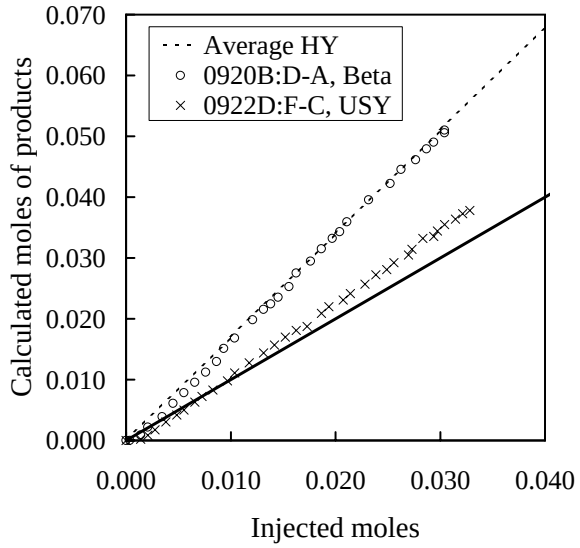

Figure 59: Ratio of product moles to injected moles for tests with different zeolites.

mole ratio of 1.137. The Beta and HY zeolites had similar activities as observed by mole ratios of 1.667 and 1.701, respectively. It should be noted that the pore diameters of HY

and Beta (Table 1) are similar so their similar activity with JP-10 is expected.

The product distribution over multiple GC samples appears in Fig. 60 for USY and Fig. 61 for Beta. Significant variation in the GC samples is again observed. However, Beta does have a greater percentage of C_5 components whereas USY has a greater percentage of C_6 compounds. Since USY cracks the JP-10 into larger compounds as compared with HY and Beta, the decreased conversion observed in Fig. 59 is expected. The multiple GC samples for each test are averaged and compared to the average product distribution of HY (Fig. 62). From Table 17, we calculate an overall average conversion of 70% for Beta and 11% for USY. These are compared with the overall average conversion of HY at the same fuel flowrate of 34%

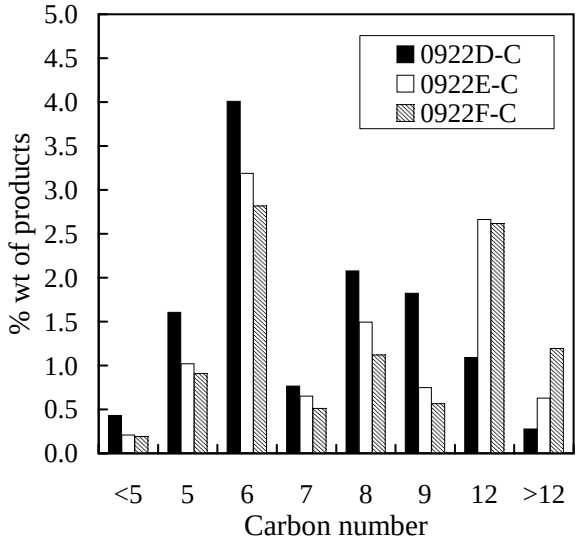

Figure 60: Product composition of test 0922D:F-C with USY zeolite at a fuel flowrate of 2.3 g/hr (FP = 25). The C_{10} products are omitted for clarity.

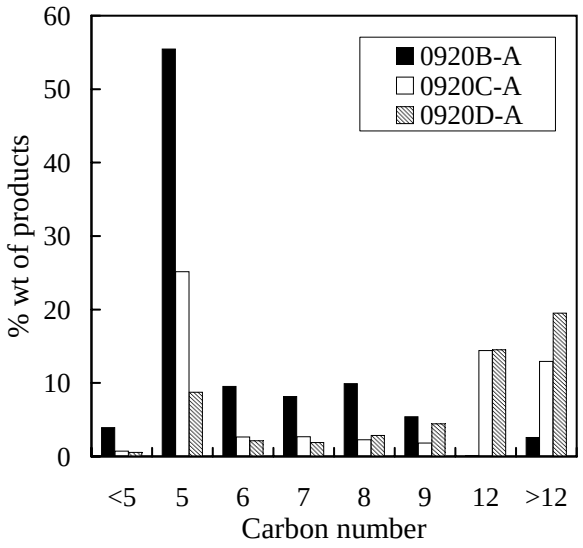

Figure 61: Product composition of test 0920B:D-A with Beta zeolite at a fuel flowrate of 2.3 g/hr (FP = 25). The C_{10} products are omitted for clarity.

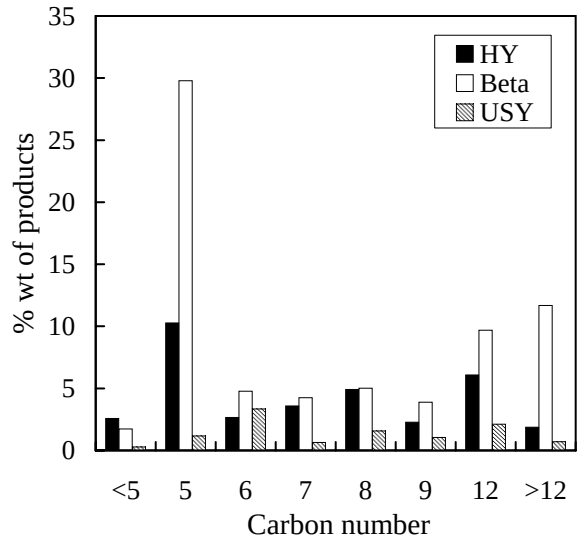

Figure 62: Average product composition comparing different zeolites at a fuel flowrate of 2.3 g/hr (FP = 25). The C_{10} products omitted for clarity.

8.2.4 Comparison of catalytic and thermal cracking

The average mole balances for the thermal tests previously discussed and the HY catalytic cracking tests appear in Fig. 63 for a fuel flowrate of 2.3 g/hr (FP = 25) and Fig. 64 for a fuel flowrate of 10.6 g/hr (FP = 125). The mole balance increases from 1.11 to 1.70 at a flow rate of 2.3 g/hr and it increases from 1.02 to 1.51 at a flowrate of 10.6 g/hr when the catalyst is installed in the reactor. The overall average product compositions appear in Fig. 65 for FP = 25 and Fig. 66 for FP = 125. The catalytic tests increase the conversion of JP-10 as expected by observing the increased composition of the smaller carbon components, particularly the C_5 components.

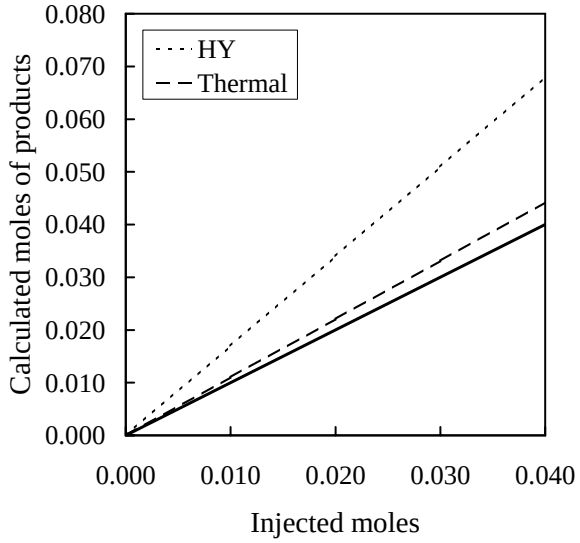

Figure 63: Average ratio of product moles to the injected moles for the thermal cracking and catalytic cracking tests at a fuel flowrate of 2.3 g/hr (FP = 25).

8.2.5 Effect of pressure

The effect of system pressure was studied in test 0913B:D-A. The system was pressurized to 400 kPa of nitrogen before the FIV was opened or the fuel pump turned on. The bottom of the accumulator was also pressurized to 400 kPa with air. Due to the increased pressure, the piston in the accumulator did not move much and the uncertainty in the gauge reading increased as compared with the baseline tests. This is observed through a slight increase in the data point scatter of the mole balance results (Fig. 67). The data are plotted with the overall average HY mole balance of Fig. 55. The ratio of product moles to injected moles at the higher system pressure is 0.996 which is similar to the average thermal mole ratio of 1.10.

A look at the product distribution from multiple GC samples in Fig. 68 yields a significant fraction of products with carbon numbers greater than 10. Thus, the higher pressure inhibits the cracking reactions to smaller carbon numbers and enhances coking.

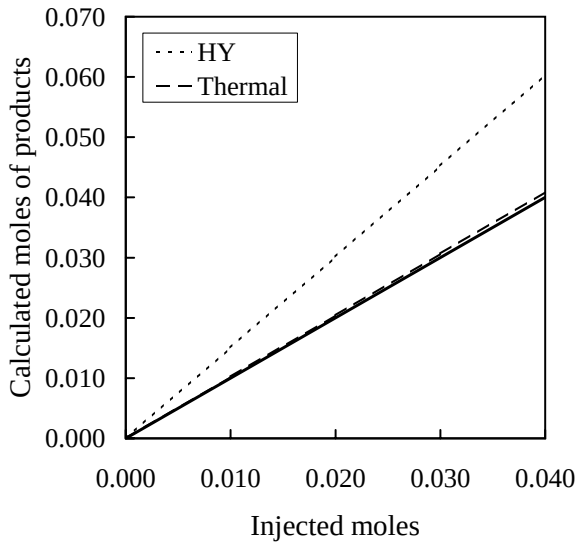

Figure 64: Average ratio of product moles to the injected moles for the thermal cracking and catalytic cracking tests at a fuel flowrate of 10.6 g/hr (FP = 125).

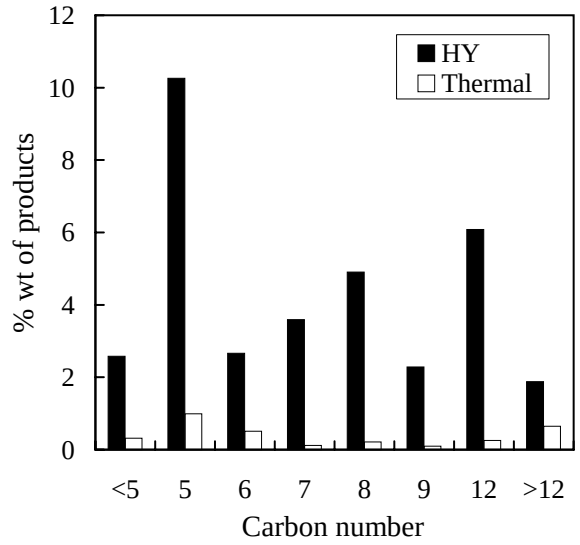

Figure 65: Overall average product distributions for tests with and without catalyst installed in the reactor at a fuel flowrate of 2.3 g/hr (FP = 25). The C_{10} products are omitted for clarity.

This is expected because the higher pressure acts to increase the Reynolds number which increases deposit formation [24, 21]. Additionally, by Le Chatlier's principle, an increase in the pressure would cause the chemical reactions to proceed in a manner decreasing the number of moles in the system. Thus, higher molecular weight species would be formed. This supports the GC product distribution measured. Averaging over the multiple GC samples enables a comparison of the product distribution with the baseline HY case

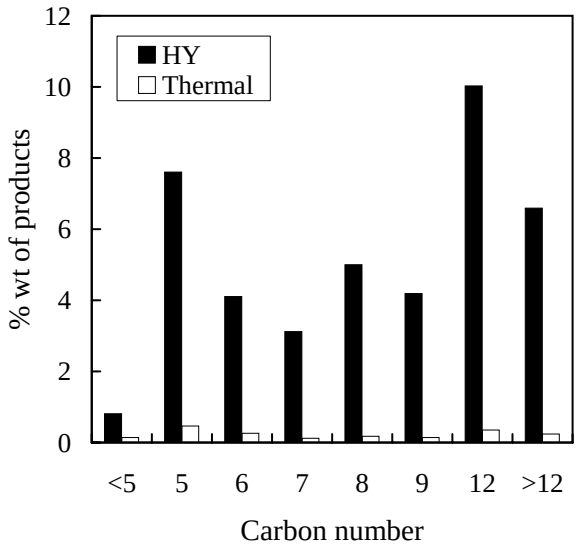

Figure 66: Overall average product distributions for tests with and without catalyst installed in the reactor at a fuel flowrate of 10.6 g/hr (FP = 125). The C_{10} products are omitted for clarity.

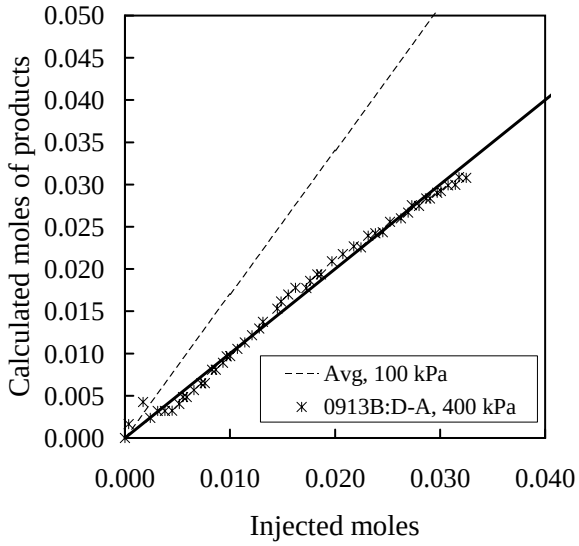

Figure 67: Comparison of moles of product to moles of injected JP-10 in a system with HY zeolite at different system pressures. Fuel flowrate is 2.3 g/hr (FP = 25).

(Fig. 69). The increase in higher carbon components at the higher pressure is easily observed. The overall average conversion at a system pressure of 400 kPa is 53% versus the conversion at atmospheric pressure of 34%.

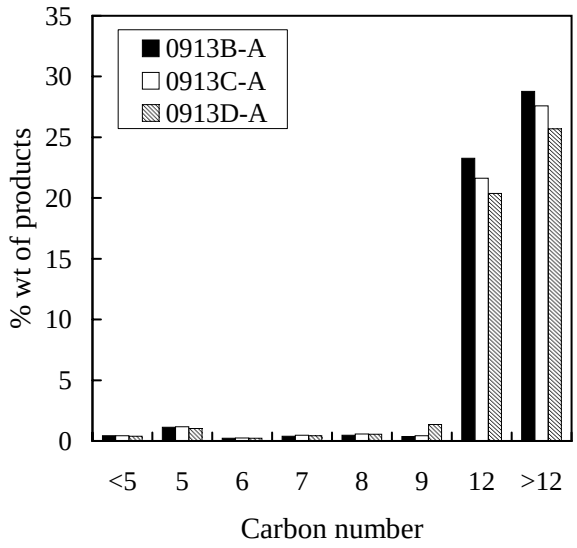

Figure 68: Product composition of test 0913B:D-A with HY zeolite, a system pressure of 400 kPa, and a fuel flowrate of 2.3 g/hr (FP = 25). The C_{10} products are omitted for clarity.

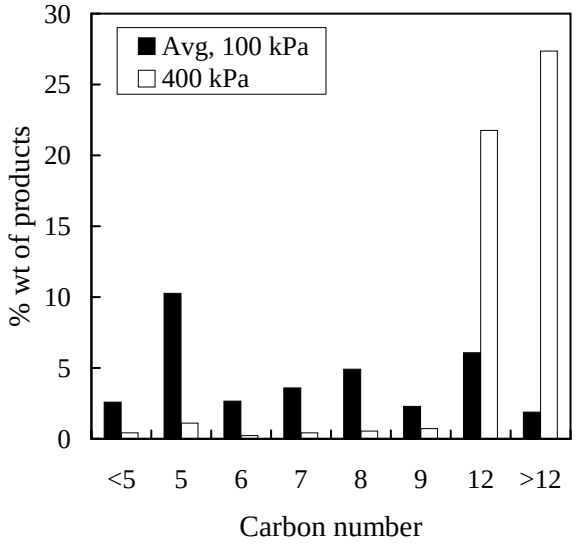

Figure 69: Overall average product composition to determine effect of system pressure with HY zeolite at a fuel flowrate of 2.3 g/hr (FP = 25). The C_{10} products are omitted for clarity.

8.2.6 Effect of reactor temperature

The effect of reactor temperature was studied with HY zeolite at a liquid fuel flowrate of 10.6 g/hr (FP = 125). The mole balance data appears in Fig. 70 for five different temperatures. As the reactor temperature decreases, the mole ratio decreases resulting

in a decrease in the conversion of JP-10 into smaller products. (Fig. 71).

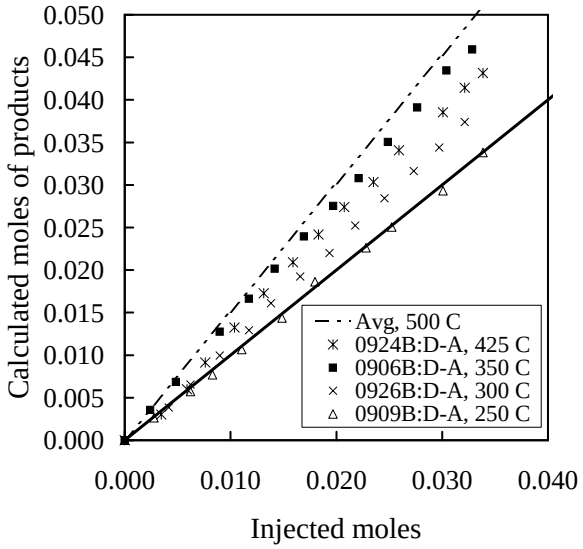

Figure 70: Comparison of moles of product to moles of injected JP-10 in a system with HY zeolite at different reactor temperatures. Fuel flowrate is 10.6 g/hr (FP = 125).

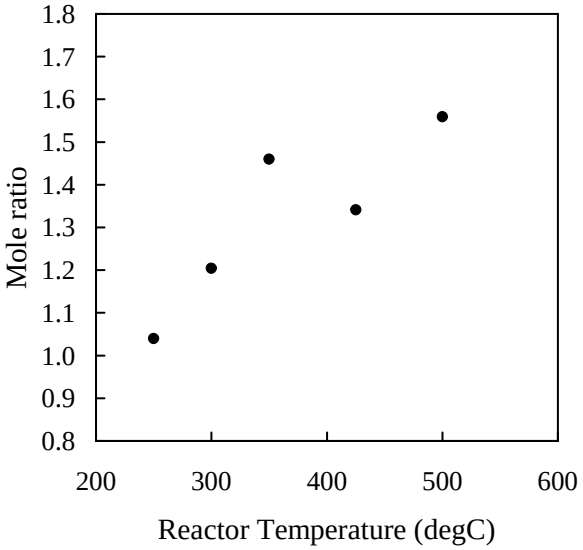

Figure 71: Ratio of moles of products to injected moles as a function of reactor temperature. Fuel flowrate is 2.3 g/hr (FP = 25).

The product distribution from multiple GC samples for each of the tests appears in Fig. 72, 73, 74, and 75.

The overall averaged product distributions for the multiple samples at each reactor temperature appear in Fig. 76.

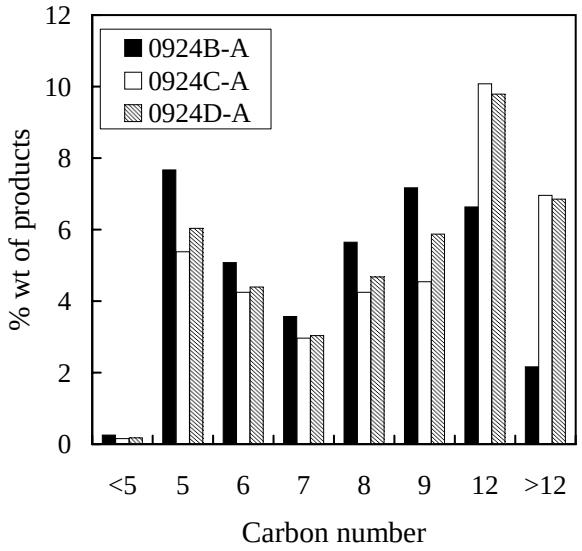

Figure 72: Product composition of test 0924B:D-A with HY zeolite, a reactor temperature of 425°C, and a fuel flowrate of 10.6 g/hr (FP = 125). The C_{10} products are omitted for clarity.

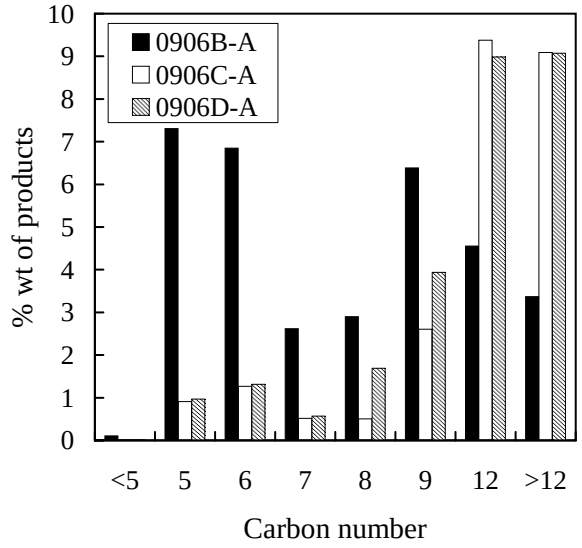

Figure 73: Product composition of test 0906B:D-A with HY zeolite, a reactor temperature of 350°C, and a fuel flowrate of 10.6 g/hr (FP = 125). The C_{10} products are omitted for clarity.

The overall average conversion as a function of the reactor temperature appears in Table 16.

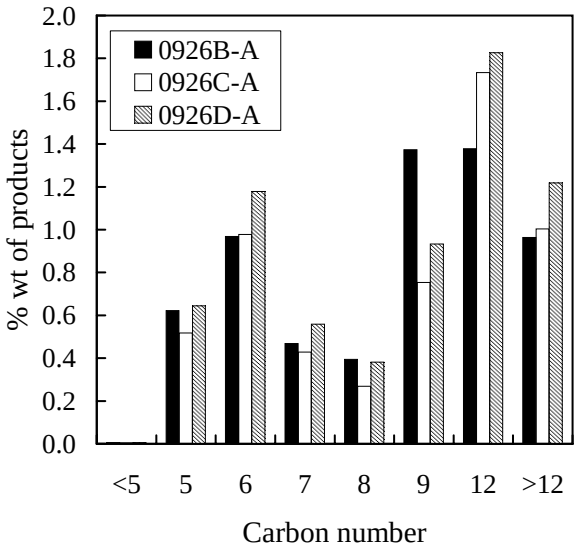

Figure 74: Product composition of test 0926B:D-A with HY zeolite, a reactor temperature of 300°C, and a fuel flowrate of 10.6 g/hr (FP = 125). The C_{10} products are omitted for clarity.

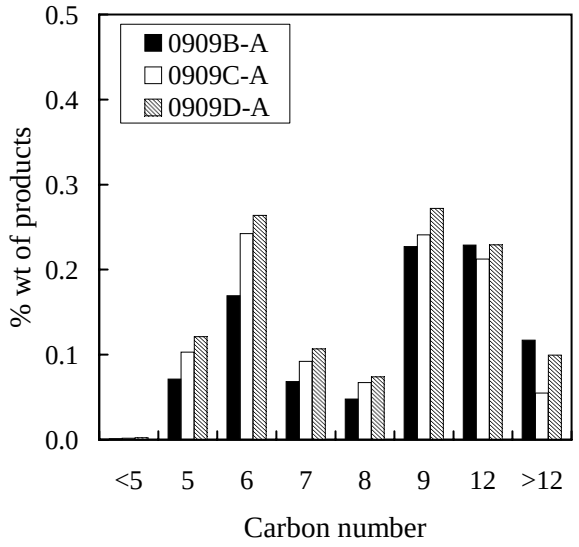

Figure 75: Product composition of test 0909B:D-A with HY zeolite, a reactor temperature of 250°C, and a fuel flowrate of 10.6 g/hr (FP = 125). The C_{10} products are omitted for clarity.

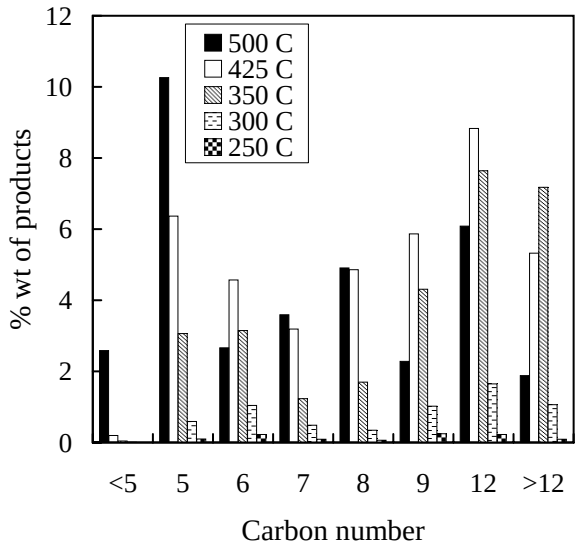

Figure 76: Averaged product distributions for tests with HY zeolite and different reactor temperatures. The C_{10} products are omitted for clarity.

Reactor Temperature (°C)	% Conversion
500	34
425	39
350	28
300	6
250	1

Table 16: Percent conversion as a function of reactor temperature.

Test ID	Sample ID	Fuel Pump	Reactor T, P	Zeolite type	n_p/n_f	Avg % wt. Conv.	% wt. Conv.
0524D,G,I	0524D-C 0524G-F 0524I-H	10.6 g/hr FP=125	500°C 100 kPa	HY 1 g	1.510	31.17	28.13 32.78 32.61
0524K-J	0524K-J	6.2 g/hr FP=70	500°C 100 kPa	HY 1 g	1.026	1.44	1.44
0808B:D-A	0808B-A 0808C-A 0808D-A	10.6 g/hr FP=125	500°C 100 kPa	HY 0.998 g	1.434	31.73	33.93 31.38 29.90
0815B:E-A	0815B-A 0815C-A 0815D-A 0815E-A	2.3 g/hr FP=25	500°C 100 kPa	HY 1 g	2.223	31.54	28.10 33.45 37.70 26.90
0827B:D-A	0827B-A 0827C-A 0827D-A	10.6 g/hr FP=125	500°C 100 kPa	HY 0.983 g	1.583	61.41	56.62 62.34 65.27
0906B:D-A	0906B-A 0906C-A 0906D-A	10.6 g/hr FP=125	350°C 100 kPa	HY 1 g	1.410	28.31	34.09 24.28 26.55
0909B:D-A	0909B-A 0909C-A 0909D-A	10.6 g/hr FP=125	250°C 100 kPa	HY 0.722 g	0.990	1.04	0.93 1.01 1.17
0913B:D-A	0913B-A 0913C-A 0913D-A	2.3 g/hr FP=25	500°C 400 kPa	HY 1 g	0.996	52.56	55.09 52.54 50.06
0916B:D-A	0916B-A 0916C-A 0916D-A	2.3 g/hr FP=25	500°C 100 kPa	HY 0.998 g	1.444	35.52	59.67 20.49 26.39
0918B:E-A	0918B-A 0918C-A 0918D-A 0918E-A	2.3 g/hr FP=25	500°C 100 kPa	HY 1.045 g	1.435	35.70	95.83 17.22 12.72 17.00
0920B:D-A	0920B-A 0920C-A 0920D-A	2.3 g/hr FP=25	500°C 100 kPa	Beta 0.880 g	1.667	70.79	95.03 62.68 54.66
0922D:F-C	0922D-C 0922E-C 0922F-C	2.3 g/hr FP=25	500°C 100 kPa	USY 0.874 g	1.137	10.87	12.08 10.60 9.92

The mole ratio as a function of the average mass conversion fraction is plotted in Fig. 77. The results show reasonable agreement with the simple model of a constant

Test ID	Sample ID	Fuel Pump	Reactor T, P	Zeolite type	n_p/n_f	Avg % wt. Conv.	% wt. Conv.
0924B:D-A	0924B-A 0924C-A 0924D-A	10.6 g/hr FP=125	425°C 100 kPa	HY 1.002 g	1.291	39.20	38.18 38.57 40.84
0926B:D-A	0926B-A 0926C-A 0926D-A	10.6 g/hr FP=125	300°C 100 kPa	HY 1.000 g	1.154	6.20	6.17 5.69 6.75

Table 17: Summary of all catalytic cracking tests and GC samples. Estimated uncertainty in n_p/n_f is ±6.4% and uncertainty in Avg % wt. Conversion y is 12.5%.

product average molar mass and indicate a reasonable correlation between observed mass conversion fraction and molar ratio. Three conditions (0815B, 0909B, 0913B) from the dataset are not visible on this plot because the results are so extreme. We conclude that these points are suspect and should not be used in the overall correlation process. These conditions are set aside and the remainder of the data has been considered as acceptable.

The acceptable data can be fit to a line through the origin to obtain a slope of 1.07 with a regression coefficient of 0.75. Using the analysis of Section 6.3, the average molar mass of the products is estimated to be 0.48·136 g/mol or 65 ± 11 g/mol. Thus, the average number of carbon atoms is 4.8 ± 0.8 assuming a H/C ratio of 1.6. This is reasonable considered the actual distribution of product species and the expectation that breaking the JP-10 rings to form C5 and C6 species is the initial path of decomposition under these conditions.

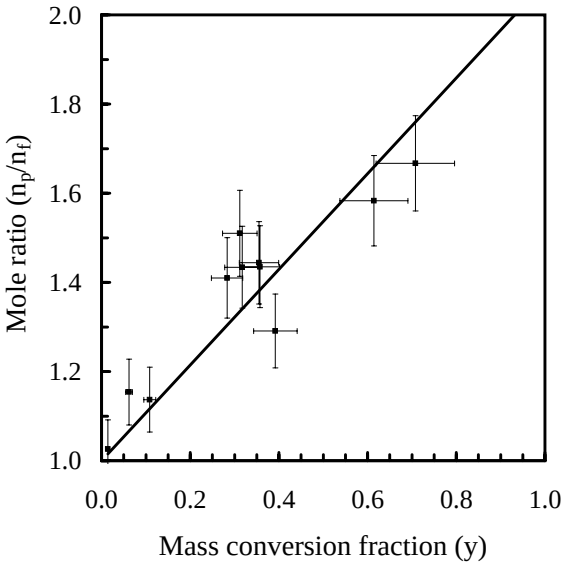

Figure 77: Measured mole ratio n_p/n_f as a function of the mass conversion fraction y for the catalytic cracking tests.

9 Sources of uncertainty

Chemical experiments require careful design to eliminate sources of uncertainty. If the experiment and reaction conditions are not carefully controlled, chemical reaction rates and product composition can be significantly affected. By studying the results of this experiment and actually operating the system, many experimental uncertainties have been identified and attempts have been made to quantify their effect when possible.

9.1 Fuel pump flowrate

The fuel pump calibration appears in Fig. 8. This rate was measured by determining the volume change in the buret over time.

$$R_{FP} = \frac{\Delta V}{\Delta t} = \frac{V_f - V_i}{t_f - t_i} \tag{25}$$

The uncertainty in the time measurement σ_t is 1 second and the uncertainity in the buret level σ_V is 0.05 ml. Using the standard method for the propagation of error [37] the uncertainty in the flow rate measurements is determined.

$$\sigma^2_{R_{FP}} = \left(\frac{\partial R_{FP}}{\partial V}\right)^2 \sigma^2_V + \left(\frac{\partial R_{FP}}{\partial t}\right)^2 \sigma^2_t \tag{26}$$

This yields an average uncertainty of $\pm 5\%$ in the fuel flowrate measurements. The Eldex metering pump documentation lists a reproducibility of $\pm 0.3\%$ where the unit operates more reproducibly if operated at a higher backpressure (greater than 25 psi). In our tests, the backpressure rarely exceeded 1 psi so reproducibility may be an issue. The buret liquid level was observed after opening the FIV and before the pump was started to ensure no movement of the level occurred.

Unexpected increases in the fuel flowrate would result in a higher Reynolds number in the system. Coking and deposition processes would be accelerated resulting in more rapid zeolite deactivation. A higher percentage of larger molecule weight compounds ($> C_{10}$) would be observed.

9.2 Pressure gauge calibration

The pressure gauges have a documented accuracy of 0.25% of full scale. These pressure gauges with output in units of kPa were calibrated against professionally calibrated dial gauges in units of psi. The dial gauge could be read to an uncertainty of ± 1 psi resulting in an uncertainty for the electronic gauge of ± 7 kPa equal to $\pm 7\%$.

9.3 Accumulator height reading

The ruler attached to the accumulator indicator can be read within 0.05 mm. However, after completing a number of tests with the system, the accumulator piston did not

maintain a smooth motion as observed during the first several tests. The piston began sticking resulting in jumps in the accumulator height up to 0.3 cm at a time. Thus, the uncertainty in the accumulator height has been estimated to be ±0.3 cm.

9.4 Measurement of accumulator volume

The design drawings were used to calculate the internal volume of the accumulator including the plumbing up to the inlet valves of the accumulator (Valves A1 and A3 of Fig. 9). Propagation of error yields an uncertainty of the volume estimate equal to ±0.05%.

9.5 Upstream volume measurement

The upstream system volume was determined with a pressure-volume test based on the calculated volume of the accumulator. Using the ideal gas law,

$$V_{sys}^{0} = \frac{P_{accum} V_{accum}}{P_{sys}} \ . \tag{27}$$

The uncertainties for the pressure and accumulator volume are listed above. These are used in the standard equation for the propagation of error [37] the uncertainty in the upstream system volume. This yields an average uncertainty of ±2.2% in the upstream system volume measurement.

9.6 Temperature distribution within a zone

Due to the uneven heating of the rope heaters (as a result of tubing and Swagelok connections of varying dimensions), there is some variation in the temperature distribution (Table 12). The reactor itself has even heating within 2°C over the copper blocks.

The variation in temperature of the system will result in an uncertainty in the computed moles of product obtained from the accumulator position. A variation of ±10 K will cause an uncertainty of ±2% in the computed moles of product n_p at a nominal system temperature of 200°C.

9.7 Purity of JP-10 and N_2

The liquid JP-10 contained dissolved oxygen that likely contributed to the coking problems within the system. No attempt was made to remove the dissolved oxygen during testing.

Industrial nitrogen was used to provide backpressure on the fuel metering pump resulting in a dilution of the cracking products. The requirements on the contaminants are the least restrictive for the bottled gases. These contaminants could affect the reaction initiation and mechanisms, yet the magnitude of this effect is unknown since the cracking mechanisms were not determined.

9.8 Buret level reading

The buret may be read to an uncertainty of 0.05 ml. This has a minor effect on the mole balance calculations (less than 1%).

9.9 Tubing surface reactivity

Stainless steel components are used in the system. At elevated temperatures, hydrocarbons are known to react with these metals. Throughout the operation with the system, most of the components were not changed but the central reactor tube was changed periodically and modifications were made to the section upstream of the reactor. Different mole balance results were observed for clean reactor tubes and reactor tubes coated with carbon deposits.

9.10 Number of active sites due to ion exchange and regeneration

Tests such as MAT or heptane reactivity tests were not completed with any of the zeolites used in this study to quantify the number of active sites based on the completed ion exchange. This was considered out of scope of the project. However, repeat mole balance calculations were similar indicating a similar number of active sites and zeolite activity.

9.11 Variation in zeolite bed height and corresponding level of packing

Initially, as described in the experimental setup of the reactor, the zeolite pellets were constrained in the second spacer tube between two porous disks. The disks were held a constant distance apart (approximately 5 inches). In this orientation, the zeolite pellets were poured into the spacer tube. They filled a length of approximately 3 inches within the second spacer tube and received no additional compaction.

As the porous disks became filled with carbon deposition, they were replaced with plugs of glass wool. In this case, a plug of glass wool was pushed into the second tube then the zeolite pellets were poured in. A second plug of glass wool was pushed into the tube above the pellets. It was pushed down until it stopped against the zeolite. Thus, the pellets did receive additional compaction.

It is unknown exactly how much this could affect the conversion ratio. However, one method to attempt to reduce coking is to mix pellets of an unreactive material (i.e. sand) with the zeolite. This seems to imply that tighter packing of the zeolite reduces the conversion ratio.

9.12 Distance from fuel inlet to beginning of zeolite bed

When the porous disks were used to contain the zeolite bed, the distance from the fuel inlet to the beginning of the bed was constant. However, when the plugs of glass wool replaced the disks, it was more difficult to maintain a constant distance to the beginning of the zeolite bed.

It was also observed that the procedure of using the vacuum pump to complete a final system cleaning could dislodge the plugs of glass wool such that they moved upward within the central reactor tube increasing the distance between the fuel inlet and the bottom of the zeolite bed.

Increases in this distance would result in more time for thermal cracking reactions to take place. Especially if the fuel travels through part of the reactor tube which was typically at 500°C where conversion on the order of 1-3% is expected. Cracking of the JP-10 before coming into contact with the zeolite could increase the conversion of cracking since the smaller molecules would have greater accessibility to the active sites of the zeolite, especially those within the large supercages of the HY zeolite.

Because reaction mechanisms are not known, quantifying this effect is not possible.

9.13 Leakage between accumulator wall and internal piston

Although honing the internal surface of the accumulator significantly reduced the leak rate, a residual leak was present. After testing with the system on a regular basis, a pool of liquid was observed below the accumulator in a line attached to the system fume hood. This suggests that vaporized products were leaking from the system across the accumulator piston and subsequently condensing outside the piston. This effect would act to reduce the number of product moles captured in the accumulator and may act to reduce the movement of the piston. Thus, it is possible to be making more moles of products than are being measured in the piston due to the leak. Based on the maximum leak rate of 2.47 sccm measured previously, a loss of 0.0078% of the mass in the system is expected at a fuel flowrate of 10.6 g/hr, a loss of 0.0190% of the mass in the system is expected at a fuel flowrate of 6.2 g/hr, and a loss of 0.038% of the mass in the system is expected at a fuel flowrate of 2.3 g/hr.

9.14 Residual JP-10 in system

This is expected to be the largest source of error in the system. Due to the large amount of stainless steel plumbing and the many area changes because of the Swagelok components, there is a significant amount of surface area upon which the JP-10 molecules may adhere. Between tests, nitrogen flowed through the hot system plumbing to flush the residual JP-10 out through the vent hood. The vacuum pump was also used to remove any residual products. However, sampling with the GC immediately after flushing the system typically resulted in JP-10 peaks that were still saturating the column.

9.15 Mass conversion fraction

The uncertainty in the mass conversion fraction y was estimated from the GC analysis at the same operating conditions. For the thermal tests, an average y of 0.02985 was calculated from tests 0807C-B, and 1001B:D-A. The Δy for these tests was 0.0037 resulting in an uncertainty of $\pm 12.4\%$. For the catalytic cracking tests, an average y of 0.3425 was calculated from tests 0815B:E-A, 0916B:D-A, and 0918B:D-A. The Δy for these tests was 0.0416 resulting in an uncertainty of $\pm 12.1\%$. We use an uncertainty of $\pm 12.5\%$ as an upper bound on the mass conversion fraction.

9.16 Mole ratio

The uncertainty in the mole ratio is determined based on the measured liquid fuel injected into the system and the calculated product moles based on the accumulator position. Thus, the uncertainty in the mole ratio depends on the uncertainty in the accumulator height measurement, temperature estimation, liquid height in the buret, and the pressure measurement. These uncertainty values are discussed above and when the propagation of error analysis is applied to Eq. 18, this results in a maximum uncertainty in the mole ratio of ± 6.4

9.17 Average molar mass of products

The propagation of error analysis was applied to Eq. 23 to determine the uncertainty of the average molar mass of the products. This was evaluated to be $\pm 17\%$ for the catalytic cracking tests.

10 Feasibility of partial oxidation studies

Two techniques have been proposed for carrying out fuel modification. One was catalytic partial oxidation and the other was catalytic cracking. At the outset of this project, we did not have any experience with these processes so we carried out literature research and also had discussions with Prof. Davis' research group at Caltech. After examining the options, Caltech selected catalytic cracking as being the most worthwhile process to investigate. The technical grounds for this decision are that

a. Catalytic cracking is easier to implement, requiring a less complex and lower temperature reactor. The operating regime is also simpler to define - depending primarily only on temperature and mass flowrate of fuel for the cracking reactor. Since there is no oxidizer in the fuel stream, there are also no issues about flashback or explosion, which are potential problems with partial oxidation. Reactor startup and control is simpler for a catalytic cracking reactor since the catalyst does not have to be "lit" and there is no danger of a runaway reaction or catalyst melting, as can happen in partial oxidation under high temperature conditions.

b. Partial oxidation with air results in a high gaseous nitrogen concentration in the fuel stream. This reduces the energy content of the fuel stream on a mass basis and necessitates a high flowrate fuel injection system in order to compensate for the dilution. This places partial oxidation at a considerable disadvantage to catalytic thermal decomposition, which does not dilute the fuel stream.

c. Experiments [1] in our laboratory on detonation properties of synthetic partial oxidation products have shown that there is no significant improvement in fuel detonation characteristics obtained by partial oxidation. Detonation cell widths for partially oxidized fuel (synthetic mixture) mixed with a stoichiometric amount of air were found to have essentially the same detonation cell width as the parent fuel JP-10. In addition, the energy content of the partially oxidized fuel is lower than the parent fuel, which also makes it less useful for propulsion.

Despite these drawbacks, partial oxidation may still be of interest since the coking problem is so severe for zeolite catalysts. A brief study was carried out on the feasibility of converting the existing catalytic reactor to partial oxidation operation. The results of that study are reported below.

10.1 Required reactor modifications

The current reactor design is appropriate for catalytic cracking (referred to in the test plan as catalytically cracked fuel) using a bed of zeolites as the catalyst with maximum reactor

temperatures of 500°C and downstream temperatures of 200°C. The GC analysis system with a FID is also set up only for hydrocarbons. Reacting and analyzing partial oxidation products will require significant modifications to the existing reactor and instrumentation. It is not simply a matter of introducing air into the feedstream and changing the catalyst in the existing reactor.

10.1.1 Temperature limitations

Partial oxidation, particularly at high oxygen concentrations, results in a high temperature product stream. The actual temperature has to be determined experimentally, but since there is no actual data available, we have used equilibrium computations to estimate the maximum temperature of the product stream. The results for a mixture of JP-10 and air at various equivalence ratios are shown in Fig. 78.

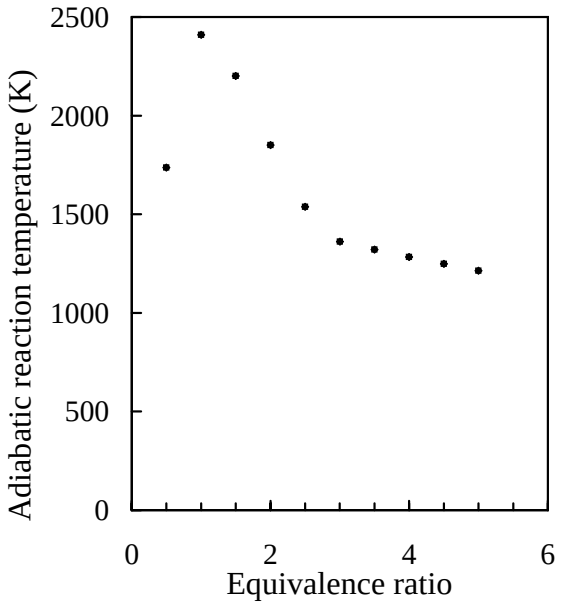

Figure 78: Adiabatic flame temperatures for complete combustion of mixtures of JP-10 and air initially at 300°C and 100 kPa. Equivalence ratio defines the initial mixture as $\phi C_{10}H_{16} + 14O_2 + 52.64N_2$.

The optimum operating conditions are not known but are expected to be at an equivalence ratio greater than 2.8 and possibly as high as 5. The goal is to optimize the energy content of the product stream. The actual products for a given reactor can be determined only by experiment but the equilibrium distributions (corresponding to the temperatures in Fig. 78) can be estimated and are given in Fig. 79. As indicated, the equivalence ratio has to be at least 2.8 so that CO_2 and H_2O are not formed.

From these considerations, we see that the reactor and the region downstream will be operating at temperatures up to 1300 K or about 1000°C. At present, the maximum operating temperature of the reactor is 500°C and the downstream components, valves,

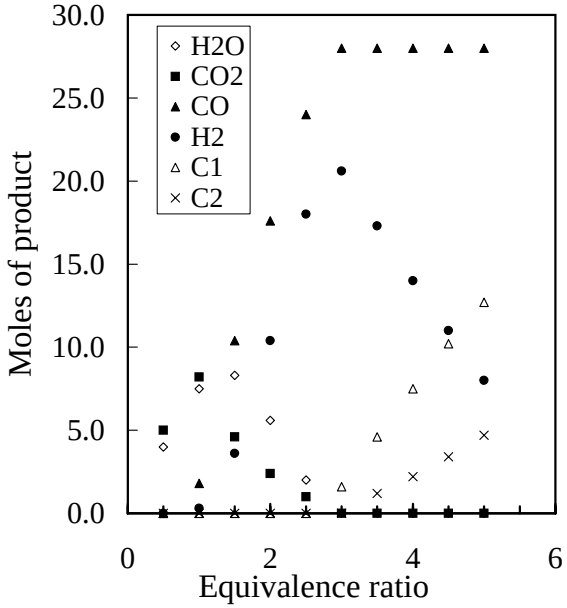

Figure 79: Equilibrium product distribution for complete partial oxidation of JP-10 mixed with air. Initial temperature is 300°C and pressure is 100 kPa. Equivalence ratio defines the initial mixture as $\phi C_{10}H_{16} + 14O_2 + 52.64N_2$.

and accumulator are limited to 200°C due to the elastomer seals. If we are going to use the existing accumulator and plumbing downstream of the reactor, a heat exchanger will have to be used to cool the products before reaching these components.

A new reactor section and a heat exchanger will have to be designed, constructed, installed, and tested in order to do these studies. A latter section addresses the redesign required on the current system.

10.1.2 Catalyst

Zeolite catalysts are not useful for partial oxidation. Instead, transition metals or metal complexes are typically used for partial oxidation catalysts. We would have to obtain materials and carry out preliminary experiments to determine feasibility and yield. The residence time in the reactor and flashback to the upstream fuel-air mixture are also factors in this type of reactor. This means that a different type of fixture is required to hold the catalyst and needs to incorporate a fine screen or porous plate that can be used as a flame arrestor. The reactor tube will reach high temperatures once the catalyst "lights off" and will have to be insulated rather than placed in contact with the existing reactor heating system. In addition, the extent of conversion will depend on the residence time, controlled by the length of the reactor.

10.1.3 Instrumentation

Caltech will have to install a different column in the GC in order to analyze CO and H_2. Two different carrier gases may have to be used; He for the CO and N_2 for the H_2 analysis. A TCD will have to be used for H_2 rather than the existing FID that is used for HC compounds. Caltech can do some analysis (of the HC components and CO) with the existing FID. The mole balance that is used in the present experiments will not be an effective diagnostic tool since the added nitrogen reduces the sensitivity of this technique. The estimated ratio of product and reactant molar amounts is shown in Fig. 80 for JP-10-air mixtures. As shown, this ratio will never exceed 1.5, making it

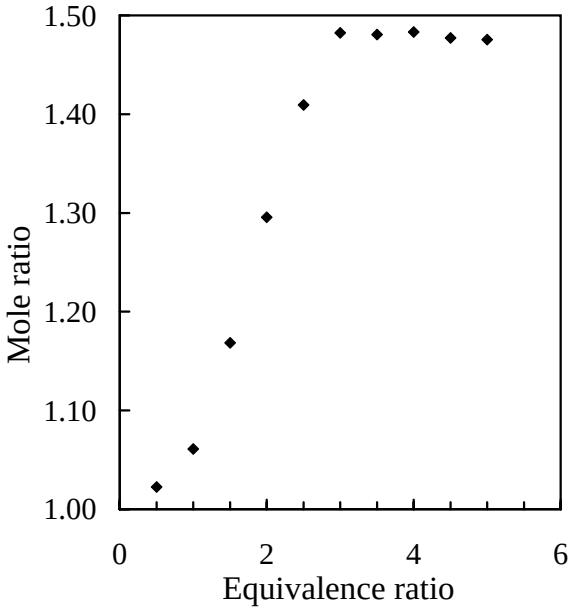

Figure 80: Estimated ratio of product to reactant mole amount as a function of equivalence ratio for JP-10-air mixtures. Equilibrium partial oxidation of JP-10-air mixtures, initial temperature of 300°C, and pressure of 100 kPa. Equivalence ratio defines the initial mixture as $\phi C_{10}H_{16} + 14O_2 + 52.64N_2$.

difficult to use as a diagnostic since the accumulator leaks, and sticking of the piston seals introduces substantial uncertainty in the measurement.

10.1.4 Air addition

Air will have to be metered into the region upstream of the catalyst and mixed with the fuel. The current reactor had provisions only for simple rotameters that were originally intended for controlling N_2 and CH_4 flow that were to be used for fuel stream dilution and zeolite catalyst activation. Later, we discovered that the CH_4 was not needed and that the rotameter operation was not stable with our system. The rotameters were disconnected and were never used in our catalytic cracking tests.

The air flow and fuel flowrate will have to be controlled in order to have a known equivalence ratio within the reactor. The existing fuel pump can be used to control the fuel flowrate. Several possibilities exist for controlling the air flowrate. One is the very simple technique of using a choked flow orifice in the line coming from the air bottle. This will work for only a fixed number of fuel flowrates and stoichiometries. The orifice will also have to be extremely small since the liquid fuel flowrates are very low according to our experience with the existing reactor. Small orifices can get clogged easily by the soot and coking products that are always present in very rich oxidation processes. In this case, a mass flow controller may have to be used in order to regulate the air flowrate properly.

10.2 Design constraints and preliminary design of partial oxidation reactor

The reactor must be redesigned to operate at temperatures associated with catalyst ignition and exothermic oxidation reactions during continuous operation. As shown in Fig. 78, temperatures greater than 1000°C have been predicted assuming complete combustion of JP-10 mixtures. The range of variation between these adiabatic flame temperatures and the actual temperature produced by catalytic combustion is unknown. Due to the lack of experimental information, we have used the conservative equilibrium temperature in developing a design.

The existing reactor tube consists of a 1/2-inch OD, 15-inch long stainless steel tube with the zeolite section encased in two heated copper blocks. The maximum operating temperature is 500°C. Quartz tubing is commonly used in partial oxidation microreactors [38, 39, 40] due to the high operating temperatures observed in experiments with alkanes and cyclohexane and the known surface reactivity of metal tubing. A wire gauze catalyst is typically used in syngas production, oxidation of cyclohexane, and olefin formation. One common metal is 90% Platinum-10% Rhodium by mass. The gauze is fixed within the quartz reactor tube by clamping it between two quartz tubes and wrapping with a fiber woven with Al_2O_3-SiO_2 fibers as described in O' Connor and Schmidt [38]. New fittings will be required in order to connect the quartz tube to the existing Swagelok plumbing. To monitor reaction progress, a quartz-enclosed thermocouple must be installed in the region downstream of the catalyst. The location must be adjustable so that the position relative to the catalyst is known.

The oxidation reactions are initiated spontaneously in the presence of the catalyst at sufficiently high temperatures. However, new catalysts will require activation before reproducibility in the temperatures, conversion rates, and selectivities of the feed are achieved [38]. For experiments with 90% Pt-10% Rh wire gauze, activation was achieved by reaction in high purity n-butane-oxygen with molar ratios between 1.4-2.0 for approximately 10 hours [38]. Activation with cyclohexane-oxygen alone was not obtained in a similar length of time.

The existing preheat section (referred to as the evaporator section) is capable of temperatures up to 350°C; however, it is currently a significant distance upstream of

the catalyst location. If the preheat temperature of the feed gases is greater than the ignition temperature, no external heater on the catalyst is required [39]. Otherwise, an external heater must be applied to the catalyst and quickly removed after surface ignition or the temperature will rise to unacceptable values within a few seconds (or less) in a transition mode [39]. This process is not well documented and ignition temperatures on such catalysts are not well defined. Cyclohexane-oxygen mixtures in the 0.4-5 molar feed ratios ignite at 200-250°C [38]. Ignition in methane was experimentally measured to be >600°C and ignition in butane was measured to be around 300°C [39]. Because ignition in methane is difficult, it is possible to initiate ignition with NH_3-air and then replace NH_3 with CH_4 and air and O_2 [39]. The catalyst type appears to affect the surface ignition temperature and values of 300 - 400°C for methane, ethane, propane, and isobutane were experimentally measured with resistively heated platinum foil [40]. Due to the lack of data for ignition temperatures of JP-10 mixtures on the catalyst, the ignition temperature will have to be experimentally determined. The ignition temperature is expected to be similar to that of the higher carbon number alkanes and cyclohexane.

Although the existing catalyst heater can achieve the ignition temperatures for the higher carbon number compounds, it is not an acceptable type to use since it is not possible to quickly remove the heat source from the catalyst once ignition is achieved. The steady-state operation or "autothermal" temperatures were measured to be between 400-1000°C for methane, ethane, propane, and isobutane [40]. It is important not to allow the temperature to go too high or a flame may propagate upstream into the reactants. Veser and Schmidt measured catalyst temperatures of between 1000-1500°C immediately before observing a flame [40].

The most likely heater types would utilize radiant heat or hot air. Ignition with an external heater requires careful system operation because a suitable path must be found from ambient temperature to steady state operation that avoids the possibility of explosive ignition (a serious safety hazard), catalyst melting, or the formation of coke deposits [39]. This path of ignition is not known for JP-10 mixtures and will require significant experimental testing. Schmidt et al. warns that small thermal time constants in such micro-reactors prevent the standard feedback procedure that utilizes temperature sensing devices in the reactor bed and manual adjustment of preheat temperatures or wall heat transfer. This manual interaction becomes extremely difficult or impossible during transients of startup (ignition) and shutdown (extinction) [39]. In some cases, the reactor may be destroyed [39].

Fuel and oxidizer must be accurately metered into the system to maintain the desired molar ratios and operate the reactor safely. Previously employed flow rates of JP-10 in the catalytic cracking experiments were 10.6, 6.2, and 2.3 g/hr. These values are used along with the reaction equation of Fig. 80 to predict the required mass flowrates of oxygen and nitrogen for two different equivalence ratios (Table 18).

After catalyst light off, the product stream resulting from the oxidation of JP-10 mixtures is likely to be in excess of 1000°C (Fig. 78). Due to the downstream temperature limits of the existing system components, the product gases should be cooled to at least 200°C. This could be accomplished with a counterflow heat exchanger. Based on the

Equivalence Ratio	JP-10 (g/hr)	O_2 (g/hr)	N_2 (g/hr)	Equivalent Air (g/hr)
3	10.6	11.6	38.2	50.1
3	6.1	6.7	22.1	28.9
3	2.3	2.5	8.3	10.9
10	10.6	3.5	11.5	15.0
10	6.1	2.0	6.6	8.7
10	2.3	0.8	2.5	3.3

Table 18: Predicted mass flowrates, m, for JP-10 mixtures.

mass flowrates of the feed stream (Table 18), the mass flowrate of the product gases m_P can be calculated.

$$m_{JP-10} + m_{O_2} + m_{N_2} = m_{JP-10} + m_{Air} = m_P$$

A preliminary analysis was carried out to determine the operating parameters required for a shell and tube heat exchanger to reduce the temperature of the product gases from 1000°C to 200°C. Based on conservative predictions of convection coefficients, the maximum flowrate for the product gases and a substantial temperature rise in the working fluid, a heat exchanger of only a few inches in length and a flowrate smaller than 0.1 gal/min is required. These values are based on a working fluid of water initially at 20°C. The heat exchanger can be constructed of Swagelok fittings and stainless steel tubing. Industrial water would be used for cooling. The heat exchanger outlet would attach to existing plumbing just upstream of the valves for the accumulator.

The GC analysis system as discussed above will require upgrading to enable detection of the partial oxidation components. A new PLOT-Q capillary column and a thermal conductivity detector are required. Although the thermal conductivity detector will enable detection of non-HC species, the calibration of the detector is more involved than for the existing FID. The response at a specific retention time to a given component is directly proportional to its concentration, velocity, and inversely proportional to its specific heat. Unlike the FID, the TCD is sensitive to H_2, O_2, and N_2 in addition to the organic compounds. One disadvantage of the TCD is that it is less sensitive than the FID by a factor of 10^5 [29].

10.3 Value to the overall program

The modified fuels created in this program were intended to be used in a PDE simulator that was developed in a separate task. The current simulator fuel injection system cannot accommodate high temperature products so it will not be possible to inject at the conditions created at the exit of the reactor. In addition, the valve body and air streams are cold, causing condensation of the heavier hydrocarbon components. Therefore, a realistic partial-oxidation product stream cannot actually be tested in the existing simulator. Work by previous investigators has defined what a typical composition might

be for partial oxidation at various equivalence ratios for JP-10. These data can be used to create a synthetic mixture that could be purchased from a commercial gas supplier and used to fuel the simulator. This would be more controlled and quite a bit more cost effective than attempting to create these mixtures with a new reactor facility.

11 Pre-mixed partial oxidation experiments

Experiments were conducted to determine the feasibility of creating partial oxidation products by using premixed combustion. A series of experiments was carried out in an explosion vessel with mixtures of JP-10 and air. An initial burn of a rich mixture was used to create the partial oxidation products. These products were allowed to cool, air was added to create a stoichiometric mixture, and a second burn was performed. Pressure measurements, high-speed video schlieren, and ideal thermodynamic computations were used to characterize the mixtures. This section of the report describes the experimental facility, the test procedure, results, and analyses of the data.

11.1 Experimental facility and procedure

The experiments were carried out in an 11.25 liter explosion vessel, shown in Fig. 81, without the surrounding insulation. The vessel was equipped with an Endevco 8530B-200

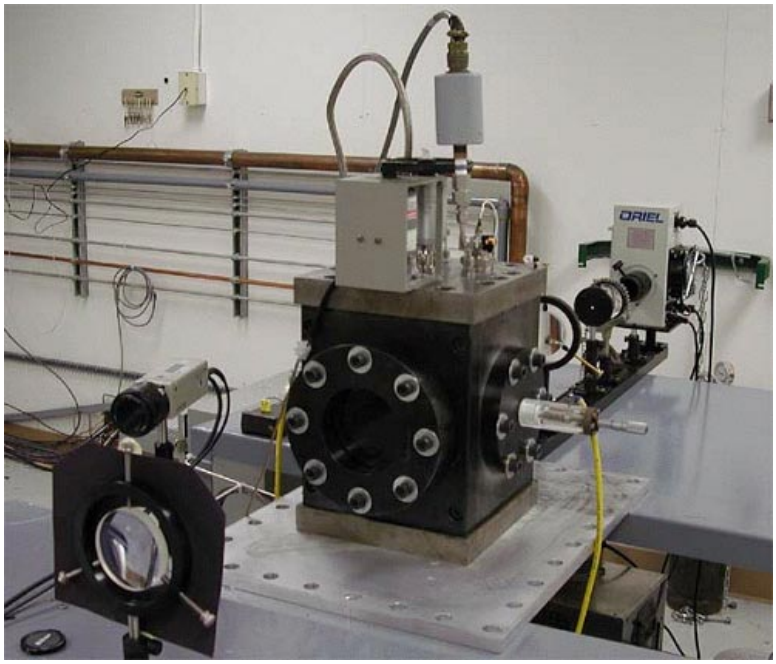

Figure 81: Constant volume combustion vessel for pre-mixed partial oxidation experiments.

pressure transducer, thermocouple, two-sided optical access for flame visualization and a spark ignition system consisting of a capacitor discharge system and two electrodes. The facility was heated to an average of 107°C to vaporize the liquid JP-10 that was injected into the vessel through a self-sealing septum with a 1-cc syringe. A schlieren system was used to visualize the combustion fronts. The images were recorded on a Phantom IV digital camera at 512×512 resolution and 1000 frames/s. The schlieren video was used to determine the flame geometry, speed, and verify flamability limits.

The test procedure began by evacuating the vessel and gas handling system with the vacuum pump. Liquid JP-10 was injected into the vessel to achieve a partial pressure of 1.4 kPa. Oxygen and nitrogen were then added to the vessel by the method of partial pressures (Table 19) to obtain the desired equivalence ratio.

$$\phi C_{10}H_{14} + 14(O_2 + 3.76N_2) \tag{28}$$

Equivalence Ratio ϕ	P_{JP-10} (kPa)	P_{O_2} (kPa)	P_{N_2} (kPa)	P_1 (kPa)
1	1.4	19.9	74.7	96
1.5	1.4	13.1	49.4	64
2	1.4	9.8	36.8	48
2.5	1.4	7.9	29.7	39
3	1.4	6.6	24.9	33
3.5	1.4	5.8	21.8	29
4	1.4	5.0	18.6	25
4.5	1.4	4.3	16.3	22
5	1.4	3.9	14.7	20

Table 19: Partial pressures of the initial mixture of the first burn for varying equivalence ratios.

A fan stirred the mixture for 5 minutes to ensure mixture homogeneity. A LabView program was used to synchronize ignition with recording the pressure signals, including $(P_{max})_1$, and the schlieren images.

After combustion, the products quickly cooled to the vessel temperature (average of 380 K) and the final pressure of the products $(P_p)_1$ was recorded. Additional oxygen and nitrogen were then added to achieve an equivalent stoichiometric mixture at 100 kPa and 380 K. The amount of air added to the mixture was

$$(\phi - 1)14(O_2 + 3.76N_2)\ . \tag{29}$$

The mixture was again stirred and the initial pressure P_2 recorded before the second burn was completed. Pressure histories and schlieren video were recorded.

11.2 Pressure and product composition results

A summary of the recorded pressures for the first and second burn at each initial equivalence ratio appears in Table 20.

The recorded pressure histories for the first burn appear in Fig. 82 and 83. As the equivalence ratio increases and the mixture becomes increasingly richer, the maximum pressure decreases. The flame develops very slowly and then is observed to extinguish in

ϕ	Burn 1 P_1 (kPa)	Burn 1 $(P_{max})_1$ (kPa)	Burn 1 $(P_p)_1$ (kPa)	Burn 2 P_2 (kPa)	Burn 2 $(P_{max})_2$ (kPa)
1	96.01	644.43	95.04	95.04	-
2	48.15	430.6	50.8	97.86	-
2.5	39.03	367.73	46.2	102.9	432.7
3	32.91	316.01	43.03	106.4	560.54
3.5	29.03	272.5	39.93	108.3	577.36
4	24.98	191.54	37.31	109.34	624.45
4.5	21.99	94.19	31.63	106.34	623.2
5	20.1	68.96	28.08	-	-

Table 20: Summary of the initial, maximum and final pressures for the first and second burns

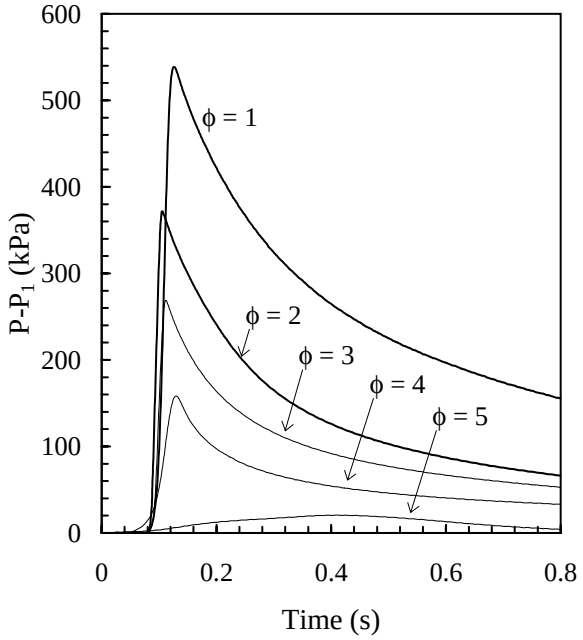

Figure 82: Pressure histories of the first burn for ϕ equal to 1, 2, 3, 4, and 5.

the schlieren images for the case of ϕ equal to 5 which explains the small pressure rise of only 8 kPa.

Equilibrium predictions of mole concentrations and pressures for the first burn were made with STANJAN [41]. Adiabatic, constant volume, complete-combustion calculations were performed for each equivalence ratio at an initial temperature of 380 K and at initial pressures P_1 corresponding to the experimental conditions. The numbers of moles have been normalized by the initial moles of JP-10.

$$C_{10}H_{14} + n(O_2 + 3.76N_2) \tag{30}$$

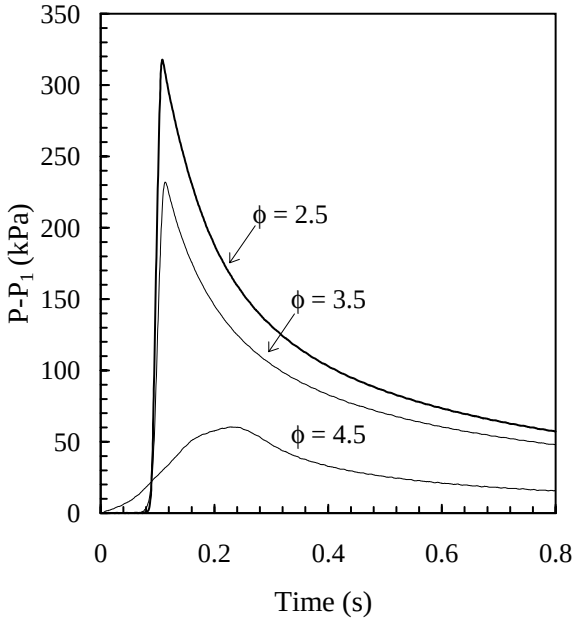

Figure 83: Pressure histories of the first burn for ϕ equal to 2.5, 3.5, and 4.5.

where n is $14/\phi$. Comparison between the equilibrium predictions and experimental values of ΔP_1 appear in Fig. 84. Using the ideal gas law with the first law of thermodynamics, the maximum pressure rise during the combustion event can be related to the equivalent chemical energy release Q of the mixture.

$$Q = U_{max} - U_1 \tag{31}$$

$$= \frac{n_{max}\tilde{R}T_{max}}{\gamma - 1} - \frac{n_1\tilde{R}T_1}{\gamma - 1} \tag{32}$$

$$= \frac{(P_{max}) - P_1}{(\gamma - 1)V} \tag{33}$$

As the equivalence ratio ϕ is increased, the effective energy release Q decreases since the C and H atoms are only partially oxidized.

The corresponding normalized moles of products for the first burn of JP-10 and air at different equivalence ratios appear in Fig. 85. At the stoichiometric condition (ϕ=1), the approximate reaction predicted by the equilibrium calculations is

$$C_{10}H_{14} + 14(O_2 + 3.76N_2) \rightarrow 2.2CO + 7.8CO_2 + 7.4H_2O + 52.64N_2 + \text{traces}(O_2, H_2) \tag{34}$$

All of the fuel is oxidized completely to major products, mostly CO_2 and H_2O. At an equivalence ratio of 2.5, the approximate reaction predicted by the equilibrium calculation is

$$C_{10}H_{16} + 5.6(O_2 + 3.76N_2) \rightarrow 9.6CO + 7H_2 + 21N_2 + \text{traces}(CO_2, H_2O) \tag{35}$$

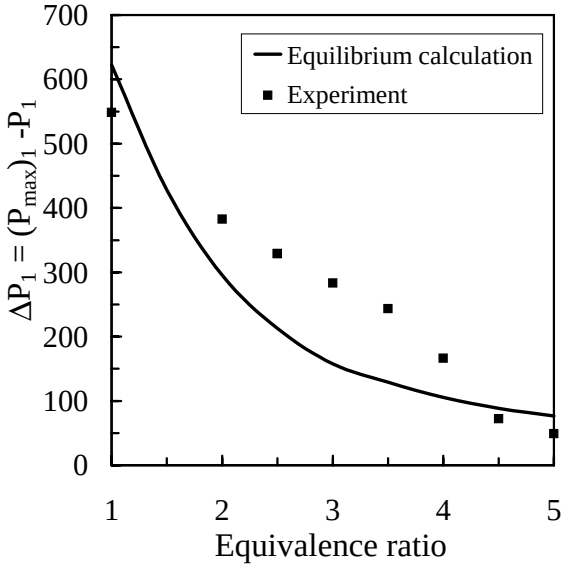

Figure 84: Equilibrium predictions and experimental data for the peak pressure rise in the first burn ΔP_1 as a function of equivalence ratio.

The fuel is oxidized to only CO and H_2. There is not enough O_2 to create H_2O or CO_2 for $\phi \geq 2.5$. At an equivalence ratio of 4, an approximate reaction is

$$C_{10}H_{16} + 3.5(O_2 + 3.76N_2) \rightarrow 7CO + 4H_2 + 13N_2 + 1.6CH_4 + \text{traces}(C_2H_x) \; . \qquad (36)$$

The excess fuel forms CH_4 and trace amounts of higher hydrocarbons. The H_2, CO, CH_4, and other hydrocarbons act as the fuel for the second burn when air is added to the system.

After the first burn with JP-10 and air, the products were allowed to cool to the vessel temperature of 380 K. The ratio of initial and final pressures is equal to the ratio of product moles to the reactant moles since the volume is constant. The ideal gas law relates these two ratios.

$$\frac{(P_p)_1}{P_1} = \left(\frac{(n_p)_1 RT}{V}\right)\left(\frac{V}{n_1 RT}\right) = \frac{(n_p)_1}{n_1} \qquad (37)$$

Two predictions of the cooling process to the initial temperature of 380 K were conducted with STANJAN. The equilibrium case calculates the concentrations assuming the reactions progress extremely quickly and the composition is at equilibrium at 380 K. The frozen case calculates the concentrations assuming the reactions progress extremely slowly and the composition is fixed at that found for the adiabatic conditions associated with the first burn (Fig. 85). The two predictions are compared with the experimental data in Fig. 86.

The experimental data generally lie between the two limiting predictions of equilibrium and frozen product concentrations. The dependence of maximum temperature

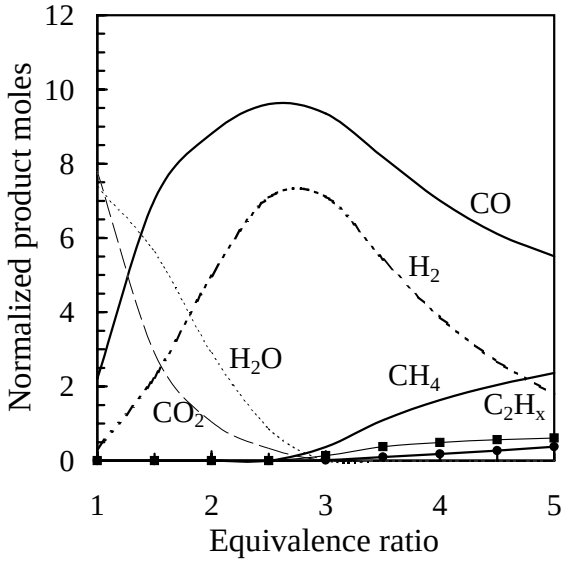

Figure 85: Normalized moles of products for $C_{10}H_{16} + n(O_2 + 3.76N_2)$ as a function of the equivalence ratio. N_2 product moles are omitted for clarity. Equilibrium computations under adiabatic, constant volume complete combustion conditions.

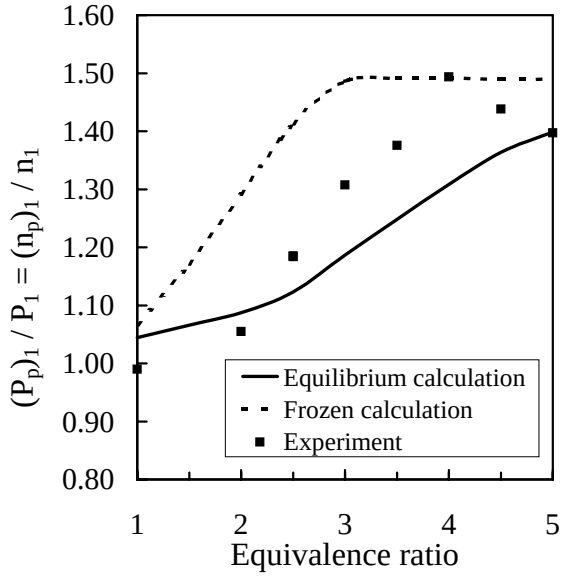

Figure 86: Predicted and experimental values of P_2/P_1 as a function of equivalence ratio.

(Fig. 87) during the first burn (as predicted by the equilibrium calculation) helps explain the trend of the data shown in Fig. 86. The peak temperature decreases with increasing equivalance ratio. For $1 < \phi < 2.5$, the temperature is sufficiently high that the reactions in the products proceed rapidly before heat transfer to the vessel walls reduces the gas temperature and the chemical reactions cease. For these cases, the equilibrium model

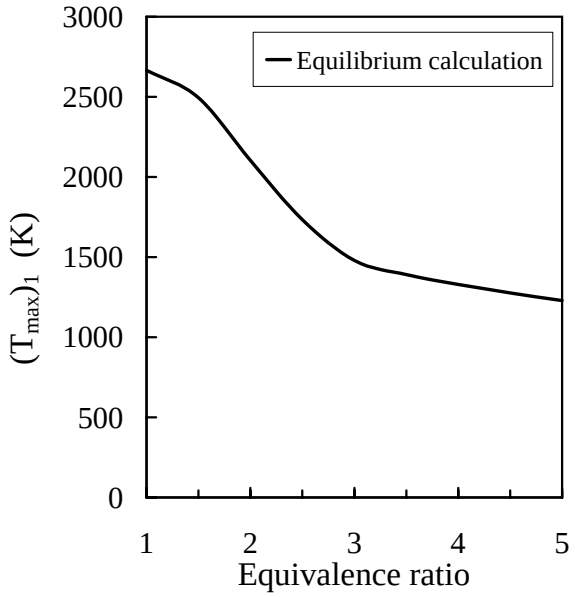

Figure 87: Equilibrium predictions of the maximum temperature during the first burn as a function of equivalence ratio. Adiabatic, constant volume, complete combustion process.

appears to be appropriate. As the equivalence ratio increases, $\phi > 2.5$, the peak temperature drops and the rate of the chemical reactions decreases. The reaction apparently does not have time to take place before the gas cools to the vessel temperature. For these cases, the frozen model appears to be appropriate.

For equivalence ratios greater than 4, combustion produces a significant amount of soot, decreasing the final pressure relative to the predictions which do not account for the formation of carbon-containing solids. In addition, incomplete combustion occurs, resulting in a lower pressure rise in comparison to the complete combustion prediction. For equivalence ratios greater than 5, the combustion could not be initiated. This is consistent with the very low pressure rise observed at ϕ=5 (Fig. 82).

The normalized product distributions for the cool gas assuming equilibrium composition appear in Fig. 88. For equivalence ratios near stoichiometric, the products are composed almost entirely of H_2O and CO_2. For the higher equivalence ratios, the products are composed almost entirely of CO and CH_4. The product distribution for the cooled gas assuming a frozen composition is the same as in Fig. 85.

After the products have cooled to the initial temperature of the vessel, oxygen and nitrogen are added to form an equivalent stoichiometric mixture. The mixture is ignited and the pressure histories are recorded. The initial pressure for the second burn after the addition of the oxygen and nitrogen is approximately 100 kPa, refer to Table 20 for the actual values. The recorded pressure histories for the second burn appear in Fig. 89 and 90. As the first burn equivalence ratio increases, the maximum pressure of the second burn at an equivalent stoichiometric condition increases. This is a result of the partial

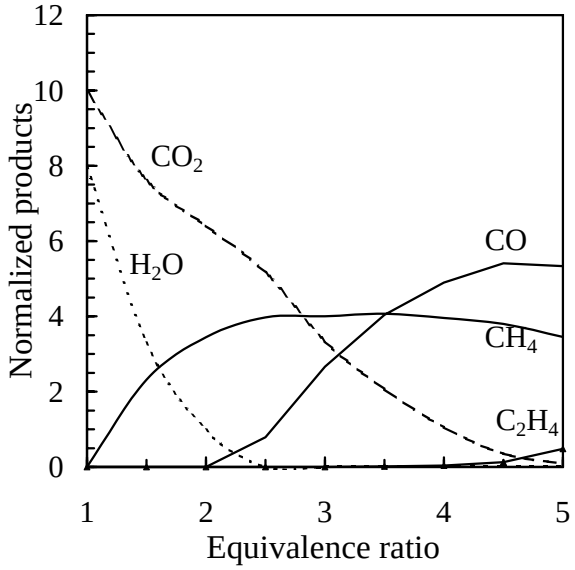

Figure 88: Normalized moles of cooled products calculated with equilibrium concentrations as a function of the first burn equivalence ratio. N_2 product moles are omitted for clarity.

oxidation products (CO, H_2, and hydrocarbons) of the first burn now being fully oxidized by the added oxygen. No second burn was achieved for values of ϕ less than 2.5 since only a very small fraction of the products of the first burn are incompletely oxidized. In these cases, the mixtures are too lean to be flammable.

Adiabatic, constant volume explosion pressure and species computations were carried out with STANJAN for the second burn. These computations were done using both frozen and equilibrium compositions resulting from the first burn. The predictions are compared with the experimental data for ΔP_2 in Fig. 91. The horizontal lines in the figure correspond to the maximum pressure rise realized for the experimental data (548 kPa) and the predicted value (615 kPa) for stoichiometric combustion of JP-10 and air at 100 kPa and 380 K. In both the predicted and experimental cases, the maximum pressure rise obtained by combusting products of rich JP-10 combustion in air is less than the pressure rise obtained by combusting a stoichiometric mixture of JP-10 in air.

We define an effectiveness factor ϵ for the second burn

$$\epsilon = \frac{(\Delta P)_2}{(\Delta P_1)_{\phi=1}} \ . \tag{38}$$

The effectiveness is a measure of chemical energy conversion in the second burn as compared to that obtained by the stoichiometric combustion of JP-10 in air at the same initial conditions. The effectiveness is zero for cases in which no first ($\phi \geq 5$) or second ($\phi < 2.5$) combustion event occurred. In both the experimental data and predictions based on equilibrium calculations, the effectiveness is always less than 1 implying that partial oxidation releases less energy than would be released if JP-10 in air at stoichio-

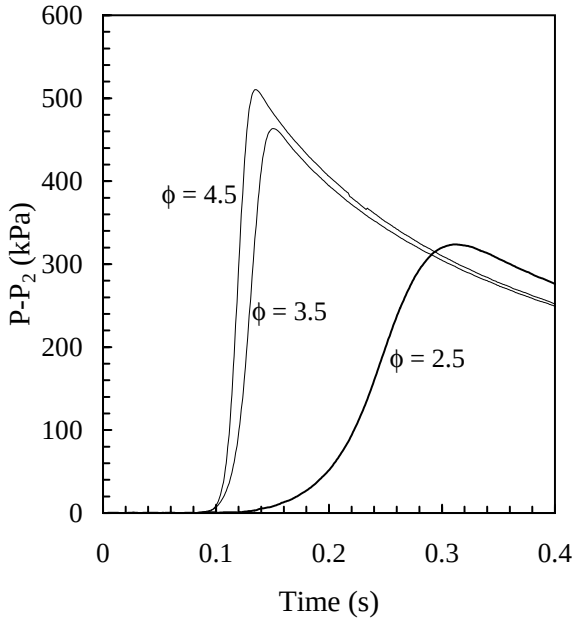

Figure 89: Pressure histories of the second burn for ϕ equal to 2.5, 3.5, and 4.5.

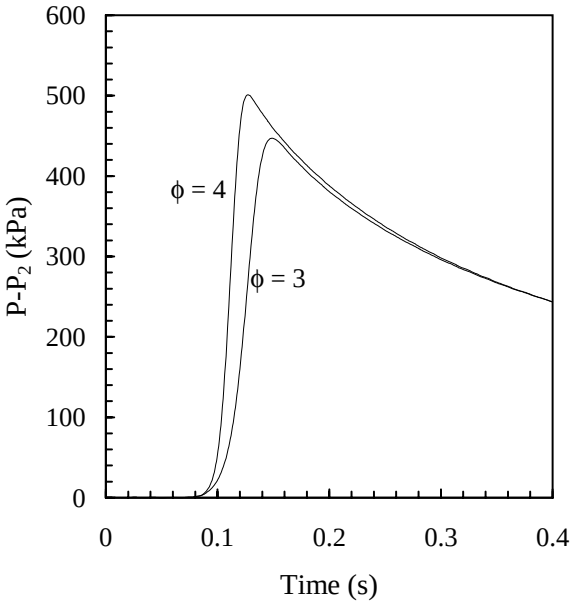

Figure 90: Pressure histories of the second burn for ϕ equal to 3 and 4.

metric conditions was burned directly (Fig. 92).

The equilibrium product distributions have been computed for the second burn. The case of starting with the frozen composition (Fig. 85) for the first burn is shown in Fig. 94. The case of starting with the equilibrium composition (Fig. 88) for the first burn is shown in Fig. 93. In both cases, the results have been normalized to one mole of fuel and the

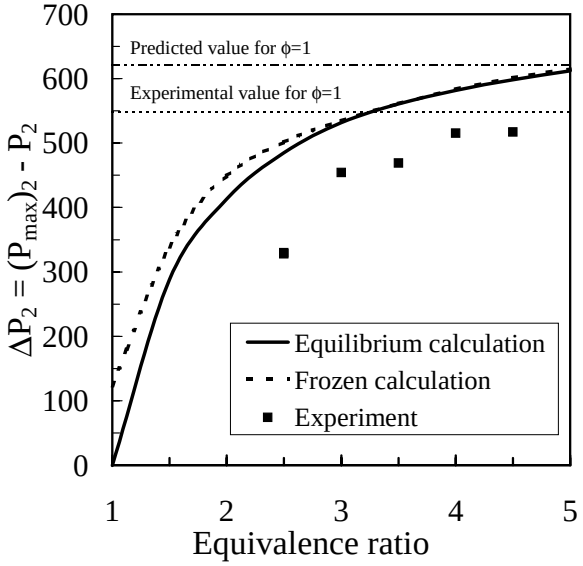

Figure 91: Predicted and experimental values of ΔP_2 as a function of equivalence ratio.

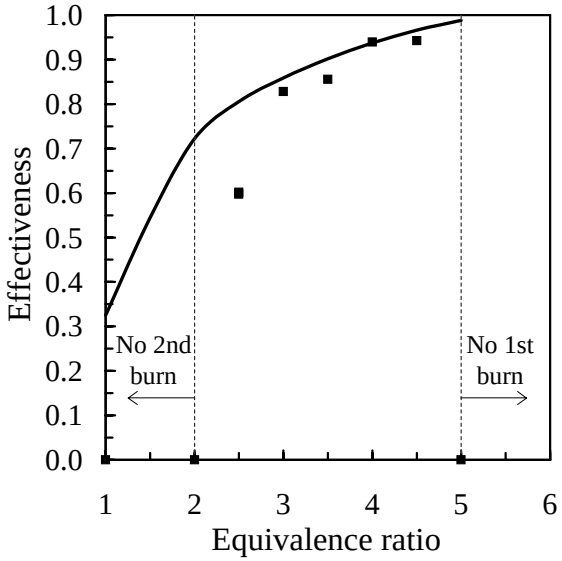

Figure 92: Predicted and experimental effectiveness values as a function of the first burn equivalence ratio.

major products are CO_2, H_2, and CO.

A decrease in the product concentrations of CO_2 and H_2O occurs as the first burn equivalence ratio increases (Fig. 93 and 94). The maximum temperature of the second burn increases with equivalence ratio as shown in Fig. 95. Thus, the decrease in CO_2 and H_2 can be attributed to dissociation at the higher temperatures. The slightly higher temperature for the reaction with the frozen reactants results in more dissociation as

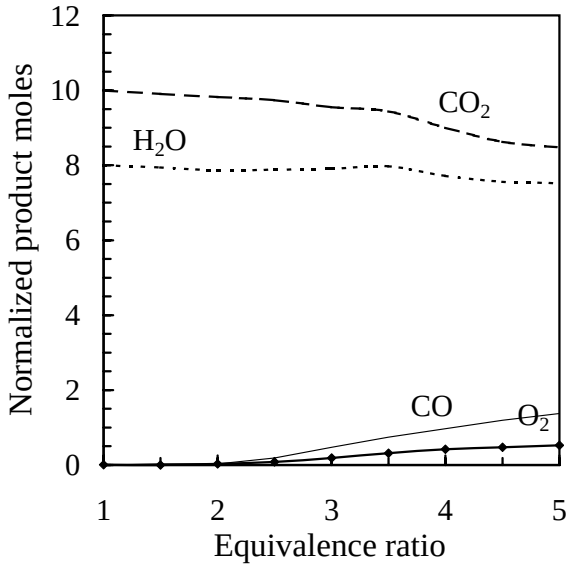

Figure 93: Normalized product moles of second burn with reactants calculated using equilibrium concentrations as a function of the first burn equivalence ratio. N_2 product moles are omitted for clarity.

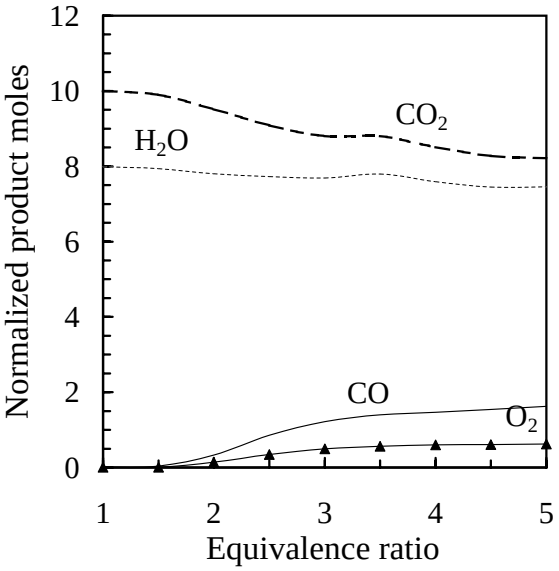

Figure 94: Normalized product moles of second burn with reactants calculated using frozen chemistry as a function of the first burn equivalence ratio. N_2 product moles are omitted for clarity.

compared to the reactants from the equilibrium case.

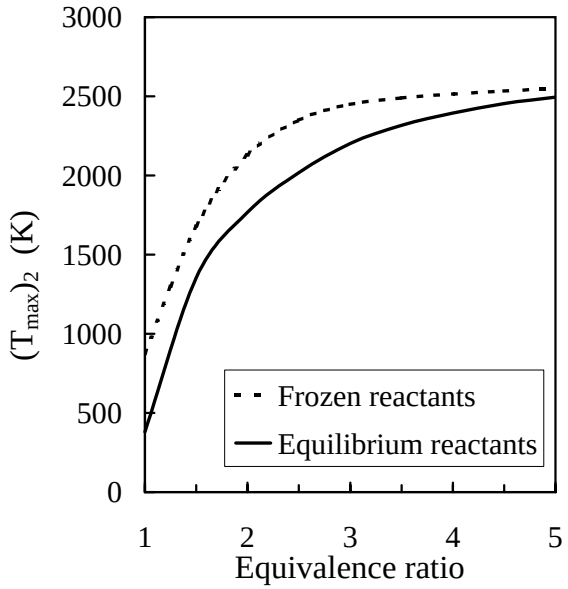

Figure 95: Predictions of the maximum temperature during the second burn as a function of equivalence ratio.

11.3 Flame speed results

Several schlieren images visualizing the flame front at equivalence ratios of 1, 3, and 5 appear in Appendix B. Successive images can be used to determine the outward velocity V_f of the flame as a function of the changing radius R_f over time.

$$V_f = \frac{dR_f}{dt} \tag{39}$$

This flame velocity is larger than the burning velocity S_u due to the displacement effect of the combustion creating a fluid velocity u_u ahead of the flame. The burning velocity S_u is defined to be the velocity of the flame relative to the flow ahead so that we have

$$V_f = S_u + u_u \ . \tag{40}$$

When the combustion products are stationary, the conservation of mass implies that

$$u_u = S_u(E-1) = S_u\left(\frac{v_f}{v_u} - 1\right) \tag{41}$$

and therefore,

$$S_u = \frac{V_f}{E} \tag{42}$$

where the volumetric expansion ratio E is defined as the ratio of the volume of burned gas to the volume of unburned gas. A constant-pressure equilibrium calculation is used

to compute the expansion ratio and determine the burning velocity from experimental measurements of flame speed.

The effect of curvature, referred to as flame stretch, on the laminar burning velocity must be considered. We define a stretch factor K_s for a spherical flame as

$$K_s = \frac{2}{R_f}\frac{dR_f}{dt} \approx \frac{2}{R_f}V_f \ . \tag{43}$$

The unstretched laminar burning velocity ${S_u}^\circ$ can be determined by extrapolating the burning velocity as the radius of the flame goes to infinity, or as the stretch goes to zero. The relationship between the stretch factor, burning velocity, and unstretched burning velocity is

$$S_u = {S_u}^\circ - L_M K_s \tag{44}$$

where L_M is the Markstein number. The parameters in the previous equation can be found by plotting S_u as a function of K_s. The slope of the burned velocity versus the stretch factor is the Markstein number and the y-intercept is the unstretched velocity.

The flame velocity as observed from the recorded images of Fig. 100 is plotted as a function of time in Fig. 96. The data points described by the horizontal burning

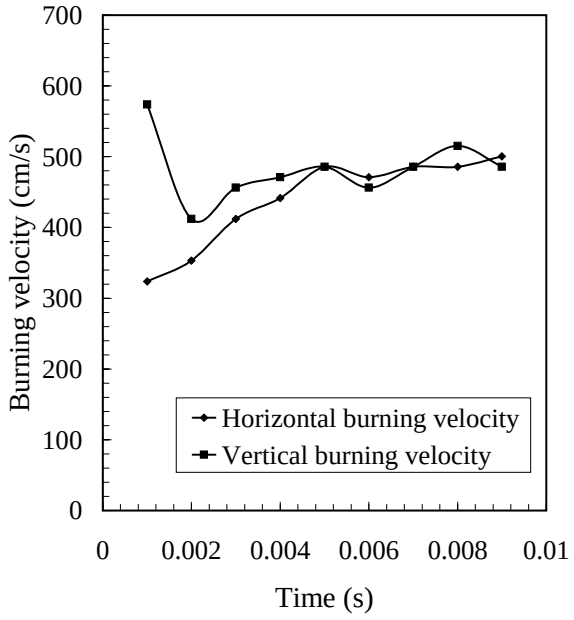

Figure 96: Burning velocity as a function of time for a stoichiometric mixture of JP-10 in air at initial conditions of 100 kPa and 380 K.

velocity correspond to the change in position of the flame front parallel to the ignition probes. The data points described by the vertical burning velocity correspond to the change in position of the flame front perpendicular to the ignition probes. From the STANJAN equilibrium code, the expansion ratio for a stoichiometric mixture of JP-10 in air at 100 kPa was determined to be 8.19. Figure 97 shows S_u versus the stretch factor.

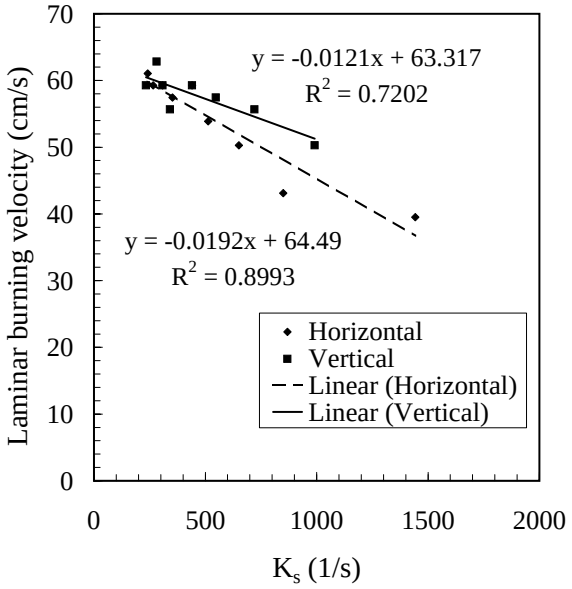

Figure 97: Laminar burning velocity as a function of the flame stretch for a stoichiometric mixture of JP-10 in air at initial conditions of 100 kPa and 380 K.

Straight lines have been fitted to the data and extrapolated to a stretch factor of zero. The y-axis intercept value of 64 cm/s is our estimate of the unstretched laminar burning velocity.

11.4 Conclusion

Pre-mixed partial oxidation experiments were conducted with JP-10 and air mixtures in a heated explosion vessel. JP-10 and air mixtures were found to combust for equivalence ratios less than 5. After the initial combustion event, additional air was added to obtain an equivalent stoichiometric mixture and a second combustion event was initiated. Combustion was achieved for these mixtures with an initial equivalence ratio of 2.5 or greater.

Comparisons of the maximum pressure difference, as a measure of the mixture's equivalent energy release, with the maximum pressure difference for stoichiometric JP-10 combustion in air at initial pressures of 100 kPa resulted in effectiveness factors ranging between 60 and 94%. Thus, combusting the products of JP-10 partial oxidation do not achieve the same pressure rise as combusting stoichiometric JP-10 in air directly. To operate at the highest effectiveness values, the highest possible equivalence ratios should be used. However, during the experimental testing, significant soot formation was observed. Based on the previous experience with coke deposit formation in the zeolite HC study, catalyst activity is greatly affected by coke deposits. We expect that operating a partial oxidation reactor under such rich conditions would have a limited time span of operation due to catalyst deactivation.

12 Conclusions

Thermal and catalytic cracking of JP-10 has been investigated in a flowing reactor.

Chromatography with liquid injection Gas chromatography with liquid injection studied the effect of sample dilution. A dilution of 0.05% wt of JP-10 in hexane in a 1 μl sample was required to obtain symmetric chromatograms. Symmetric chromatograms are necessary for accurate quantitative measurements of the sample amount and retention time.

Chromatography with gaseous injection Gas chromatography with gaseous injection quantified the retention time of the major alkanes from C_5 to C_{12}. These retention times established the region boundaries of signal integration so the product distributions from the HC reactions could be quantified.

JP-10 vapor pressure A correlation for the vapor pressure of JP-10 was generated from experimental data. It was determined that the reactor panel could not obtain the temperatures necessary to vaporize JP-10 to achieve a rise in the system pressure greater than approximately 130 kPa. As a result, most tests were completed at atmospheric pressure.

Data analysis procedure A procedure to analyze the conversion of JP-10 into smaller molecular weight compounds enabled conclusions to be made regarding the effect of operating conditions. The major system diagnostic was the instantaneous accumulator position. A relationship developed between the accumulator position and the number of moles of products in the system. This was related to the number of moles injected of liquid JP-10 to conduct a mole balance. The data obtained with this method are summarized below.

Samples taken from the accumulator with the gas chromatograph yielded the distribution of the product gas retention times. The individual signal peaks were split into regions corresponding to compounds with the same carbon number. This allowed a qualitative measurement of the product distribution and enabled comparisons between tests. Although saturation of the GC column occurred due to the large sample sizes, trends are still observed.

Thermal cracking Tests with the heated reactor panel were completed to determine the effect of thermal reactions on the hydrocarbon cracking of JP-10. Liquid JP-10 was metered into the system and allowed to flow through the reactor which was at 500°C. Conversion ratios of approximately 3% and less were observed. The GC chromatograms did show a slight increase in C_5 and C_6 compounds in addition to higher molecular weight compounds ($> C_{12}$).

Thermal reactions were not found to be significant for JP-10 at 500°C. Increasing the reactor temperature may cause these reactions to be of more importance.

Fuel Flowrate (g/hr)	mole ratio	% conversion
2.3	1.11	3.15
6.2	1.09	2.19
10.6	1.02	1.90

Table 21: Major results of thermal cracking tests.

Effect of zeolite type Throughout the course of testing using zeolite pellets installed in the reactor, two separate batches were prepared. Since the zeolite activity was not verified by standard tests before installation, the conversion ratios were compared. This was the only available means with which to verify similar zeolite activity. Additionally, after the zeolite had become coked through testing in the reactor panel, its activity was restored by a regeneration process. The activity as measured by the mole balance seemed to be more consistent than the GC percent conversion.

	2.3 g/hr		10.6 g/hr	
	mole ratio	% conv.	mole ratio	% conv.
1st batch	1.826	34	1.472	31
1st batch regenerated			1.583	61
2nd batch	1.444	36		

Table 22: Effect of zeolite activity on conversion.

The number of times the same zeolite pellets may be regenerated and still maintain high activity should be investigated. The regeneration process is an acceptable means to restore zeolite activity but over time the molecular structure degrades, ultimately destroying the zeolite. Because of the significant coking observed in our tests, a higher regeneration temperature than values used in the heavy oil cracking industry was required. Holding the zeolite within this high temperature environment acts to accelerate the structural degradation of the zeolite.

Effect of fuel flowrate The effect of the liquid fuel flowrate on the catalytic cracking tests was measured by comparing the conversion ratios at three different metering speeds. As in the thermal tests, a decrease in the fuel flowrate results in converting more JP-10 into smaller compounds.

Fuel Flowrate (g/hr)	mole ratio	% conversion
2.3	1.70	34
10.6	1.51	41

Table 23: Effect of fuel flowrate on catalytic cracking tests with HY zeolite at a reactor temperature of 500°C.

This is expected because of the increased residence time of the molecules in the heated reactor plumbing at the lower flowrates. The chemical reactions had more time to initiate and for surface reactions to occur. Due to the size of the system and the pump capabilities, testing at lower flowrates was not easily achieved without significant repeatibility issues. Testing at even lower flowrates may observe higher conversion ratios, but coking is known to increase as the Reynolds number decreases. Experimental testing is required to determine the dominant effect.

Effect of zeolite type Three common zeolites (HY, USY, and Beta) were tested to determine their effect on the conversion ratio. HY is known as a large-pore zeolite commonly used in heavy oil cracking, while USY is a modified version of the Y zeolite designed to be more resistant to coke deposits. Beta has a larger range of pore dimensions suggesting it might be able to produce a greater variety of cracked products. The mole balance results were similar for HY and Beta, while USY was significantly lower. The USY zeolite was not observed to have a significant reduction in coking as compared to the others. It seems that none of these tested zeolites are optimal for hydrocarbon cracking with JP-10 due to the rapid deactivation by coke deposits and relatively low conversion ratios.

Zeolite	mole ratio	% conversion
HY	1.70	34
USY	1.14	11
Beta	1.67	70

Table 24: Effect of zeolite type on catalytic cracking tests at a reactor temperature of 500°C and fuel flowrate of 2.3 g/hr.

Effect of system pressure Although the average system temperature was not high enough to achieve the desired system pressure of 200 psi by the vaporization of JP-10 alone, a test was completed with the system pressurized with nitrogen gas. In this test, a backpressure was applied to the accumulator in addition to pressurizing the system to approximately 400 kPa. The movement of the accumulator position was significantly reduced for the case at 400 kPa as compared with the 100 kPa case as denoted by the reduced mole ratio. However, the GC analysis observed a greater percent conversion.

Pressure (kPa)	mole ratio	% conversion
100	1.70	34
400	0.996	53

Table 25: Effect of system pressure on catalytic cracking tests with HY zeolite at a reactor temperature of 500°C and a fuel flowrate of 10.6 g/hr.

Effect of reactor temperature Chemical reactions are known to depend strongly on temperature. A series of catalytic cracking tests was completed with HY zeolite as a function of reactor temperature. The conversion percent and mole balance both increase as the temperature in the reactor increases.

Temperature (°)	mole ratio	% conversion
500	1.70	34
425	1.29	39
350	1.41	28
300	1.15	6
250	0.99	1

Table 26: Effect of reactor temperature on catalytic cracking tests with HY zeolite at a fuel flowrate of 10.6 g/hr.

Catalytic versus thermal cracking The effect of catalytic cracking over thermal cracking on the conversion of JP-10 was investigated. As expected, the addition of the zeolite catalyst increases the cracking reactions and generates products of smaller molecular weight than the parent JP-10 molecule. The estimated uncertainty in the mole ratio is ±6.4% and the uncertainty in the average % wt. conversion is ±12.5%.

	2.3 g/hr		10.6 g/hr	
	mole ratio	% conv.	mole ratio	% conv.
Thermal	1.11	3.15	1.02	1.90
Catalytic	1.70	34	1.51	41

Table 27: Effect of catalytic and thermal cracking on conversion.

Comparison between the mole ratio and mass conversion fraction For thermal cracking, there was too much variability in the results and an average molar mass of the products could not be determined. For catalytic cracking, the measured mole ratio was found to be an approximately linear function of mass conversion fraction, see Fig. 98. This indicated that the average molar mass of the products is approximately constant. Using the mass balance and mole balance analysis for the overall reaction, the average molar mass of the products is estimated to be 65 ± 11 g/mol. Assuming that all the atoms are in a single notional molecule, the average number of carbon atoms is 4.8 ± 0.8 for an H/C ratio of 1.6.

Pre-mixed partial oxidation experiments Experiments were carried out in an explosion vessel to examine the feasibility of creating partial oxidation products with rich

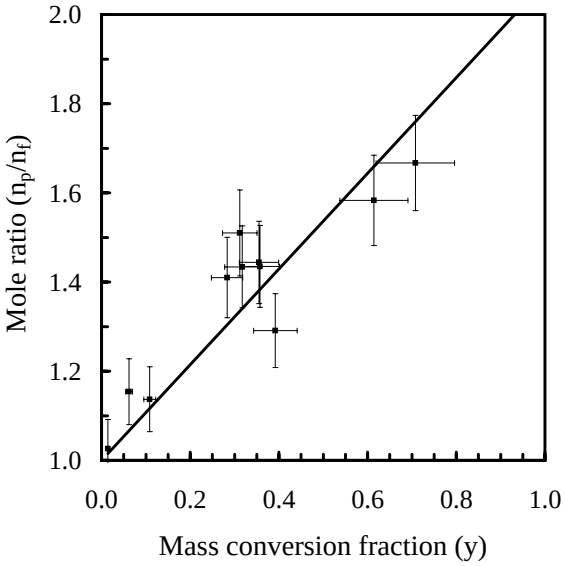

Figure 98: Mole ratio as a function of the mass conversion fraction for the catalytic cracking tests.

premixed combustion. Mixtures of JP-10 and air could be combusted up to an equivalence ratio of 5. The rich flammability limit appears to be at about 5; mixtures richer than this did not burn. The combustion products of rich mixtures with $\phi > 2$ appear to be consistent with the products predicted by a frozen cooling of the adiabatic, equilibrium, constant volume explosion products.

For equivalence ratios between 2.5 and 4.5, it was possible to add a stoichiometric amount of air after the first burn and carry out a second burn. The peak pressure obtained in the second burn was consistent with equilibrium predictions assuming frozen product composition of the first burn. The peak pressure rise of the second burn was an increasing function of the equivalence ratio in the first burn and reaches a maximum value of about 95% of the stoichiometric peak pressure rise at an initial equivalence ratio of 4 to 4.5. We conclude that from an energetics point of view , partial oxidation should be carried out an equivalence ratio that is as high as possible while avoiding coking due to soot production. Soot production was evident in the present experiments as the equivalence ratio approached 5. Other properties such as flame speed, expansion ratio, and detonation cell size need to be examined to further constrain the choice of equivalence ratio. The laminar burning speed of stoichiometric JP-10 and air mixtures at 100 kPa and 105°C is about 64 cm/s, similar to the peak laminar burning speed of other hydrocarbon fuels in air.

Acknowledgement

This work was carried out under P.O. No. 00-592 for Advanced Projects Research, Inc. under AF contract F04611-99-C-0017. Contract administration, mechanical design and fabrication of two components of the facility: the reactor heater and accumulator, were carried out by Advanced Projects Research, Inc. Key participants from APRI included Toby Rossmann, Jay Marsh, Kevin Moore, and Tom Sobota.

We acknowledge Kathia Devouge for her preliminary design work. Special thanks to Nathan Dalleska, Director of the Environmental Analysis Center at Caltech, for his immensely valuable lessons on the theory and operation of the gas chromatograph. Prof. Mark Davis of Chemical Engineering at Caltech and members of his research group were very helpful with sharing their expertise in zeolite chemistry. In particular, we thank Andrea Wight, Ph.D. student in Chemical Engineering at Caltech, for providing not only many zeolite samples and use of her chemical laboratory but also many helpful discussions on zeolite structure, preparation, and handling procedures. We thank Daniel Lieberman for his contributions to the pre-mixed partial oxidation experiments.

References

[1] Austin, J. M. and Shepherd, J. E., "Detonation in Hydrocarbon Fuel Blends," Accepted for publication in Combustion and Flame.

[2] Hitch, B., "The Effect of Autoignition-Promoting Additives on Deflagration-to-Detonation Transition," 38th AIAA/ASME/SAE/ASEE Joint Propulsion Conference and Exhibit, July 7–10, 2002, Indianapolis, IN, AIAA 2002–3719.

[3] Akbar, R., Thibault, P. A., Harris, P. G., Lussier, L. S., Zhang, F., Murray, S. B., and Gerrard, K., "Detonation Properties of Unsensitized and Sensitized JP-10 and Jet-A Fuels in Air for Pulse Detonation Engines," 36th AIAA/ASME/SAE/ASEE Joint Propulsion Conference and Exhibit, July 16–19, 2000, Huntsville, AL, AIAA 2000–3592.

[4] Zhang, F., Murray, S. B., and Gerrard, K. B., "JP-10 Vapour Detonation at Elevated Pressures and Temperatures," 18th ICDERS, Seattle, WA, July 29 – August 3, 2001.

[5] Olah, G. A. and Molnar, A., *Hydrocarbon Chemistry*, John Wiley and Sons, Inc., New York, NY, 1995.

[6] Green, R. J., Nakra, S., and Anderson, S. L., "Breakdown Behavior of Fuels for Pulse Detonation Engines," Office of Naval Research, Energy Conversion and Propulsion Program.

[7] Li, S. C., Varatharajan, B., and Williams, F. A., "The Chemistry of JP-10 Ignition," 39th AIAA Aerospace Sciences Meeting and Exhibit, January 8–11, 2001, Reno, NV, AIAA 2001–1074.

[8] Davidson, D. F., Horning, D. C., Oehlschlaeger, M. A., and Hanson, R. K., "The Decomposition Products of JP-10," 37th AIAA/ASME/SAE/ASEE Joint Propulsion Conference and Exhibit, July 8–11, 2001, Salt Lake City, UT, AIAA 2001–3707.

[9] Schauer, F., Stutrud, J., and Bradley, R., "Detonation Initiation Studies and Performance Results for Pulsed Detonation Engines," 39th AIAA Aerospace Sciences Meeting and Exhibit, January 8–11, 2001, Reno, NV, AIAA 2001-1129.

[10] Abbot, J. and Wojciechowski, B. W., "Catalytic Reactions of n-hexane on HY Zeolite," *The Canadian Journal of Chemical Engineering*, Vol. 66, October 1988, pp. 825–829.

[11] Dyer, A., *An Introduction to Zeolite Molecular Sieves*, John Wiley and Sons, Inc., New York, NY, 1988.

[12] Meier, W. M. and Olson, D. H., *Atlas of Zeolite Structure Types*, Butterworth-Heinemann, London, 3rd ed., 1992.

[13] van Santen, R. A. and Niemantsverdriet, J. W., *Chemical Kinetics and Catalysis*, Plenum Press, NY, 1995.

[14] Chang, C. D., *Hydrocarbons from Methanol*, Marcel Dekker, Inc., NY, 1983.

[15] Honna, K., Sato, K., Araki, Y., Miki, Y., Matsubayashi, N., and Shimada, H., "HY zeolite-based catalyst for hydrocracking heavy oils," *Hydrotreatment and Hydrocracking of Oil Fractions*, edited by B. Delmon, G. F. Froment, and P. Grange, Elsevier Science, B.V., Amsterdam, 1999, pp. 427–430.

[16] Dwyer, J., Dewing, J., Karim, K., Ojo, A. F., Garforth, A. A., and Rawlence, D. J., "Hydrocarbon Transformations over Analogues and Derivatives of Zeolite Y," *Zeolite Chemistry and Catalysis*, edited by P. A. Jacobs, Elsevier Science Publishers, B.V., Amsterdam, 1991, pp. 1–23.

[17] Lopes, J. M., Lemos, F., Ribeiro, F. R., and Derouane, E. G., "A comparison of the catalytic properties of SAPO-37 and HY zeolite in the cracking of n-heptane and 2,2,4-trimethylpentane," *Zeolite Chemistry and Catalysis*, edited by P. A. Jacobs, Elsevier Science Publishers, B.V., Amsterdam, 1991, pp. 365–371.

[18] Paal, Z. and Xu, X. L., "Reactions of n-Hexane over Pt-HZSM-5 Catalyst," *Studies in Surface Science and Catalysis*, edited by H. K. Beyer, H. G. Karge, I. Kiricsi, and J. B. Nagy, No. 94 in Catalysis by Microporous Materials, Elsevier Science, B. V., Amsterdam, 1995, pp. 590–597.

[19] Sobel, D. R. and Spadaccini, L. J., "Hydrocarbon Fuel Cooling Technologies for Advanced Propulsion," *Journal of Engineering for Gas Turbines and Power*, Vol. 119, April 1997, pp. 344–351.

[20] H. Huang, D. R. S. and Spadaccini, L. J., "Endothermic Heat-Sink of Hydrocarbon Fuels for Scramjet Cooling," 38th AIAA/ASME/SAE/ASEE Joint Propulsion Conference and Exhibit, July 7–10, 2001, Indianapolis, IN, AIAA 2002–3871.

[21] Spadaccini, L. J., Sobel, D. R., and Huang, H., "Deposit Formation and Mitigation in Aircraft Fuels," *Journal of Engineering for Gas Turbines and Power*, Vol. 123, October 2001, pp. 741–746.

[22] Edwards, T., "Storable Fuels and Connected Issues of Hypersonic Flight," *Future Aerospace Technology in the Service of the Alliance: Sustained Hypersonic Flight*, NATO RTO, December 1997, AGARD-CP-600-03-Vol 3.

[23] Lander, H. and Nixon, A. C., "Endothermic Fuels for Hypersonic Vehicles," *Journal of Aircraft*, Vol. 8, No. 4, 1971, pp. 200–207.

[24] Chin, J. S. and Lefebvre, A. H., "Influence on Flow Conditions on Deposits From Heated Hydrocarbon Fuels," *Journal of Engineering for Gas Turbines and Power*, Vol. 115, July 1993, pp. 433–438.

[25] Condon, R. D., *Instrumentation in Gas Chromatography*, Eindhoven, Centrex, 1968.

[26] Grant, D. W., *Capillary Gas Chromatography*, John Wiley and Sons Ltd, New York, NY, 1996.

[27] Pecsok, R. L. and Shields, L. D., *Modern Methods of Chemical Analysis*, John Wiley and Sons Ltd, New York, NY, 1968.

[28] David, D. J., *Gas Chromatographic Detectors*, John Wiley and Sons Ltd, New York, NY, 1974.

[29] Braithwaite, A. and Smith, F. J., editors, *Chromatographic Methods*, Blackie Academic and Professional, Bishopbriggs, Glasgow, 5th ed., 1996.

[30] Woodrow, J. E., "The Laboratory Characterization of ARCO Jet Fuel Vapor and Liquid," Report prepared for the National Transportation Safety Board, June 2000.

[31] Shepherd, J. E., Austin, J., Chao, T., Pintgen, F., Wintenberger, E., Jackson, S., and Cooper, M., "Detonation Initiation, Propagation, and Structural Response," *Fourteenth ONR Propulsion Meeting*, edited by G. D. Roy and F. Mashayek, Department of Mechanical & Industrial Engineering, University of Illinois at Chicago, Chicago, August 2001, pp. 148–153, Office of Naval Research, Energy Conversion and Propulsion Program.

[32] Anonymous, "Handbook of Aviation Fuel Properties," CRC Report 530, Society of Automotive Engineers, Warrendale, PA, 1983.

[33] Anonymous, "High Temperature JP-10 Vapor Pressure Data," Data from USAF Wright-Patterson AFB and Adroit Systems, Inc.

[34] Shepherd, J. E., Krok, J. C., and Lee, J. J., "Jet A Explosion Experiments: Laboratory Testing," Explosion Dynamics Laboratory Report FM97-5, November 21, 1997.

[35] Townsend, A. T. and Abbot, J., *Catalytic cracking of tetralin on HY zeolite*, Vol. 90 of *Applied Catalysis A: General*, Elseview Science Publishers, B.V., Amsterdam, 1991, pp. 97–115.

[36] Pickard, J. A., "Kinetics of the Autoxidation of a Jet-A Fuel," *Energy and Fuels*, Vol. 10, 1996, pp. 1074–1077.

[37] Bevington, P. R., *Data Reduction and Error Analysis in the Physical Sciences*, McGraw-Hill, 1969.

[38] O'Connor, R. P. and Schmidt, L. D., "Catalytic Partial Oxidation of Cyclohexane in a Single-Gauze Reactor," *Journal of Catalysis*, Vol. 191, 2000, pp. 245–256.

[39] Schmidt, L. D., Huff, M., and Bharadwaj, S. S., "Catalytic Partial Oxidation Reactions and Reactors," *Chemical Engineering Science*, Vol. 49, No. 25A, 1994, pp. 3981–3994.

[40] Veser, G. and Schmidt, L. D., "Ignition and Extinction in the Catalytic Oxidation of Hydrocarbons over Platinum," *AIChE Journal*, Vol. 42, No. 4, 1996, pp. 1077–1087.

[41] Reynolds, W. C., "The Element Potential Method for Chemical Equilibrium Analysis: Implementation in the Interactive Program STANJAN, Version 3," Tech. rep., Dept. of Mechanical Engineering, Stanford University, Stanford, CA, January 1986.

A Timeline

Following is a timeline of major accomplishments in constructing and running the experiments of the reactor panel. After May 2002, many similar experimental tests were run. The type of test and important test parameters are listed. If not specified, the operating parameters consisted of a reactor temperature equal to 500°C and a system pressure of 101 kPa. It should be noted that the system required approximately 6 hrs and 12 hrs to reach operational temperatures for the thermal and catalytic tests respectively. The time of fuel injection was approximately 2 hrs, 1 hr and 30 min for the fuel pump metering settings (FP) of 125, 70 and 25 respectively. An additional time of 45 min per sample taken by the GC out of the accumulator was required.

Date	Description
Sept. 20, 2000	Received ordered components for reactor panel.
Oct. 4, 2000	Completed schematic of reactor panel with dimensions. Designed panel support system. Purchased plywood and sheet metal for panel.
Oct. 17 and 20, 2000	Obtained information from Chemical Engineering department regarding packed beds of zeolite pellets.
Dec. 12, 2000	Obtained porous disks for zeolite bed.
Dec. 14, 2000	Machine shop finished construction of accumulator indicator.
Dec., 2000	Reactor panel constructed.
Jan. 4, 2001	Designed and completed Autocad schematic of zeolite bed containment device.
Jan.-Feb. 2001	Assembly of components onto reactor panel and panel supports.
Mar. 12, 2001	Received accumulator. Replaced internal wiring with high temperature heater hook-up wire.
May-Jun., 2001	Completed wiring design of controllers, fuses, power supply, thermocouples and pressure transducers. Electricians installed dedicated wall plug for the reactor panel.
Jun. 15, 2001	Ordered rope heaters for system plumbing.
Jul.-Aug., 2001	Installation of Swagelok connections and plumbing on reactor panel. Initial leak testing.
Aug. 16, 2001	Ordered controllers for heating zones.
Aug. 22, 2001	Tested rotometer operation.
Aug. 26, 2001	Replace GC tubing with copper refrigeration tubing. Ordered analytical grade regulators for GC. Met director of Environmental Analysis Center for tutorial on GC operation.

continued	
Sept. 4-9, 2001	Completed 8 separate leak tests with and without accumulator. Replaced leaking Swagelok components and identified leak across piston in accumulator.
Sept. 10, 2001	Built phenolic supports of reactor plumbing and stand for fuel pump on back of panel.
Sept. 13. 2001	Verified operation of reactor heaters. Took apart accumulator to be honed.
Sept. 16, 2001	Installed vacuum pump at system outlet. Calibrated fuel pump. Began learning GC ChemStation software.
Sept. 17, 2001	Calibrated pressure gauges to calibration panel pressure transducers.
Sept. 20, 2001	Installed thermocouples on system tubing. Conducted temperature distribution test. Reassembled accumulator after honing procedure.
Sept. 28, 2001	Leak test with accumulator. Tested system with fuel pump and discovered backpressure is required for operation.
Oct. 4, 2001	Vent hood design completed.
Oct. 10, 2001	Combined vapor pressure curves to determine correlation between 1.5 and 4.0 T^{-1} (1000/K).
Oct.-Nov., 2001	Injected JP-10 in heated system with fuel pump. Observed lower pressure rise than predicted by vapor pressure curve.
Nov. 8, 2001	Additional supports added to bottle rack. Venting regulator installed on accumulator.
Dec. 19, 2001	Began GC analysis of normal alkanes to determine retention times. Studied effect of GC operating parameters on detector output.
Jan. 9, 2002	Replaced inoperational network card. Added a second network card into computer.
Jan.-Mar., 2002	Learned techniques of liquid injection from Environmental Analysis Center. Conducted a total of 39 tests with liquid injection. Conducted a total of 51 tests with gaseous injection. Made dilution samples of alkanes.
Feb. 2, 2002	Conducted experiments to determine flowrate through sample loop versus accumulator pressure.
Mar. 12, 2002	Calculated volumes of system plumbing.
Apr. 9, 2002	Remove heater and adhesive from accumulator. Replace with new flexible heater.

continued	
Apr. 16, 2002	Remove upstream fuel pump and valves. Seal bottom of evaporator and install septum for manual injection of liquid JP-10. Conducted vaporization tests. Completed evaporator redesign and sent drawings to machine shop.
May 1, 2002	Learn about zeolites (their formation and procedures for ion exchange, calcination and handling) from Chemical Engineering department. Installed new evaporator vessel and performed leak test.
May 9, 2002	Learned how to pelletize zeolite powder and began ion exchange of HY, USY and Beta.
May 15, 2002	Test procedures determined. Two thermal tests completed at FP = 70.
May 16, 2002	Thermal test at FP = 125. Learn RAMP/SOAK function of temperature controllers.
May 20, 2002	Thermal test at FP = 125. Two thermal tests at FP = 70.
May 23 and 24, 2002	Catalytic test with HY at FP = 125 (3 samples). Catalytic test with HY at FP = 70 (1 sample).
May 29, 2002	Thermal test at FP = 70 (1 sample). Thermal test at FP = 125 (2 samples).
Aug. 5, 2002	Two thermal tests at FP = 125 (1 sample each test).
Aug. 6, 2002	Thermal test at FP = 70 (1 sample). Two thermal tests at FP = 25 (1 sample each test).
Aug. 7, 2002	Thermal test at FP = 125. Two thermal tests at FP = 70. Thermal test at FP = 25 (1 sample).
Aug. 8, 2002	Catalytic test with HY at FP = 125 (3 samples).
Aug. 15, 2002	Catalytic test with HY at FP = 25 (4 samples).
Aug. 18, 2002	Thermal test with FP = 125 (3 samples). Thermal test with FP = 70 (3 samples).
Aug. 19, 2002	Thermal test with FP = 25 (4 samples).
Aug 27, 2002	Regeneration of 1st batch of HY. Catalytic test with regenerated HY at FP = 125 (3 samples).
Sept. 6, 2002	Catalytic testing with regenerated HY at FP = 125 and reactor temperature of 350°C (3 samples).
Sept. 9, 2002	Catalytic cracking with regenerated HY at FP = 125 and reactor temperature of 250°C (3 samples).

continued	
Sept. 13, 2002	Catalytic cracking with regenerated HY at FP = 25 and system pressure of 400 kPa (3 samples).
Sept. 16, 2002	Catalytic cracking with 2nd batch of HY at FP = 25 (3 samples).
Sept. 18, 2002	Catalytic cracking with HY at FP = 25 (4 samples).
Sept. 20, 2002	Catalytic cracking with Beta at FP = 25 (4 samples).
Sept. 22, 2002	Catalytic cracking with USY at FP = 25 (3 samples).
Sept. 24, 2002	Catalytic cracking with 2nd batch of HY at FP = 125 and reactor temperature of 425°C (3 samples).
Sept. 26, 2002	Catalytic cracking with 2nd batch HY at FP = 125 and reactor temperature of 300°C (3 samples).
Oct. 1, 2002	Two thermal tests at FP = 25 (3 samples for each test).
Oct. 4, 2002	Thermal test at FP = 25 (3 samples for each test). Thermal test at FP = 125 (3 samples for each test).

B Schlieren images of flames in partial oxidation study

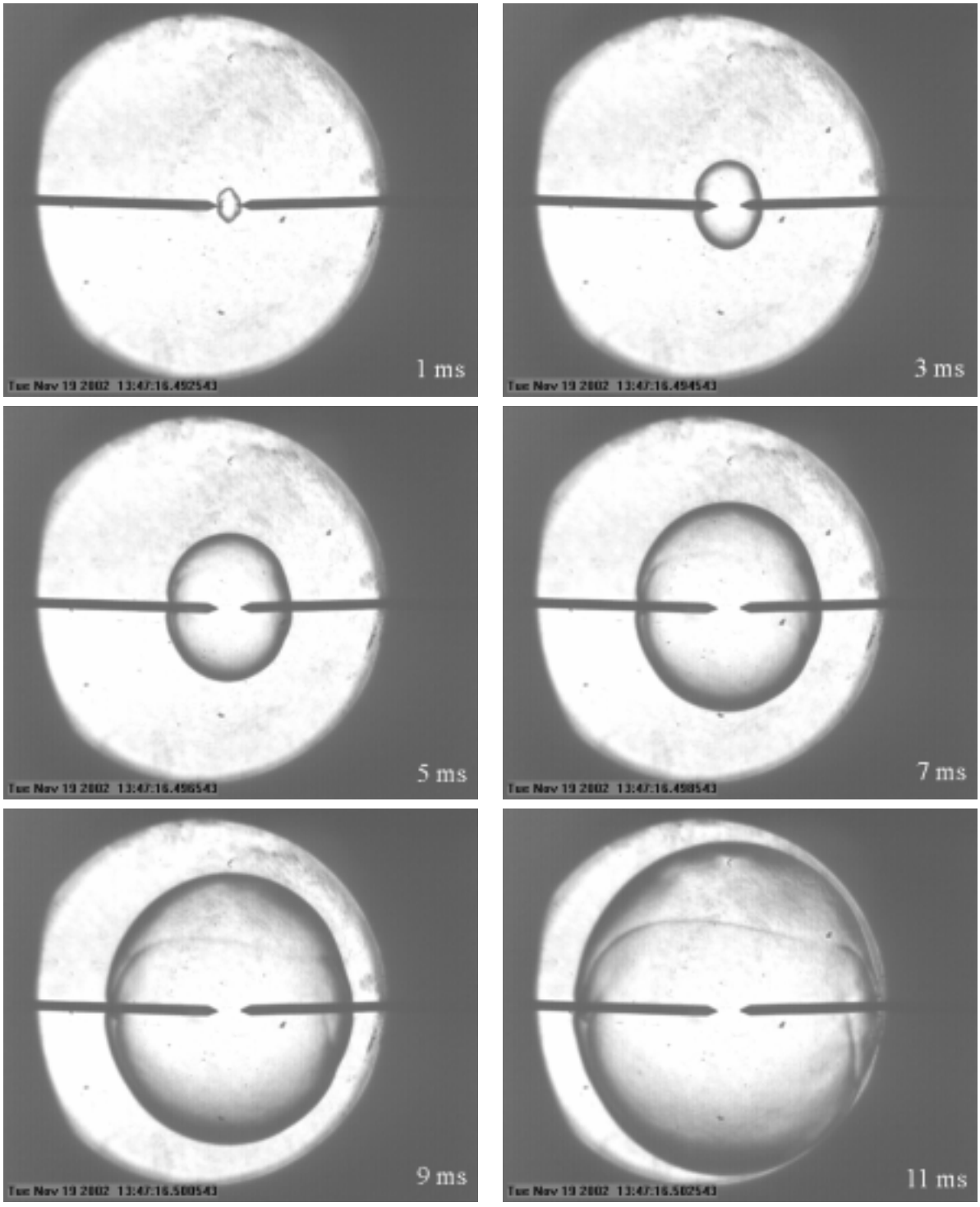

Figure 99: Successive images of first burn with an initial mixture of $C_{10}H_{16} + 14(O_2 + 3.76N_2)$ at $P_1 = 96$ kPa and initial temperature of 380 K.

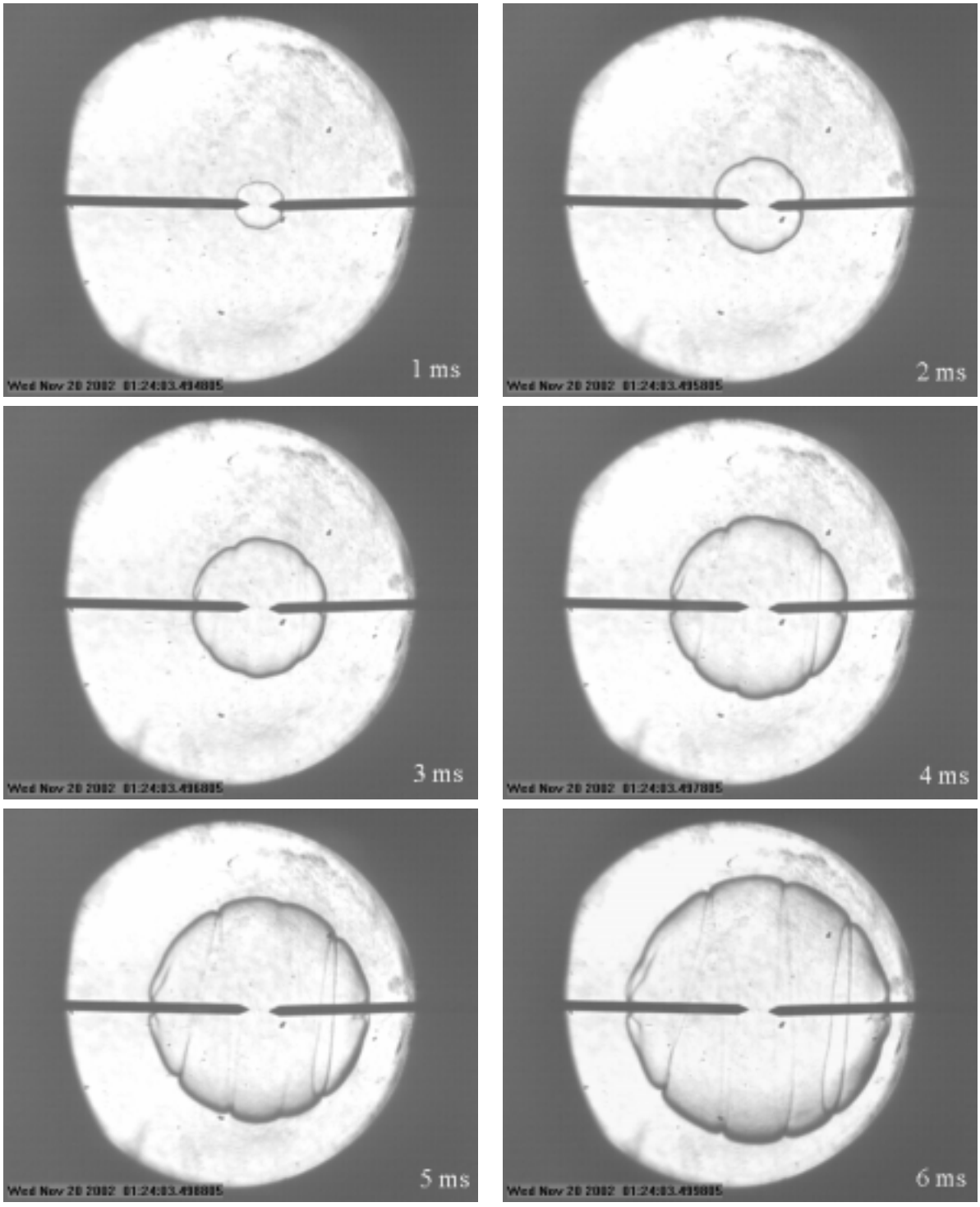

Figure 100: Successive images of first burn with an initial mixture of $3C_{10}H_{16} + 14(O_2 + 3.76N_2)$ at $P_1 = 33$ kPa and initial temperature of 380 K.

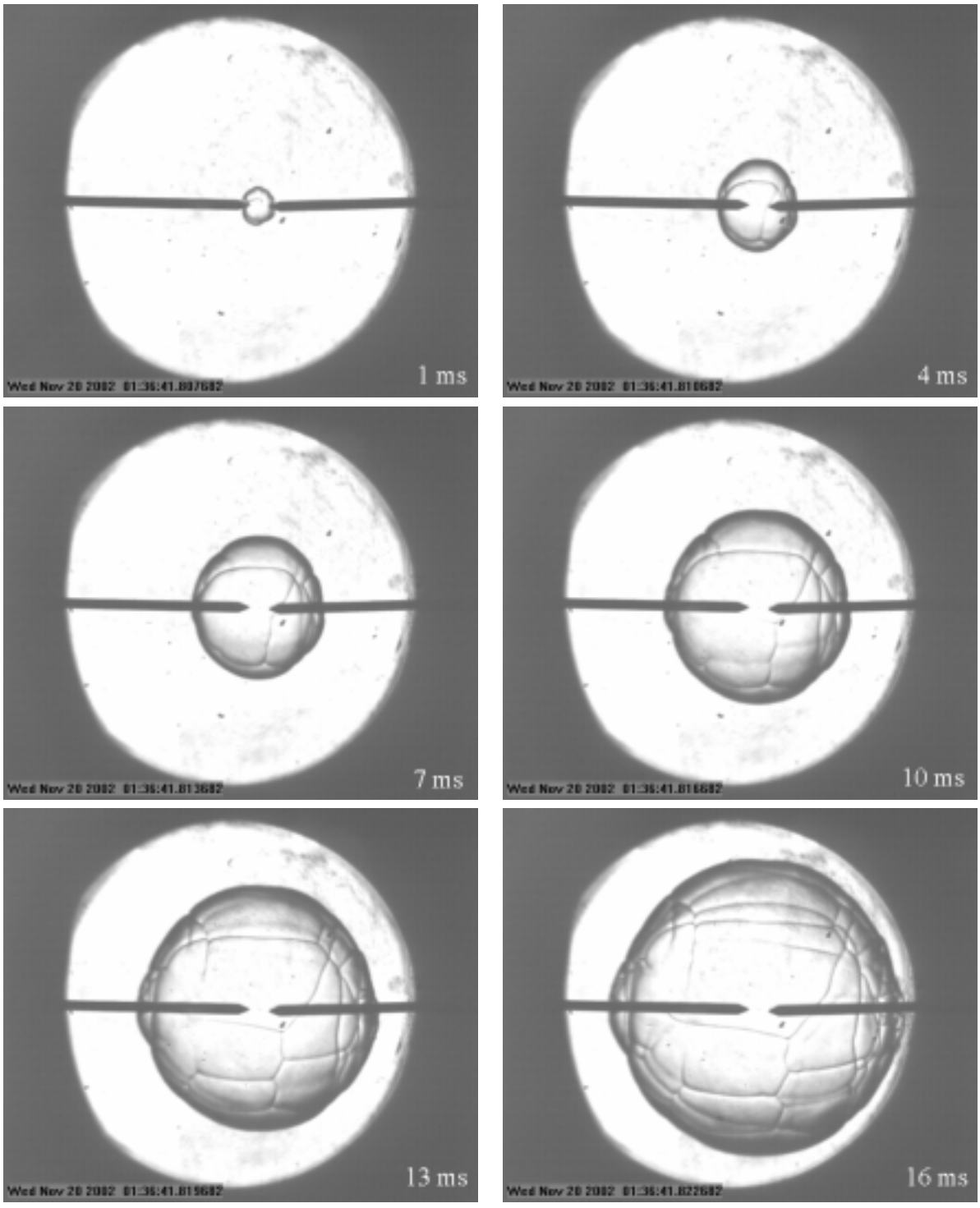

Figure 101: Successive images of second burn with an initial first-burn mixture of $3C_{10}H_{16}$ + $14(O_2 + 3.76N_2)$ at P_2 = 106.4 kPa and initial temperature of 380 K.

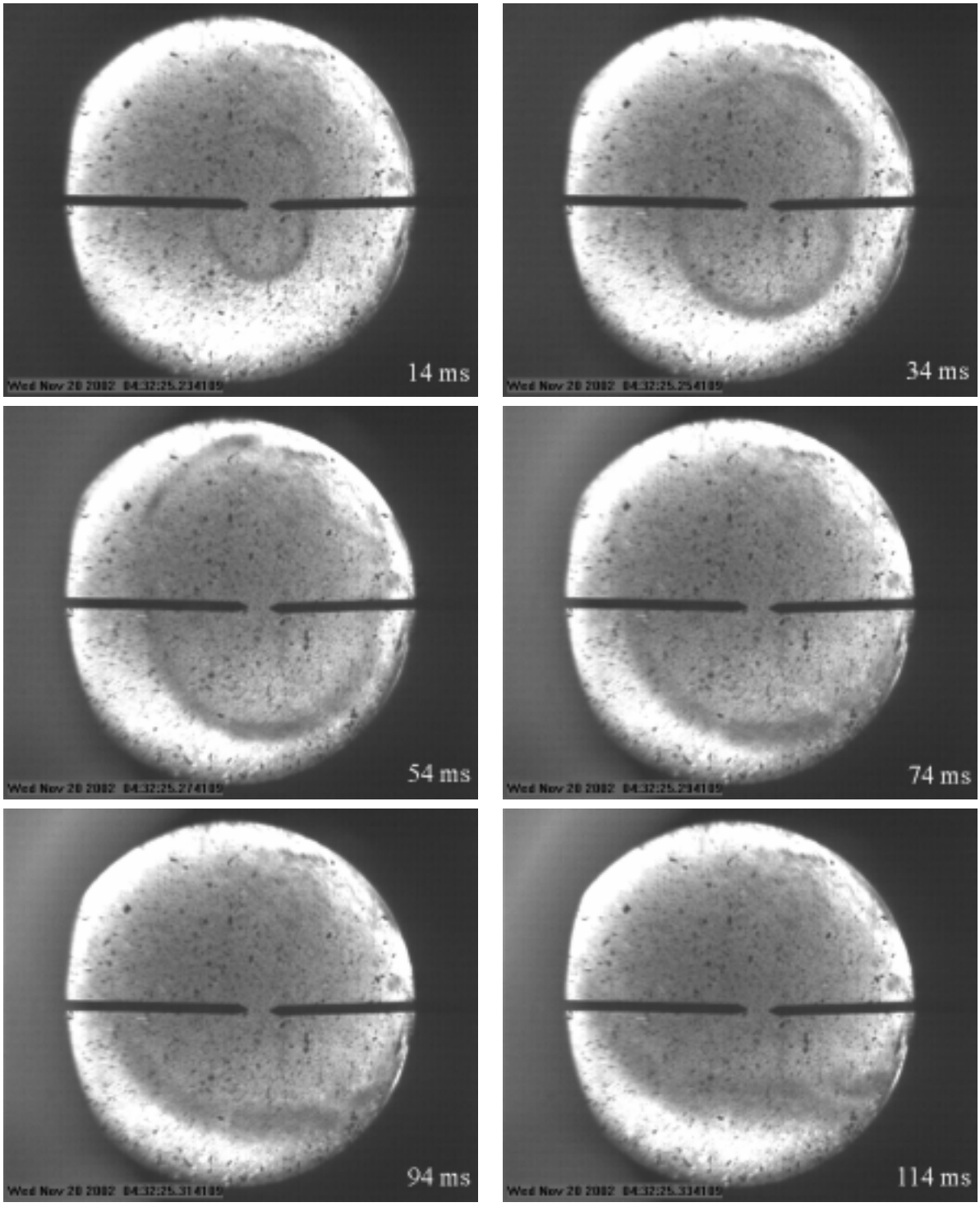

Figure 102: Successive images of first burn with an initial mixture of $5C_{10}H_{16} + 14(O_2 + 3.76N_2)$ at $P_1 = 20$ kPa and initial temperature of 380 K.